



UNIVERSIDAD NACIONAL DEL SUR

TESIS DOCTORAL EN INGENIERIA

**Medical 3D image processing applied to
computed tomography and magnetic
resonance imaging**

Diplom Informatiker

Felix Sebastian Leo Thomsen

BAHIA BLANCA

ARGENTINA

2017

Prefacio

Esta Tesis se presenta como parte de los requisitos para optar al grado Académico de Doctor en Ingeniería, de la Universidad Nacional del Sur y no ha sido presentada previamente para la obtención de otro título en esta Universidad u otra. La misma contiene los resultados obtenidos en investigaciones llevadas a cabo en el ámbito del Departamento de Ingeniería Eléctrica y Computadoras durante el período comprendido entre el 1.4.2012 y el 18.12.2016, bajo la dirección de Dr. Claudio Augusto Delrieux.



UNIVERSIDAD NACIONAL DEL SUR
Secretaría General de Posgrado y Educación Continua

La presente tesis ha sido aprobada el/..../..... , mereciendo la calificación de(.....)

Für Valeria

Contents

Abstract	IX
Nomenclature	X
1 Introduction	1
1.1 Osteoporosis	1
1.1.1 Imaging modalities	3
1.1.2 Measuring fracture risk	7
1.2 Alzheimer’s disease	11
1.3 Aim of the work	11
1.4 Hypothesis	12
1.5 Presentation of research	13
2 Standard QCT processing	16
2.1 Visualization of 3D volumes	16
2.2 Density-calibration of CT volumes	19
2.2.1 Automatic placing of the calibration phantom	22
2.3 Segmentation of the volume of interest	24
2.3.1 Segmentation by registration	26
2.4 Microstructural parameters	28
2.4.1 Global parameters	29
2.4.2 The bone map	31
2.4.3 Voxel counting	33
2.4.4 Marching Cubes	34
2.4.5 Direct secant method and run-length method	35
2.4.6 Distance transform method	37
2.4.7 Further standard methods and issues	40

2.5	Reconstruction techniques	40
3	Robust parameters	43
3.1	CT volumes and statistical methods	45
3.1.1	The vertebra phantom	45
3.1.2	Assessment of precision and accuracy	48
3.1.3	The Bioasset study	49
3.1.4	Prediction of failure load	50
3.1.5	In silico data	51
3.2	Neighborhood operators	52
3.2.1	Structural elements	53
3.2.2	Local operators	57
3.3	Preprocessing	59
3.3.1	The ridge map	59
3.3.2	The Monogenic signal	60
3.3.3	Micro-structural calibration	67
3.4	3D rose diagram	73
3.4.1	Introduction	74
3.4.2	Directional standard deviation	76
3.4.3	Preliminary results and discussion	79
3.5	Local fractal dimension	81
3.5.1	Introduction	82
3.5.2	Materials and Methods	83
3.5.3	Results	89
3.5.4	Discussion	93
3.5.5	Conclusion	95
3.6	Texture descriptors	96
3.6.1	Introduction	97
3.6.2	Materials and methods	98
3.6.3	Results	104
3.6.4	Discussion	107
3.6.5	Conclusion	109
4	Structural Insight	111
4.1	Purpose and workflow	112

4.2	General classes and features	114
4.2.1	Start screen	116
4.2.2	File formats	117
4.2.3	Visualization	117
4.2.4	General volume processing functions	118
4.2.5	Threads	118
4.2.6	Further methods to increase the efficiency	121
4.3	Core functions	122
4.3.1	Calibration	123
4.3.2	Segmentation	124
4.3.3	Computation of micro-structural parameters	125
4.4	Implementation of the structural parameters	128
4.4.1	Voxel counting	128
4.4.2	Marching cubes	128
4.4.3	Thickness transform method	129
4.4.4	Direct secant method and run-length method	130
	Conclusions	133
	List of Figures	136
	List of Tables	138
	References	139

Abstract

Existing microstructure parameters of computed tomography (CT) are able to compute architectural properties of the bone from ex-situ and ex-vivo scans while they are highly affected by the issues of noise and low resolution when applied to clinical in-vivo imaging. A set of improvements of the standard workflow for the quantitative computation of micro-structure from clinical in-vivo scans is proposed in this thesis. Robust methods are proposed (1) for the calibration of density values, (2) the binarization into bone and marrow phase, (3) fuzzy skeletonization and (4) the calibration of the CT volumes in particular for the computation of micro-structural parameters. Furthermore, novel algorithms for the computation of rod-volume fraction with 3D rose diagrams and fractal approaches are proposed and the application of local texture operators to diffusion tensor imaging is proposed. Finally an existing computer program for the application in radiology departments, Structural Insight, was improved and largely extended.

In particular the methods of the microstructural calibration, the fractal and the texture operators showed significant improvements of accuracy and precision for the prediction of fracture risk and the quantitative assessment of the progress of Alzheimer's disease, in comparison to existing state-of-the art methods. The methods were tested on artificial and in-vitro data and as well on real-world computed tomography and magnetic resonance imaging (MRI) studies. The proposed novel methods improve the computation of bone characteristics from in-vivo CT and MRI in particular if the methods are combined with each other. In consequence, this allows to assess more information from existing data or to conduct studies with less ray exposure and regarding the MRI method in shorter time than nowadays required.

Nomenclature

Imaging devices

DXA	dual X-Ray absorptiometry
HRMRI	high resolution MRI, applied to ex-situ specimen
HRQCT	clinical high resolution QCT; allows the highest possible image quality, obtainable with standard clinical CT (effective resolution $\approx 300 \times 300 \times 500 \mu m^3$)
HRpQCT	peripheral HRQCT, applied in-vivo to the forearm and leg and ex situ to the vertebra; a CT scanner with a reduced tube diameter, allowing to human peripherals (arms and legs), reaching a higher image quality and resolution than clinical CT (isotropic resolution $\approx 80 \mu m$)
MRI	magnetic resonance imaging
μ CT	micro-CT: CT scanners with highest resolution but very small specimen size used for pre-clinical and material studies (isotropic resolution $0.5 - 100 \mu m$)
QCT	(clinical) quantitative computed tomography
QUS	quantitative ultrasound

CT imaging

bone tissue	hard bone matter part inside a spongy bone
cortex	cortical bone, the outer shell of the bone
DV	density value: calibrated CT values in mg/cm^3
FE	finite element: used to obtain the maximum failure load of bone

HU	Hounsfield unit: unit applied in CT scans, based on absorption of water (0 HU) and air (−1000 HU)
marrow tissue	soft matter inside a spongy bone.
microstructural parameters	refers to certain indices describing the architecture of cancellous bone
μ	linear attenuation coefficient
Osteopenia	early stadium of osteoporosis with T-score between −2.5 and −1
Osteoporosis	a skeletal disorder characterized by compromised bone strength predisposing a person to an increased risk of fracture with T-score smaller −2.5
spongiosa	also cancellous or spongy bone: spongy part inside the bone
T-score	the difference in standard deviations of the patient's BMD in relation to the age-matched average

Densitometry parameters

aBMD	areal bone mineral density: BMD obtained in the 2D plane
BMC	bone mineral content
BMD	bone mineral density
BS	bone surface
BV	bone tissue volume
Ct.Th	cortical thickness
DA	degree of anisotropy
Fr.I	fragmentation index
F_{exp}	experimentally derived maximum failure load
MIL	mean intercept length, a distribution over all orientations
MV	marrow tissue volume
PV	plate volume: volume of bone tissue caught in plates (oblate)
RV	rod volume: volume of bone tissue caught in rods (prolate)

SMI	structure model index
TBS	trabecular bone score
Tb.Di	trabecular distance, average distance between bone ridges
Tb.N	trabecular number, average number of bone ridges per mm
Tb.Sp	trabecular separation, average marrow space
Tb.Th	trabecular thickness, average thickness of bone
TMC or BMCseg	tissue mineral content or segmented BMC
TMD or BMDseg	tissue mineral density or segmented BMD
TV	total volume
$FD_i(\vec{x})$	local fractal dimension obtained with method $i \in \{1, 2\}$ at voxel \vec{x}
$fTb.Th(\vec{x})$	local fractal trabecular thickness at voxel \vec{x}
FD_i	average of $FD_i(\vec{x})$
$FD_i.SD$	standard deviation of $FD_i(\vec{x})$
fRV_i/BV	fractal rod volume/bone volume of $FD_i(\vec{x})$
$fTb.Th$	average of $fTb.Th(\vec{x})$
$fTb.Th.CV$	coefficient of variation of $fTb.Th(\vec{x})$

Image processing and statistic

Bone	signal containing the membership of each voxel of belonging to bone
IQR	inter-quartile range
LTP	long term precision: metric to measure the accuracy/trueness
MED	median
Ridge	fuzzy skeletonization, signal of the bone ridges
ROI	2D region of interest
SKW	skewness, obtained as 3 weighted moment
STP	short term precision: metric to measure the precision/robustness
VOI	3D volume of interest
Voxel	volume element (3D pixel)

QCV	quartile coefficient of variation
$Q_{N\%}$	$N\%$ quantile
\mathcal{N}	general 3D structural element or neighborhood
\mathcal{N}^{Vox}	3D neighborhood-based structural element
\mathcal{N}^{Euc}	3D neighborhood with Euclidean metric
\mathcal{N}^{∞}	3D neighborhood based on the infinite-norm
\mathcal{N}^{Sphere}	3D spherical Euclidean neighborhood with real valued memberships
\mathcal{N}^{Gauss}	3D spherical Gaussian neighborhood
V	volume / 3D image
V^{HU}	volume in Hounsfield units
V^{DV}	volume in density values
V^{Global}	volume in density values, obtained with global microstructural calibration
V^{Local}	volume in density values, obtained with local microstructural calibration
$\vec{\epsilon}$	3D vector depicting the voxel spacing in x-, y- and z-direction
\vec{x}	voxel in a 3D volume V
\vec{c}	point/voxel in a mask or neighborhood \mathcal{N}
λ_i	i 'th eigenvalue ($i \in \{1, 2, 3\}$) obtained from a principal component analysis

Magnetic resonance imaging

Alzheimer's disease (AD)	A chronic neurodegenerative disease causing 60% to 70% of cases of dementia
b-value	reflects the strength and timing of the gradients used to generate diffusion-weighted images
DTI	diffusion tensor imaging
DWI	diffusion weighted imaging
FA	fractional anisotropy
GM	gray matter: brain region containing numerous cell bodies and relatively few myelinated axons.
MD	mean diffusivity

Mild cognitive impairment (MCI)	incipient dementia or isolated memory impairment; may occur as a transitional stage between normal aging and dementia and is often a prodromal stage of Alzheimer's disease
MNI 152 standard space	specific brain atlas defined by McConnell Brain Imaging Centre (MNI) which contains 152 different labeled regions
NEX	number of excitations / number of averages: number of repetitions that were averaged in the final signal
RD	radial diffusivity
TBSS	tract-based spatial statistics
TE	echo time
TR	repetition time
VBA	voxel-based analysis
WM	white matter: brain region containing mainly long-range myelinated axon tracts and very few cell bodies

Chapter 1

Introduction

The impact of Osteoporosis grows annually by 3%, reaching prospectively 10 million cases of hip-fracture in 2050 [25] and annual costs of 200 billion US dollars [51, 118], accompanied with a first year mortality of 10 – 20%. Similarly, worldwide costs for the treatment of Dementia and Alzheimer’s were at 604 billion dollars in 2010 [143] with much lower costs for the treatment of mild dementia than for progressed dementia [86].

Clinical interventions for the treatment of osteoporosis or Alzheimer’s disease are often only performed, if their costs stay in relation to the expected increase of life time [67]. Thus, besides improving the treatment strategies, improvement of computerized radiology methods are required for an early and accurate diagnosis, helping to increase the efficiency and to decrease the overall costs of the treatment.

1.1 Osteoporosis

Osteoporosis reflects an increased fracture risk of the bones. It is defined as a *skeletal disorder characterized by compromised bone strength predisposing a person to an increased risk of fracture. Bone strength primarily reflects the integration of bone density and bone quality* [66]. Bone density refers to mineral content and bone quality means several aspects, such as architecture turnover, damage accumulation and mineralization. *Bone density peaks at an age between 20 and 30 and declines as people age. Hormonal changes, most notably menopause, accelerate this decline. For the purpose of diagnosis, individual bone density is commonly compared to an age-matched reference collective* [49]. This is measured by the T-score, the standard

deviation below the age-matched mean. The World Health Organization defines osteopenia by T-score between -2.5 and -1 and osteoporosis by T-score smaller -2.5 .

Patients with osteoporosis are treated with a diet rich in calcium and vitamin D, also physical exercise, in particular running and jumping stimulates bone formation. For patients with very low T-score, drug diets are required for instance with bisphosphonates or hormone therapies. The use of drugs however depends on the diagnosis, which requires the determination of the individual fracture risk [49]. The T-score as the standard measure of osteoporosis considers only the BMD and age, though it was already shown that bone micro-architecture plays another important role for the overall fracture risk [87]. In particular physical exercise effects a strong reduction of fracture incidence [62] but only a relative low bone density gain of around 1% [145]. Osteoporosis is associated with a deterioration of the complex three-dimensional trabecular network [38].

The anatomical location is an important factor for obtaining the fracture risk since a person can own a strong spine but fragile arms or legs. It is therefore important to measure bone health separately in each particular location [43]. Most important for life quality are the vertebrae and the calcaneus, while bone stability at the forearm contains practically no direct impact to the lifetime expectancy, though much easier to measure. Bone contains the spongy part and the cortical shell. The contribution of the cortex to the mechanical load might be between 45% and 75% [108]. Conversely, since the mechanisms, that form the spongy part and the cortex are tightly connected, the mechanical load can also almost completely attributed to spongy bone [35]. Thus, bone stability can extracted equally from the spongiosa or the cortex. The computation of bone characteristics from the spongiosa has advantages over cortex. The convex shape of the interior of the vertebra allows to assign full memberships to a high number of spongiosa-voxels, while that assignment is difficult for voxels belonging to the cortex, as the real cortex is very thin but appears generally blurred in the CT volumes. This allows to assign well-defined representative volumes of interests to the spongiosa, which contain a sufficient size to deduce significant claims. Furthermore, the variety of existing spongy structural parameters exceeds the one obtainable on the cortex, offering a wider set of possible applications. Finally, the spongy BMD explains about 70% of the failure load, and up to 90% can be explained with BMD in combination with micro structural

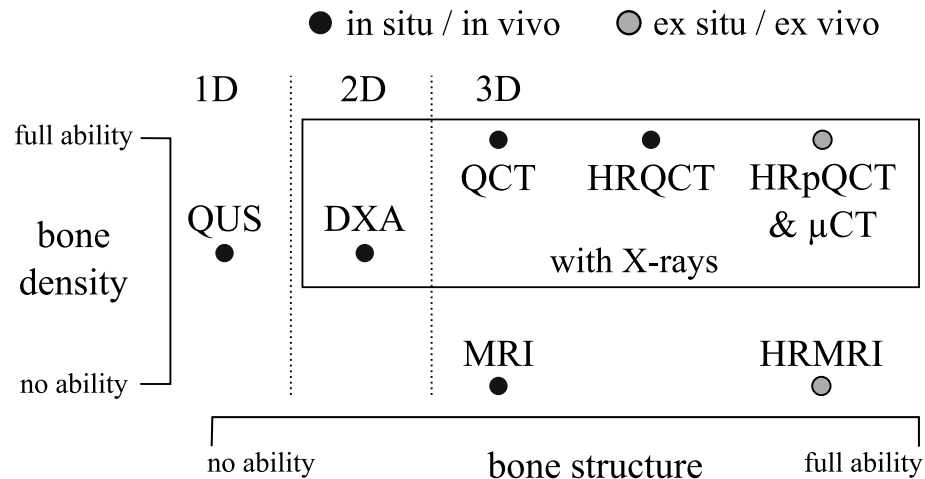


Figure 1.1: Bone measurement modalities ordered by their ability to measure bone density and bone structure. HRQCT is the optimum in-vivo method to obtain bone density and structure.

parameters [140], thus outperforming the 75% contribution of the cortex to the mechanical load.

1.1.1 Imaging modalities

Modalities to measure bone health can be organized in those that do not use X-rays and thus not affect the patient's health and those that use X-rays. Other categories are the ability to measure bone density versus bone quality or the applicability to measure the spine or calcaneus in-vivo versus techniques that apply ex-vivo, Fig. 1.1. In practice also the costs of the devices are important, QUS or DXA devices are most cost efficient, followed by clinical CT devices; MRI is most expensive. Preclinical or peripheral devices (HRpQCT, μ CT or HRMRI) are mostly only used for research and contain additional costs.

Quantitative ultrasound

Quantitative ultrasound (QUS), Fig. 1.2¹, is a 1D technique to measure bone density only, micro structure parameters cannot be obtained, it measures the speed of sound and derives then indirectly the density of the material. Target parameters of QUS

¹Images of Fig. 1.2 are obtained from <http://www.pekinhospital.org/womens-health/womens-diagnostic-center/achilles-express>, https://en.wikipedia.org/wiki/Magnetic_resonance_imaging and <https://www.uclouvain.be/en-98947.html>.

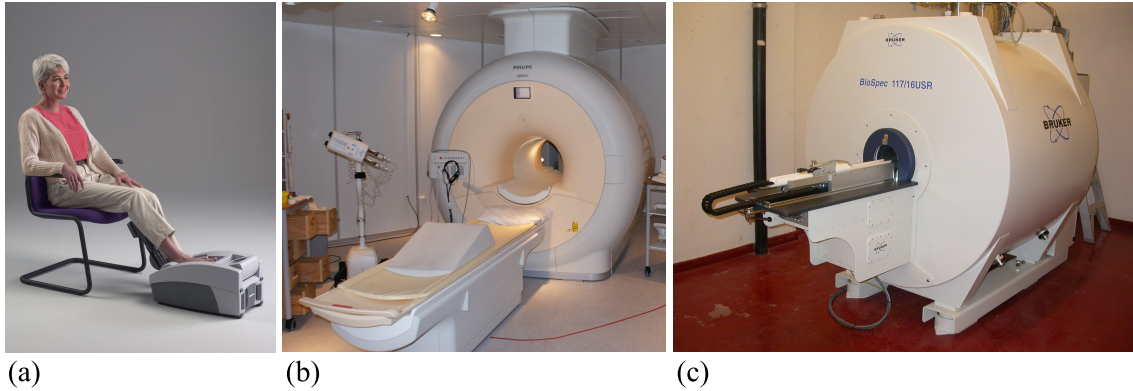


Figure 1.2: Scanners without X-ray technique: a) QUS-Scanner, b) clinical MRI, c) preclinical HRMRI.

are BMC and BMD. It is cost efficient but is only applicable at the extremities (leg or forearm), which are generally not the critical regions for fracture risk [43]. The measurements obtained with QUS are as good as these obtained by 2D DXA [39, 52].

Magnetic resonance imaging

Magnetic resonance imaging (MRI) and high resolution MRI (HRMRI) do not emit x-rays to obtain 3D volumes of the specimen. The nominal resolution depends on the acquisition time, and is for in-vivo MRI $1000 \times 1000 \times 3000 \mu m^3$, however can be much higher on HRMRI ex-vivo studies. Certain MRI protocols are relatively time consuming, thus a common problem of the analysis of in-vivo MRI volumes are motion artifacts. Density measurements are not obtainable, but micro structural parameters can be assessed. Since BMD is however the mayor predictor of fracture risk in osteoporosis, estimations of bone health require generally a combination with X-ray based techniques (for instance DXA). HRMRI is only applicable to ex-situ samples or to mice and rats.

Microscopy

Histology using microscopy is an invasive 2D imaging techniques which is of importance since many of the standard microstructural parameters, such as for instance BV/TV, were originally derived as parameters of 2D histology. An analysis with the microscope allows to visualize much finer levels of detail than all other imaging tech-

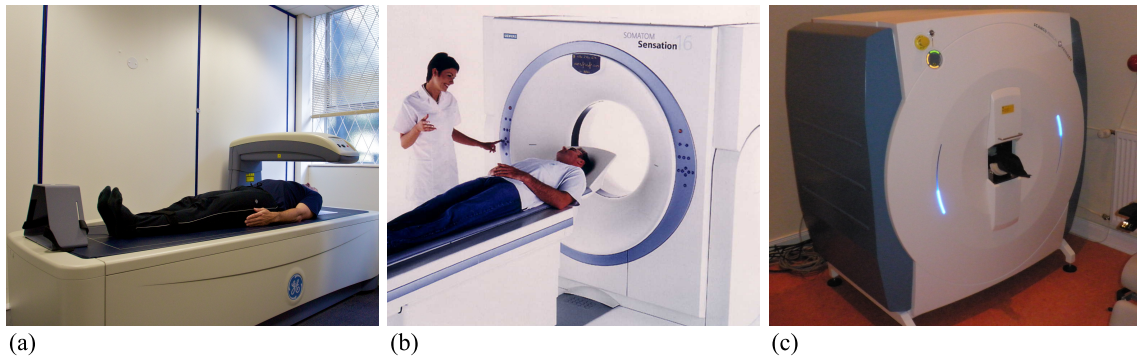


Figure 1.3: Scanners with X-ray technique: a) DXA, b): clinical CT for obtaining QCT and HRQCT scans, c): HRpQCT

niques, in particular the visualization of the osteoblasts and osteoclasts, the highly specialized bone cells responsible for matrix mineralization and demineralization. Types of microscopes, used for such analyzes, are electron microscopy, total internal reflection fluorescence microscopy or internal reflection microscopy [3].

Modalities with ray exposure

X-ray techniques are optimum to measure bone density, Fig. 1.3² For this purpose, the images are calibrated, thus mapping Hounsfield units to density units in $mgcc$ dipotassium phosphate (K_2HPO_4) or calcium-hydroxylapatite ($Ca_5(PO_4)_3(OH)$), both representing the calcium loading. After calibration, the CT scans are called quantitative CT (QCT). For some micro-structural parameters of bone quality, the calibration to density values is not necessarily required. Figure 1.4 shows scans of the same specimen obtained with a pre-clinical HRpQCT device and a clinical HRQCT device. The gap of resolution becomes even more evident when comparing μ CT with standard QCT.

Dual X-ray Absorptiometry

The 2D Dual X-ray Absorptiometry (DXA) has a nominal resolution of $500 \times 500 \mu m^2$ and is intended to access the areal BMD (aBMD). It is the common method for the diagnosis and monitoring of osteoporosis. This technique is low cost and easy to

²Images of Fig. 1.3 are obtained from https://en.wikipedia.org/wiki/Dual-energy_X-ray_absorptiometry, http://www.ascendiahealth.com/028_03_062_007_16slice_ct_applications.jpg and <http://www.osteoporosezentrum-hamburg.de/>.

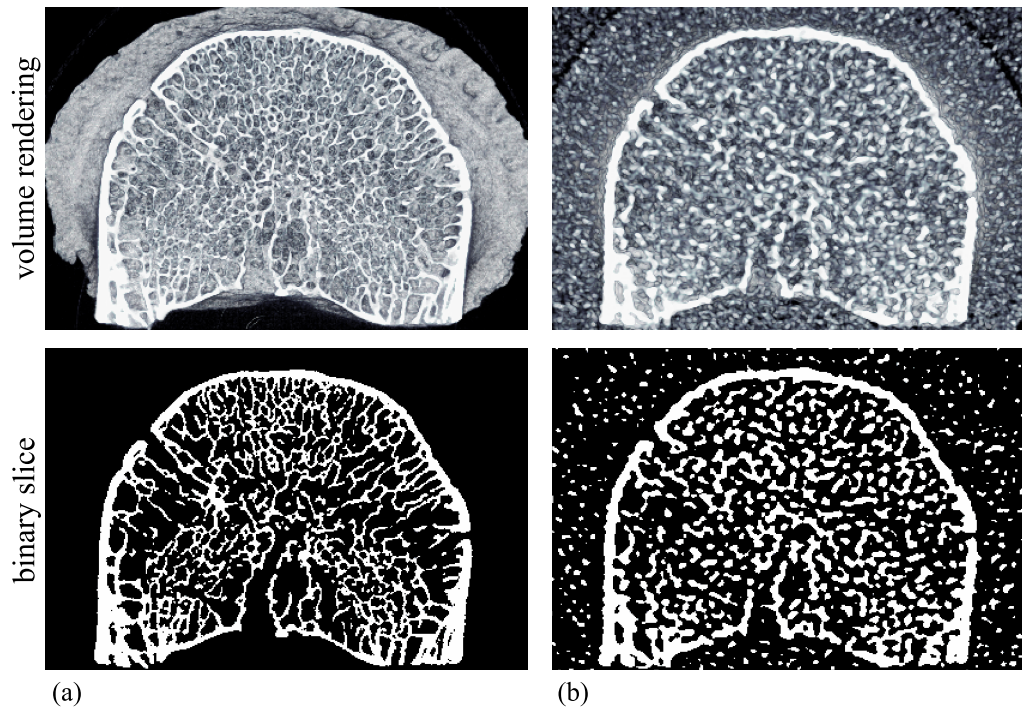


Figure 1.4: Identical human vertebra: a) scanned with a preclinical HRpQCT device, b) scanned with a clinical HRQCT device.

handle and emits only few ray exposure to the patient. It allows also to visualize the macro structure of the skeleton and to access a microstructural parameter, the trabecular bone score (TBS). While its accuracy for bone densitometry is the same as the one of QUS, it allows to obtain measurements directly in the calcaneus or spine. The degree of osteoporosis is computed from the T-score, which contains the aBMD, age and size of the patient. However the assessment of general 3D micro structural parameters, besides TBS, is not possible with DXA.

In-vivo quantitative computed tomography

Clinical quantitative computed tomography (QCT) is 3D imaging technique with nominal resolution $300 \times 300 \times 300 \mu m^3$. Image quality and ray exposure can be adapted depending on the purpose. For the imaging of bone micro structure, generally high resolution QCT (HR-QCT) is used. Standard QCT is only used to measure cortical structural parameters and the trabecular BMD.

Preclinical computed tomography

Peripheral HRQCT (HRpQCT) reaches a nominal resolution of $61 \times 61 \times 61 \mu m^3$ (Scanco XtremeCT II) but is only applicable ex-situ on the spine or the calcaneus. It allows to compute all density and micro structure parameters with high accuracy, thus is often used as a ground truth imaging technique for ex-situ studies. Micro-CT (μ CT) is a preclinical imaging technique with nominal resolution of up to $0.5 \times 0.5 \times 0.5 \mu m^3$ and a image matrix of 8192×8192 pixels (Scanco μ CT 50 in nanoCT-mode). It is solely applicable to ex-situ studies due to the highly limited maximum sample size and the high ray exposure. This imaging technique is often used in animal studies to analyze specific treatment effects. Also it applies for material proofing in non-medical scenarios. A nearly complete list of applications of μ CT can be found at <http://www.scanco.ch/en/applications/applications-overview.html>, including among others scanning of ancient Egypt mummies, quality assurance of pearls, scans of electronic circuits and imaging of diatoms.

1.1.2 Measuring fracture risk

The individual bone strength from HRQCT or QCT volumes can be obtained from two different approaches, directly by simulating the application of an applied force and indirectly by assessing bone characteristics.

FE modeling

The direct way for modeling the stability of the bone micro architecture in physical terms uses the finite element model (FE). This method interprets the bone as an entire structure. The bone is divided in finite models consisting of a few voxels of known density and stability. This set of finite elements is virtually loaded and crushed in a computer simulation, which yields local information of the strength and flexibility. The main application of this approach are virtual crash tests of cars and automobiles and it is worth to note, that FE requires in general a significant amount of computer resources. When applying FE analysis to the computation of bone stability, the results remain often uncertain due to insufficient image resolution, inadequate parceling or just the uncertainty of basic strength and flexibility parameters of the individual elements. Finite element modeling is not explicit topic of this work, nevertheless a number of FE analyses were performed, which used the

computer program Structural Insight, developed for this thesis [20, 41, 19, 79]. FE is expected to become a major analysis technique for HRQCT imaging of the bone.

Micro-structural parameters

The indirect way for estimating bone strength is the analysis of the micro architecture with structural parameters. Each of these structural parameters are an aggregate of the complete volume of interest (VOI) as a single scalar, reflecting a specific feature of the specimen. The estimation of fracture risk or bone stability is then derived from linear models or regression analyses. Accurate accessed structure parameters open a perspective beyond the question about bone strength or fracture risk, they aim to explain changes of the trabecular network during a medical treatment or can be used to describe the structural evolution of bone cancer [13, 12]. Healthy bone for instance shows higher entropy of the trabecular network, which does not imply directly an increased bone strength [134].

Structural parameters like Tb.Sp or BV/TV are standard micro-structural entities in the analysis of trabecular bone and very well understood. The most of these standard parameters were historically developed for 2D histomorphometry or pre-clinical ex-situ resolution, such as obtained with μ CT, HRpQCT or HRMRI. These ex-situ settings contain very high resolution and very low noise. The “structural entity” Tb.Sp was defined before reasonable computer methods for its computation were available. Nowadays exist different methods to calculate the trabecular separation [122, 54, 26, 71], all of these methods deliver distinct results and often new method specific structure parameters, from whom some are difficult to interpret.

In-vivo micro structural parameters

Clinical in-vivo HRQCT is a setting with much coarser resolution as the aforementioned, in particular accompanied with relative high noise besides other additional issues. Technically two different ways exist for the application of micro-structural parameters on clinical HRQCT or QCT resolution. The first approach searches algorithms, that are applicable to in-vivo resolution to compute the well-understood standard parameters, while the second approach seeks parameters that contain the highest ability to predict the fracture risk. Both approaches make sense and are valid, the second method contains however the risk, that the obtained structural parameters are difficult to interpret and thus contain very low meaning if taken for

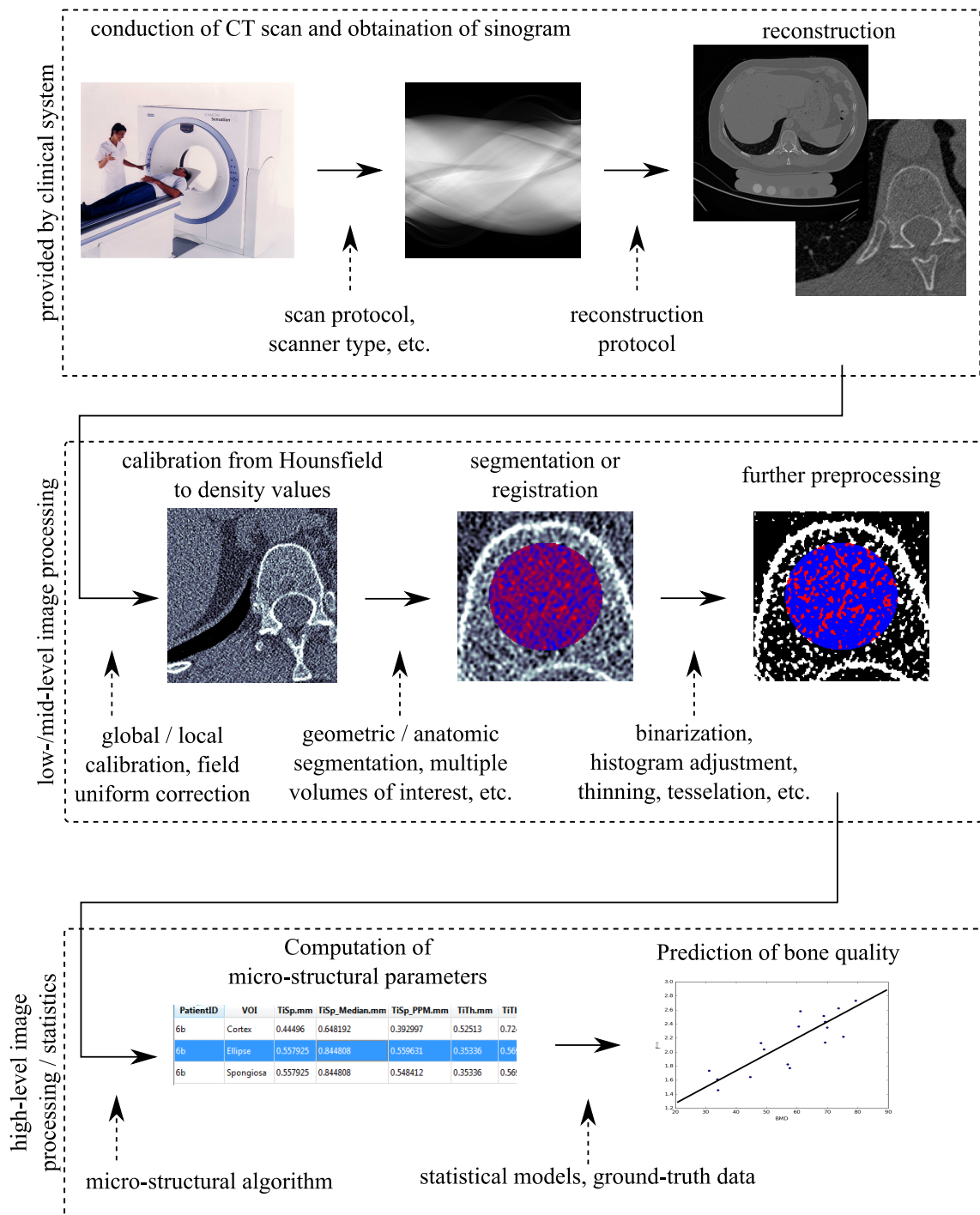


Figure 1.5: Pipeline processing CT images. First row: Scan and reconstruction, second row: Calibration, segmentation and binarization, third row: computation of micro-structural parameters (or FE) and prediction of bone quality.

themselves. The optimum is a method which allows to obtain both, the computation of standard entities on noisy in-vivo input volumes and a high ability to predict the actual fracture risk.

Most important for the translation of micro structural parameters from HRpQCT to QCT domain is the influence of the threshold. Micro structural parameters are generally computed on a binary representation of the volume, hence bone-voxels are coded as ones and marrows as zeros. This reduces the contained information by a factor of 4096, since the input Hounsfield unit of each voxel, typically decoded as a 12bit integer is mapped to 1 bit. While this initial step is unproblematic on HRpQCT, on QCT or HRQCT, the binarization is strongly biased by the low resolution and the high noise. Hence, an adaption of HRpQCT methods to QCT requires to move the binarization and information reduction to a later position in the processing pipeline or to replace the binarization with alternate steps [71].

A second important idea for the computation of micro structural parameters is the concept of fuzziness. Since in-vivo volumes contain uncertainties in the first place, due to low resolution and noise, it sounds obvious that structural parameters based on these input volumes are uncertain as well. The standard algorithms however do not involve the uncertainties. The standard method for the computation of the trabecular thickness for instance computes the radius of the maximum spheres, that fit in the marrow space. When the input volume contains noise, the marrow space is corrupted with pseudo-bone voxels. Hence the direct application of the standard method would compute much lower trabecular separations than on a noise-free volume. However, when allowing the sphere to intersect those noise-generated pseudo-bone, one could still compute the initial trabecular separation, however now as a probability based distribution [90].

Wolfram Timm showed in his PhD thesis [134] how Markov processes can be applied to the micro structural analysis of CT volumes. Markov processes can be interpreted as a special kind of local texture operators, which compute a certain characteristic solely from a local neighborhood or defined range of view. By doing so, the value of each output voxel depends only on a limited and defined set of input voxels and this makes these kind of operators applicable be computed in a very fast manner for instance on Graphics Processing Units (GPUs).

In this thesis, all three concepts, the late or suspended thresholding, the fuzziness and the locality are investigated and combined to extract robust micro structural parameters from in-vivo QCT.

Figure 1.5 shows the typical pipeline of volume processing for obtaining measures of bone quality of fracture risk. While in general all steps contribute to the final outcome, this thesis concentrates in particular on the preprocessing and computation of micro-structural parameters.

1.2 Alzheimer's disease

This work contains an application to magnetic resonance imaging for identifying the severity of the Alzheimer's disease. The computer processing situation in magnetic resonance imaging is similar in terms of the low spatial resolution and the high noise level, which requires similar image processing methods as described in the last section. In particular texture and fractal methods have been applied to MR imaging [58, 59]. However, in contrast to CT, MRI offers a wide set of input volumes, such as scalar ones (T1, T2, etc.) or vector based (Diffusion weighted imaging (DWI), diffusion tensor imaging (DTI), etc.). Most DTI parameters of the white matter in the context of Alzheimers disease, such as fractional anisotropy or mean diffusivity, are only sensible between healthy and unhealthy cohorts [119]. Section 3.6 shows a set of noise robust texture parameters, which were developed during this thesis. These parameters are able to quantify the severity or the progress of Alzheimers disease. Due to the increased sensitivity and precision of the proposed method, this approach might as well gain applicability to further pathologies like Schizophrenia [72] or TDAH [70].

1.3 Aim of the work

In this work, a set of computer methods are presented to access robust in-vivo CT or MRI parameters, using the concepts of locality and fuzziness. To allow comparison of the obtained parameters with existing ones, chapter 2 contains a thorough introduction to general CT volume processing and explains briefly the standard structural parameters. Further information about standard parameters can be found elsewhere [49, 123, 46, 134].

The local operators are applied to an improved pre-processing of the CT volumes, which allows to compute a thinned representation of the bone Sec. 3.3.1 and to improve the calibration of the CT volumes for the computation of micro-structural parameters Sec. 3.3.3. A new method for the computation of the anisotropy of the bone is presented. The anisotropy is computed in a local manner, rather to a global one, Sec. 3.4. This allows to obtain information of the rod volume- or plate volume-ratio. A second method for the computation of the rod volume- and plate volume-ratio is presented in Sec. 3.5, here the information is obtained with a fractal approach, which allows additionally to obtain the trabecular thickness. A direct application of local texture operators is presented in Sec. 3.6, with an application to brain DTI data of patients with Alzheimer's disease. Many of the discussed image processing techniques apply not only to the specific field of CT imaging but as well in other 3D modalities, such as MRI or 2D modalities like satellite and microscopic imaging [109]. In particular the fractal methods are applied not only to image precessing in the medical domain [22, 77, 9] or in the general domain [83, 6, 110] but in particular for the analysis of complex and heterogeneous systems not related with image processing [84, 103, 1, 32, 99]. The last chapter Ch. 4 shows the program Structural Insight, which was developed during this thesis to provide a handy radiology software for the computation of micro structural parameters.

1.4 Hypothesis

It is possible to design methods, which improve significantly the computation of micro-structural parameters on in-vivo QCT if replacing certain image processing steps with more adequate ones, such as a fuzzy binarization, a micro-structural calibration, the use of fractal or scale space methods and fuzzy or weighted neighborhoods, which leads ultimately to

- a better explanation of the micro-structure.
- an improvement of the correlation between ground truth HRpQCT parameters and in-vivo parameters.
- the ability to apply multi-site group studies with different noise spectra with small sample size.

- an improvement of the prediction of failure load and thus to determine osteoporosis.

1.5 Presentation of research

Parts of this research have been presented in several congresses and journals. Full papers in journals or congresses:

1. Felix Thomsen, Claudio Delrieux, Rodrigo de Luis-García: *Local Texture Descriptors for the Assessment of Differences in Diffusion Magnetic Resonance Imaging of the Brain*. **International Journal of Computer Assisted Radiology and Surgery**, 12 (3), pp 389–398 (2017).
2. Graeme Campbell, Jaime Peña, Sarah Giravent, Felix Thomsen, Timo Damm, Claus-C. Glüer, Jan Borggreffe: *Assessment of bone fragility in patients with multiple myeloma using QCT-based finite element modelling*. **Journal of Bone and Mineral Research**, 32 (1), pp 151-156 (2017).
3. Felix Thomsen, Jaime Peña, Yongtao Lu, Gerd Huber, Michael Morlock, Claus-C. Glüer, Claudio Delrieux: *A new algorithm for estimating the rod volume fraction and the trabecular thickness from in vivo computed tomography*. **Medical Physics**, 43 (12), pp 6598–6607 (2016).
4. Jaime Peña, Felix Thomsen, Timo Damm, Graeme Campbell, Jan Bastgen, Reinhard Barkmann, Claus-C. Glüer: *Bone-Marrow Densitometry: Assessment of Marrow Space of Human Vertebrae by Single Energy High Resolution-Quantitative Computed Tomography*. **Medical Physics**, 43 (7), pp 4174–4183 (2016).
5. Jan Borggreffe, Sarah Giravent, Felix Thomsen, Jaime Peña, Graeme Campbell, Asmus Wulff, Andreas Günther, Martin Heller, Claus-C. Glüer: *Association of QCT bone mineral density and bone structure with vertebral fractures in patients with multiple myeloma*. **Journal of Bone and Mineral Research**, 30, pp 1329–1337 (2015).
6. Jan Borggreffe, Sarah Giravent, Graeme Campbell, Felix Thomsen, De-Hua Chang, Mareike Franke, Andreas Günther, Martin Heller, Asmus Wulff: *Association of osteolytic lesions, bone mineral loss and trabecular sclerosis with prevalent vertebral fractures in patients with multiple myeloma*. **European Journal of Radiology**, 84, pp 2269–2274 (2015).

7. Felix Thomsen, Claudio Delrieux: *Soft classification of the plate-rod model using three dimensional rose diagrams* in **Escuela y Workshop Argentino en Ciencias de las Imágenes** (ECIMAG, Buenos Aires, Argentina, 2014), p e140108.
8. Felix Thomsen, Jaime Peña, Jan Bastgen, Beata Hoffmann, Isolde Frieling, Claus-C. Glüer, Claudio Delrieux: *Binary local fractal dimension: a precise structure parameter for 3D high resolution computed tomography images of the human spongiosa* in **Jornadas Argentinas de Informática: Argentine Symposium on Technology** (AST, Córdoba, Argentina, 2013), pp 232–243.
9. Claus-C. Glüer, Matthias Krause, Oleg Museyko, B. Wulff, Graeme Campbell, Timo Damm, Melanie Dauschies, Gerd Huber, Yongtao Lu, Jaime Peña, Sonja Waldhausen, Jan Bastgen, Kerstin Rohde, Stefan Breer, Inga Steinbach, Felix Thomsen, Michael Amling, Reinhard Barkmann, Klaus Engelke, Michael Morlock, Johannes Pfeilschifter, Klaus Püschel: *New horizons for the in vivo assessment of major aspects of bone quality* **Osteologie**, 22, pp 169–248 (2013).

Oral presentations, abstracts and posters:

1. Felix Thomsen, Claus-C. Glüer, Claudio Delrieux: *CT calibration for micro structural parameters on multi-site studies* accepted for **21th International Bone Densitometry Workshop** (IBDW, Bad Staffelstein, Germany, 2017).
2. Felix Thomsen, Jaime Peña, Claudio Delrieux, Claus-C. Glüer: *Structural Insight v3: A stand-alone program for micro structural analysis of computed tomography volumes* in **Jornadas Argentinas de Informática: Argentine Congress of Informatics and Health** (CAIS, Buenos Aires, Argentina, 2016), p. 199.
3. Felix Thomsen: *Analysis of the microstructure of the human vertebral spongiosa with in vivo computed tomography* in **Jornadas de Becarios, Tesistas y Projectistas** (UNS, Bahía Blanca, Argentina, 2016), p. 22.
4. Jan Borggreffe, Nuran Abdullayev, Martin Hellmich, Felix Thomsen, Timo Damm, Jaime Peña, Sonja Waldhausen, Claus-C. Glüer, David Maintz, Barbara Krug: *Veränderungen der computertomografisch erfassten trabekulären Mikrostruktur unter Verwendung von iterativen Rekonstruktionsalgorithmen* in **Deutscher Röntgenkongress: Technik für Menschen** (RöFo, Hamburg, Germany, 2015), p. 187 - WSSP_WISS103_3.

5. Jaime Peña, Graeme Campbell, Timo Damm, Reinhard Barkmann, Sonja Waldhausen, Felix Thomsen, Matthias Krause, Klaus Püschel, Claus-C. Glüer: *Bone Marrow Densitometry by Clinical High Resolution Computed Tomography of Human Vertebrae* in **European Calcified Tissue Society Congress** (ECTS, Prague, Czech Republic, 2014), p. 244.
6. Graeme Campbell, Christian Graeff, Sarah Giravent, Felix Thomsen, Jaime Peña, Asmus Wulff, Andreas Günther, Claus-C. Glüer, Jan Borggrefe: *Prediction of vertebral body stiffness in patients with multiple myeloma using qCT-based finite element models* in **European Calcified Tissue Society Congress** (ECTS, Lisbon, Portugal, 2013), p. 40.
7. Jan Borggrefe, Sarah Giravent, Felix Thomsen, Jaime Peña Asmus Wulff, Andreas Günther, Martin Heller, Claus-C. Glüer: *Knochendichte und Knochenstrukturparameter als Prädiktoren für vertebrale Frakturen von Myelompatienten in der Low-Dose MSCT* in **Deutscher Röntgenkongress: Radiologie ist Zukunft** (RöFo, Hamburg, Germany, 2013), p. 185–VO205_2.
8. Jan Borggrefe, Sarah Giravent, Felix Thomsen, Jaime Peña, Asmus Wulff, Andreas Günther, Martin Heller, Claus-C. Glüer: *Knochendichte und Knochenstruktur bei vertebrealen Frakturen von Myelompatienten? Neue Wege zur Implementierung der QCT Knochendichtemessung im klinischen Alltag* in **Experimentelle Radiologie** (RöFo, Kiel, Germany, 2012), p. 184–A6.
9. Jaime Peña, Sonja Waldhausen, Graeme Campbell, Reinhard Barkmann, Felix Thomsen, Claus-C. Glüer: *Simulation of the Influence of Material Properties and Image Quality on HRQCT-Based Bone Densitometry* in **19th International Bone Densitometry Workshop** (IBDW, Beckenridge, United States of America, 2012).
10. Yongtao Lu, Matthias Krause, Axel Heinemann, Felix Thomsen, Michael Morlock, Gerd Huber: *Influence of different CT scans on bone strength prediction using the finite element method*. **International Symposium on Computer Methods in Biomechanics and Biomedical Engineering** (CMBBE, Berlin, Germany, 2012).

Chapter 2

Standard processing of quantitative computed tomography

This chapter describes the theory of the standard processing methods for the computation of micro-structural parameters. Techniques for the visualization are important to detect issues of the 3D volume, Sec. 2.1. Since computer screens are only able to visualize 2D images, a number of different ways exist for the mapping of 3D volumes, none of those projections own however the ability to depict the entire 3D information. Section 2.2 describes the calibration of the input volume from Hounsfield to density values. This section contains a subsection, describing a method for the automatic placement of the calibration phantom in clinical CT volumes, developed during this thesis. Section 2.3 describes the techniques for the segmentation of the vertebra into its specific volumes of interests. The last section 2.4 describes the standard techniques to conduct micro-structural parameters, including certain generalizations. The parameters described here were used in the following chapter 3 as reference values. The chapter ends with a discussion and conclusion section about the standard methods.

2.1 Visualization of 3D volumes

For visualizing 3D CT volumes on a computer screen, certain circumstances need to be considered. CT volumes contain at every voxel the **Hounsfield unit**, rather

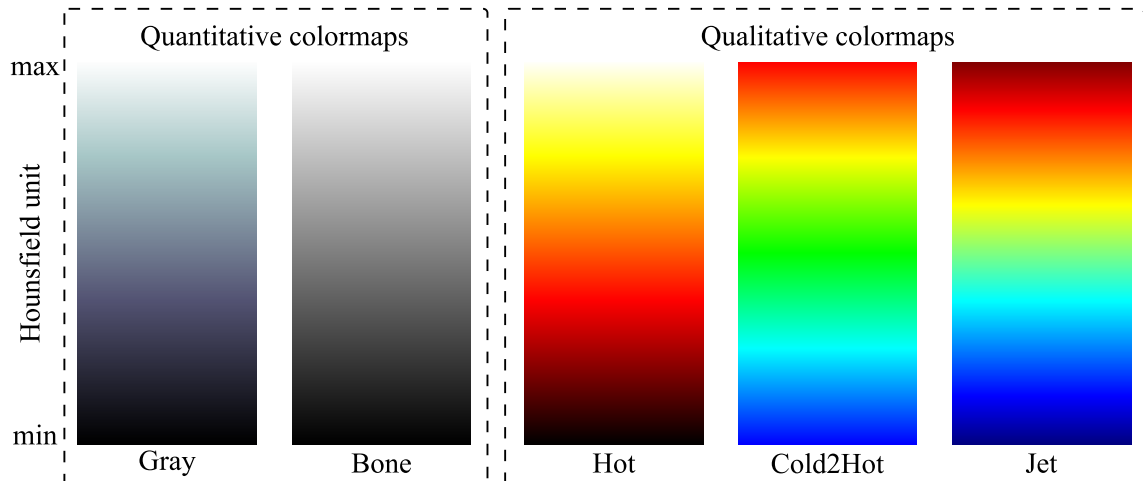


Figure 2.1: Five sample colormaps for the qualitative and quantitative visualization.

than a specific gray-value or color, as in photographs. The Hounsfield units need to be displayed to colors with a specific colormap. For the visual quantitative analysis, most commonly the gray value or bone colormaps are used. The hot, jet- and cold2hot-colormap are more adequate for a qualitative analysis of the Hounsfield units. Figure 2.1 shows sample colormaps used for the visualization of such data.

There exists no standard setting of **contrast** and **brightness** since Hounsfield units are unlimited, in contrast to photographs which occupy for instance color values between 0 and 255 only. The HU of air is -1000 and the one of metal can be higher than 5000, human tissue and bone cover typically a range between 100 and 3000.

The 3D volume must be **projected** to the 2D plane or screen. The 2D projection is defined by a **projection angle** and the **projection range**, the first and last plane, defining the subset of the 3D volume. If fixing the projection angle to zero degrees and the projection range to the entire volume, the 3D volume can be interpreted as a stack of 2D images, Fig. 2.2 (a). When interpreting the voxel values of every x-y-pixel on the screen as a 1D function of z-values, Fig. 2.2 (b). The standard projection is the slice projection, which returns the 2D image at a certain z-coordinate, Fig. 2.2 (c), statistical maps are e.g. the maximum, minimum, average, standard deviation and range projection, Fig. 2.2 (d-g). The maximum intensity projection (MIP) serves for instance to detect pulmonar nodule and the minimum intensity projection (MinIP) to detect pulmonar emphysema. True volumetric projections, that suggest the ability to watch inside the volume are the depth field-

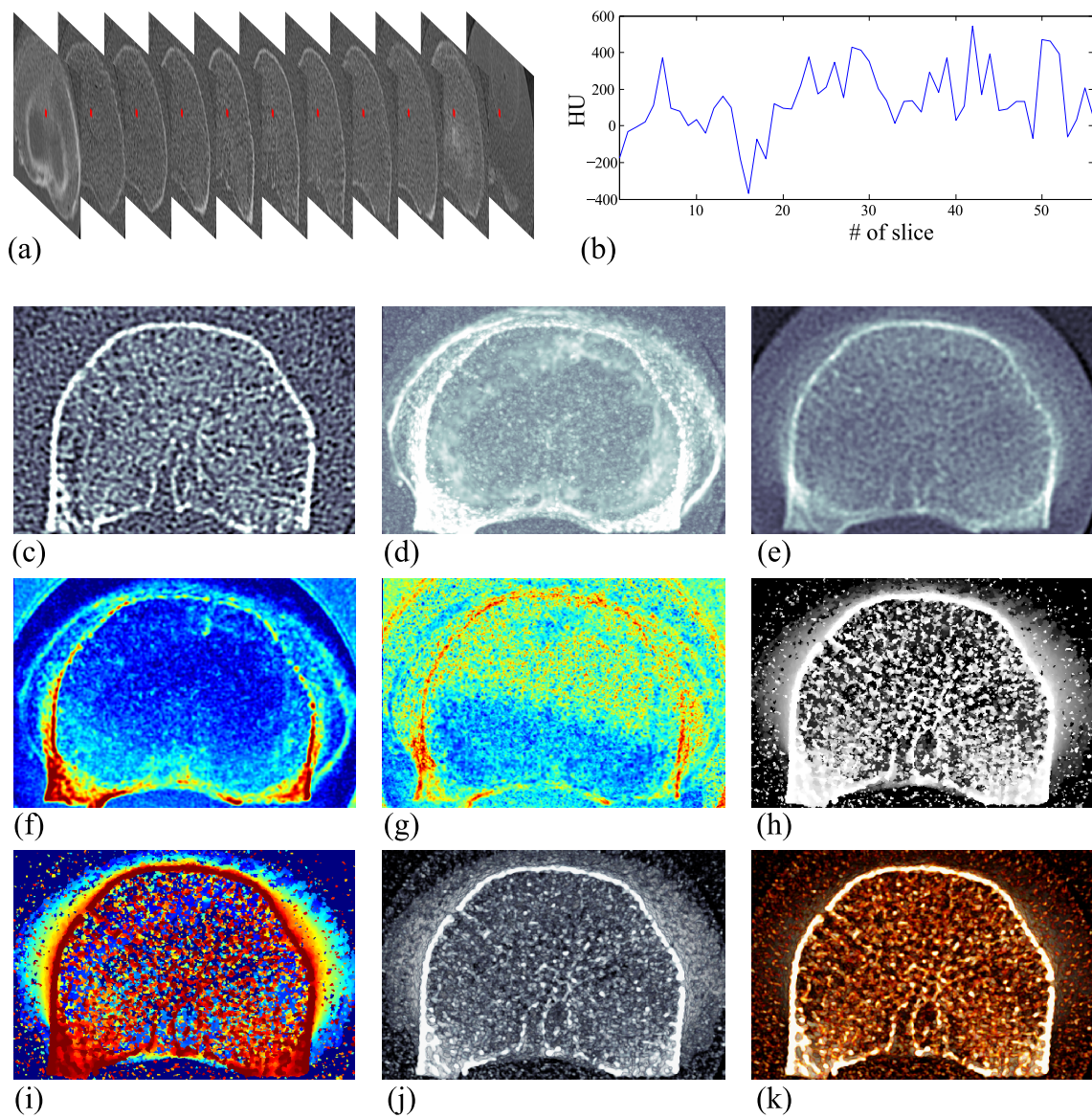


Figure 2.2: 3D projections. (a) Interpretation as a stack of 2D images, (b) sample evolution of the HU-values in z-direction at a certain x-y-pixel, (c) slice projection, (d) maximum intensity projection (MIP), (e) average intensity projection, (f) standard deviation projection, (g) standard deviation by range projection (SD/range), (h+i) depth-field projection with gray- (h) and jet-colormap (i), (j+k) ray casting with bone- (j) and copper-colormap (k).

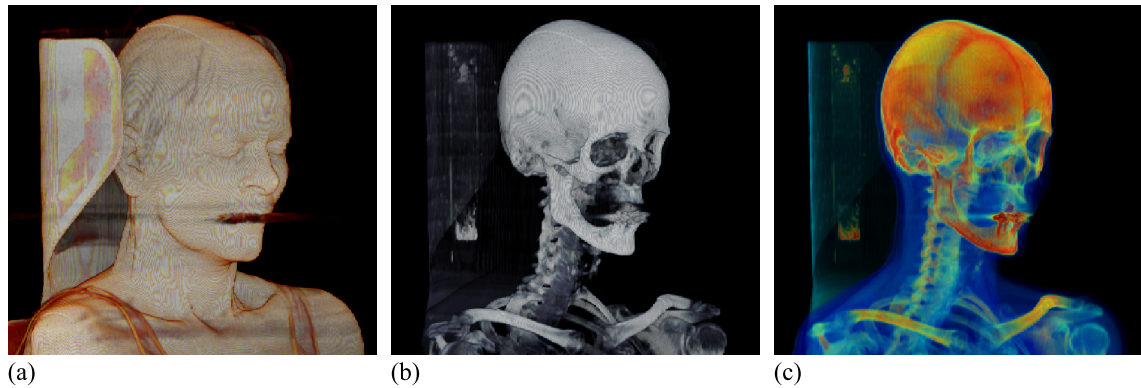


Figure 2.3: Three examples of ray casting. (a) high opacity values visualize the surface (skin), (b) low opacity values visualize the hard tissue (bone), (c) a wide range of opacities with a qualitative colormap allow to visualize both, the skin and the skeleton. The artifact in the region of the patient's mouth is generated by metal.

and the ray casting-projection. The depth field projection returns the index of the uppermost slice, whose voxel value exceeds a given threshold, Fig.2.2 (h+i). The ray-casting projection assigns every voxel a specific color and translucency value, varying from opacity to transparency. The object can be imagined as a 3D matrix of glass-cubes of different colors and transparencies. The resulting 2D image is the aggregation color if watching the object from the front, Fig.2.2 (j+k). By varying the specific color- and opacity map, the ray casting projection can visualize the skin or soft tissue Fig.2.3 (a), bone tissue (b) or even both together (c).

2.2 Density-calibration of CT volumes

The calibration of the CT data serves to map the data from Hounsfield units HU to density scale mg/cm^3 . A CT scan, which is not expressed in HU but instead in density values is called quantitative CT (QCT). The Hounsfield units (HU) are normalized linear attenuation coefficients $\mu \geq 0$, which fix the values of water (HU=0) and air (HU=-1000). Since the linear attenuation coefficient of air is zero, the simplified linear relationship reads

$$\text{HU}(\mu) = 1000 \left(\frac{\mu - \mu_{\text{water}}}{\mu_{\text{water}}} \right). \quad (2.1)$$

Substance	$\mu(\text{cm}^{-1})$	HU	$DV_1(\text{mg}/\text{cm}^3)$	$DV_2(\text{mg}/\text{cm}^3)$
Air	0	-1000	-767.1	-775.6
Fat	[0.141, 0.149]	[-100, -50]	[-92, -55]	[-83, -44]
Water	0.157	0	-17.1	-5.6
Soft tissue	[0.173, 0.204]	[100, 300]	[58, 208]	[71, 225]
Bone	[0.267, 0.629]	[700, 3000]	[508, 2233]	[533, 2304]

Table 2.1: Linear attenuation coefficients for 75 keV [16], Hounsfield units and corresponding calibrated apparent densities using DV_1 [24] and DV_2 [117] of common substances.

In practice, that map is only linear for low emission energies (75 keV) while for higher emission energies the map consists two linear relationships with a lower slope for negative HU's and higher slope for positive HU's [15]. A volume expressed in HU's can be transformed to density values $DV(\text{mg}/\text{cm}^3)$ with a linear mapping,

$$DV(\text{HU}) = \alpha \text{HU} + \beta, \quad (2.2)$$

where DV are the density values and HU the Hounsfield units. This mapping produces also negative values, however the density in bone and soft tissue remains positive. Negative values appear only at voxels that contain fat, air, water and noise. Jaime Peña investigated during the conduction of his PhD thesis the apparent density in regions containing fat or air [100, 101, 102]. The practical reason for the choice of this linear mapping is the distribution of the noise. A non-linear mapping, disallowing negative values, would generate noise, that were dependent on the actual density value and would in consequence affect the computation of the BMD, which is only exact, if the noise is independent of the actual density. Hence, since the relationship between HU and DV is generally non-linear, the Eq. 2.2 applies only for cortical and trabecular bone, but not for the quantification of soft tissue [24]. The Hounsfield units of common substances are shown in Tab. 2.1 together with sample maps between HU and densities: $DV_1 = 0.75 \text{HU} - 17.1$, [24] and $DV_2 = 0.77 \text{HU} - 5.6$, [117].

Since the map between HU's and DV's is linear, the calibration is in general unnecessary for the analysis of the micro-structure, when the analysis is performed on a binary representation. In particular if the segmentation threshold is based on a fixed BV/TV rather than on a density value, the corresponding threshold can be directly derived from the corresponding histogram, either of the DV's or HU's. The

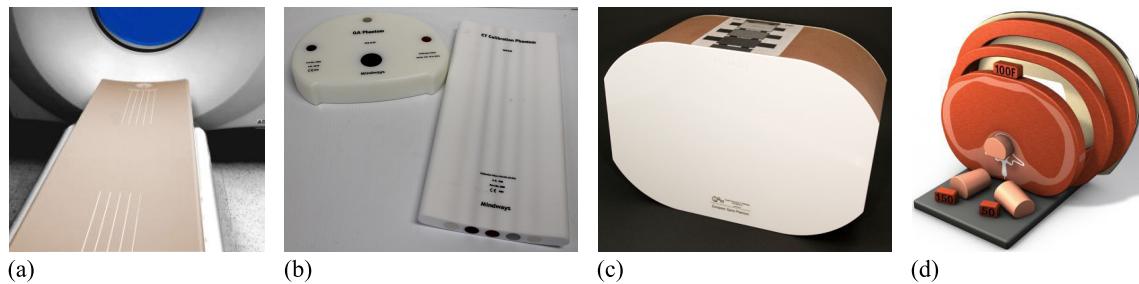


Figure 2.4: Different calibration phantoms. a) Image Analysis InTable phantom, b) Mindways calibration and quality assurance phantom, c) European spine phantom from QRM GmbH, d) combined quality assurance and body phantom from Tissue Simulation & Phantom Technology, which can be used with different inserts.

particular values of α and β vary with the noise level, which is influenced by the patient's size and the scan protocol. The calibration parameters can also vary inside the same scan, thus one can compute values of α and β separately for each slice, which is a local calibration.

The computation of the parameters of Eq. 2.2 are performed with the aid of a calibration phantom, which must be placed under the patient during the scan, Fig. 2.4. The calibration phantoms contain at least two different rods filled with a bone-equivalent of different known densities. Common substances are calcium-hydroxylapatite $\text{Ca}_5(\text{PO}_4)_3(\text{OH})$, sometimes also called HA, which is the main inorganic part of bones (bone mineral) and standard in modern calibration phantoms, an alternative calcium equivalent is dipotassium phosphate K_2HPO_4 , a highly water soluble salt. The mapping is then computed from a linear fit of the mean HU's of each rod and each slice and the defined physical bone-densities. Sometimes, a field uniform correction (FUC) factor is involved, which aims to map the density values under the patient to the desired location in the patient.

$$\text{DV}_{\text{FUC}} = \text{FUC} \cdot \text{DV}. \quad (2.3)$$

However, the use of a FUC can downgrade the calibration, in particular if the distance between the calibration phantom and the area of interest is not constant. The FUC itself is obtained with a quality assurance (QA) phantom, which simulates the intersection of a human but contains known densities. The FUC can be obtained with special quality assurance phantoms, Fig. 2.4 (b-d), for instance with the European Spine phantom, Fig. 2.5.

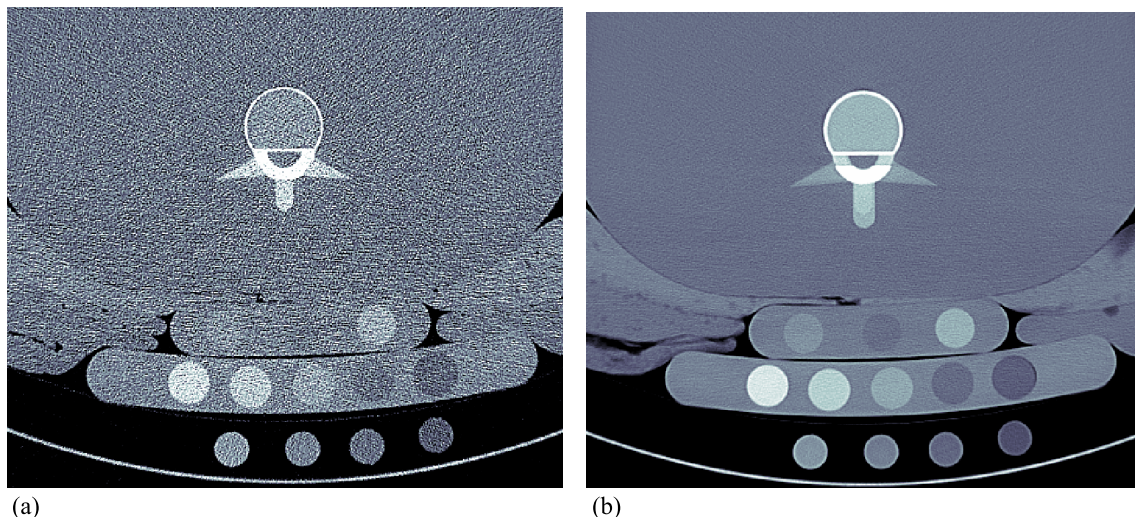


Figure 2.5: High resolution CT scan (120kV, 340mAs), containing a QA phantom (European spine phantom from QRM GmbH) and 3 different calibration phantoms: from bottom to top: InTable from Image Analysis (4 rods), Model 3 from Mindways (5 rods) and a phantom from the Hamburg-Harburg University of Technology (3 rods). (a) Noise-level of each slice, (b) noise reduction by averaging in z-direction.

2.2.1 Automatic placing of the calibration phantom

The critical step in the calibration procedure is to obtain the actual calibration parameters α and β which requires to fit a mask of the calibration phantom to the actual volume data. A procedure for the automatized placing of the calibration phantom was developed for this study and applied to the HRQCT data of the EuroGiops study [33, 42]. The performing by hand is time consuming and less accurate than the proposed automatic procedure. The procedure uses the circular Hough-transform of an edge presentation, which generates peaks in the center of the circles. The center coordinates of every tube at each slice can be obtained by the following algorithm in five steps: (1) Smooth slice i in z-direction by taking the point-wise average of the slices $i - n, \dots, i + n$, Fig. 2.5 and Fig. 2.6(a). (2) Apply the 2D Monogenic signal (see Sec. 3.3.2) as an edge detector and to obtain information of the local orientation, Fig. 2.6(b). (3) Apply a Circle-Hough-transform of the binary result of the edge detection with weighting according to the desired orientation, Fig. 2.6(c). (4) Filter the local maxima. (5) Reduce the number of the global maxima to m points and match the phantom, Fig. 2.6(d).

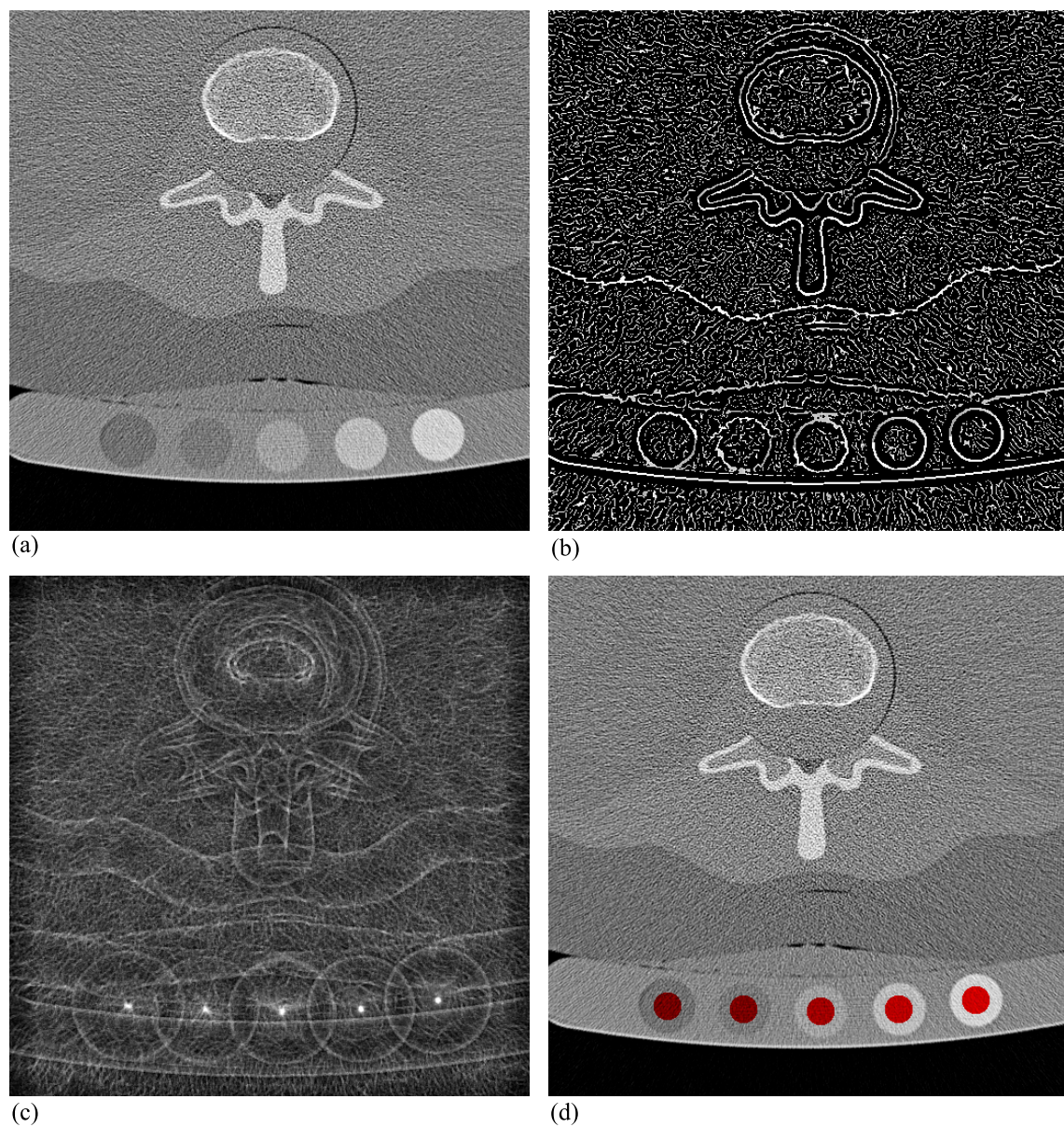


Figure 2.6: Sample steps of the segmentation of the calibration phantom. (a) Input slice, (b) result of the edge detection, the gray-values encode orientations. (c) result of the circle-Hough-transform respecting the orientation. (d) final positions of the matching between the local maxima of (c) and the phantom.

The phase and orientation of the 2D Monogenic signal [34, 128] was used to perform the edge detection of the second step of the algorithm. The edge detection was based on the Monogenic phase ϕ and the orientation $\theta = \arctan(f_x/f_y)$. The orientation-weighted circular Hough-Transform accumulates for every pixel \vec{x} the pixels of a circle with radius r . Let $\vec{c}_1, \dots, \vec{c}_N$ be the offsets of these the N points of the circle,

$$\vec{c}_i = \left\langle r \cos \left(\frac{2i\pi}{N} \right), r \sin \left(\frac{2i\pi}{N} \right) \right\rangle \quad (2.4)$$

then the accumulated intensity of the edges reads

$$\text{ACC}_r(\vec{x}) = \frac{1}{N} \sum_{i=1}^N \begin{cases} |\cos(\theta(\vec{x} + \vec{c}_i) - \frac{2i\pi}{N})| & \text{if } \sin(\phi(\vec{x} + \vec{c}_i)) > (1 - \epsilon) \\ 0 & \text{otherwise} \end{cases} \quad (2.5)$$

with $\theta \in [0, \pi]$ the orientation of the gradient, ϕ the monogenic phase and $\epsilon = 0.05$ a threshold accuracy. The accumulator adds $1/N$ for every pixel on the edge of the circle, if the orientation on the edge-pixels points to the center of the circle. The image of the local maxima is computed via,

$$\text{MAX}(\vec{x}) = \begin{cases} \text{ACC}_r(\vec{x}) & \text{if } (\text{ACC}_r \oplus \mathcal{N}_r^{\text{Euc}})(\vec{x}) = \text{ACC}_r(\vec{x}) \\ 0 & \text{otherwise} \end{cases} \quad (2.6)$$

with \oplus the morphological dilation and $\mathcal{N}_r^{\text{Euc}}$ the 2D circular structural element with radius r (see Sec. 3.2.1). The reduction to the m strongest maxima serves to facilitate the final matching. If the calibration phantom is rigid, this operation must only be computed for two slices with a sufficient distance in z-direction to derive the 3D pose and rotation of the calibration phantom. Though if the phantom is deformable, as for instance the InTable phantom, the coordinates of the rods must be computed for every slice and subsequently smoothed with a local median operator.

2.3 Segmentation of the volume of interest

The segmentation or definition of the volume (VOI) or region of interest (ROI) is a common step in nearly all image processing tasks, when structures or shapes have to be identified. Many different segmentation techniques have been defined that apply not only to medical images but also for instance to 2D satellite imaging or photographs [109]. The principal advantage of 3D segmentation in comparison

to segmentation of 2D images is the increased numbers of local neighbors, which increases the statistical accuracy. There are however also a number of specific issues, which arise on (medical) 3D volumes.

- The segmentation of biological shapes is generally a complex task, in particular when the pathology represents a deviation from the common shape or texture. The accuracy of the segmentation has often relevant implications for the diagnosis and the succeeding treatment of the patient. Full automatic and unsupervised segmentation functions require much higher success rates than in most non-medical contexts and are thus mostly inconceivable.
- CT volumes contain generally a high noise level, since image quality and patient's ray exposure are correlated. That means, the ray exposure has to be the least possible to maintain just the minimum needed image quality to perform the required task.
- The low resolution of CT volumes might induce uncertainties at the boundary of the segmented anatomical region. In this case, a non-exclusive fuzzy segmentation is required, which assigns two or more anatomical regions with each a given probability to the same voxel.
- CT volumes contain only one band, the gray value information of the HU's, which impedes under certain circumstances the detection of areas or borders. In contrast, areas or borders in color photographs or satellite images are often detectable in multiple bands.
- Certain image processing tasks become ambiguous when switching from 2D to 3D. The (fine scale) segmentation of the skeleton for instance requires a-priori assumptions in which case a given portion of voxels has to be reduced to a plate-like or a rod-like structure.

The planned analysis determines often the actual segmentation technique. For the analysis of the micro structure of the spongiosa or generally the texture inside an anatomical region, it is relevant that the volume of interest is representative, coherent and large enough to yield statistically significant measures. In most cases a geometric segmentation with a predefined mask, shaped as a cylinder, box or ball, is sufficient and recommendable.

For measuring quantitative properties of the volume of interest, like the total volume or the cortical thickness, the entire anatomical region needs to be segmented. This requires generally more complex and specialized segmentation methods, an increased effort of time and knowledge about the anatomy. In general, such a segmentation is based on a combination of seed-point placement by the user and iterative automatic adaptations of the volume of interest. The input data needs to be transformed to a reasonable representation for instance using texture operators in combination with border detection. Also pyramid approaches are very common that compute an initial segmentation on a very coarse resolution which is then refined with every finer resolution. The final segmentation is often based on a 3D mesh of the boundaries of the anatomical region of interest.

2.3.1 Segmentation by registration

Registration or matching with an atlas is a special case of segmentation, which can often be performed without further user interaction. By using this procedure, an already performed segmentation, the atlas or baseline, is rotated, translated and sometimes distorted to fit the actual volume. Two different kinds are distinguished: the rigid registration, which consists on rotation and translation only, thus contains only 6 free parameters and the deformable registration. The deformable registration contains additionally to the 6 free parameters of the rigid registration a complete volume of translation vectors for every voxel. Each of these both registration techniques exist in two forms. The registration can either be applied on the volume data of the current scan or the inverse registration can be applied to the baseline scan. Similar to the choice of the optimum segmentation technique, also the registration method depends on the intended purpose of analysis.

The **deformable registration of a prototype baseline** scan applies for instance as a first step of the segmentation of the entire vertebra into spongiosa, vertical cortex, upper and lower endplate, foramen and so on. Here, the volume data remains fixed and the anatomical regions are deformed to fit the physical anatomical locations. It can also be used for the segmentation of follow-up scans of the same patient, if a segmentation of the baseline scan was already performed and if a change of the shape or size of the volume of interest is expected, as for instance on children that are still in growth or for monitoring and measuring cancer.

The **deformable registration to atlas space** is the inverse technique of the aforementioned one. It applies for instance for the registration of MRI volumes of the brain. Each voxel in the registered volume stands for a predefined anatomical region. The actual volume data itself is distorted, hence particular voxels become squeezed or stretched to fit the predefined anatomical regions in atlas space. This kind of registration allows to apply a voxel-based analysis (VBA) where each voxel is interpreted as a separate VOI and compared between different patients.

For the analysis of the temporal change of a vertebra, only a single scan has to be segmented in a traditional way, for instance the baseline scan. The follow-up scans can then be segmented with a **rigid registration of the volume data**. A baseline and follow-up scan can be compared directly on the voxel-level, which allows for instance to subtract volumes and to compute 2D histograms of the evolution of the density values. A critical step with this kind of registration is the choice of the interpolator. Interpolation with the nearest neighbor does not affect the histogram, however contains the poorest spatial accordance, the trilinear as the other extreme contains good spatial accordance between baseline and follow-up scan but decreases the variance of the volume data, since it flattens the local peaks. The B-spline interpolation can be considered as a compromise of both techniques. Another technique for avoiding systematic differences between the histogram of the baseline and the follow-up scan can be the artificial degradation of the baseline image data. Here a non-trivial random rotation (no multiples of 45 degrees) has to be initially applied to the baseline scan, using the same interpolator as for the registration of the follow-up scan.

Rigid registration of the mask applies when the comparison between baseline and follow-up scan can be performed on a parameter level rather than on the voxel level. It does not bias the actual image data of the follow-up scan, since it applies the inverse registration matrix to the volume-of-interest of the baseline scan. Hence, the histogram of the follow-up scan is not degraded and no explicit interpolation is involved. Since the rigid registration does not adapt the shape or size of the volume of interest, only qualitative micro-structural parameters can be evaluated between baseline and follow-up scan. That means that in particular the total volume or the cortical thickness is not obtainable. Conversely the robustness of the evaluation of qualitative parameters like for instance BV/TV is generally superior with a rigid registration, since it is ensured that the same anatomical locations are compared.

It is worth to note that all of the mentioned registration techniques are only applicable if the baseline and the follow-up scan contain a sufficiently high number of unambiguous landmarks. Hence the registration between two volumes of interest of noisy spongiosa is only feasible if the image volume contains the entire cortex or at least a sufficiently large portion of the cortex.

2.4 Microstructural parameters

The computation of microstructural parameters can be subdivided into a low-level and the high-level image processing part. The low-level image preprocessing aims to transform the image into a representation to facilitate the computation of structural parameters. The outcome of certain methods for the computation of bone characteristics depends only on the preprocessing step. For instance the BMD and the BV/TV utilize both the same high-level method, the average gray value, though on different low-level processed volumes. The signal for the BMD is the calibrated volume while the signal for the BV/TV is the binary representation of the bone.

Three classes of structural methods can be distinguished: the point-wise, the local and the global parameters.

- Voxel- or point-wise parameters, such as BMD or BV/TV are based on voxel-counting. Each voxel is considered as an independent unity and spatial relations and neighborhoods are not considered.
- Local parameters, such as the star-volume, the trabecular thickness with the thickness-transform method and most of the proposed robust parameters proposed in Ch. 3 are based on a local neighborhood. The preprocessing value of each voxel results from a local neighborhood, and the information of the spatial location of each voxel is conserved until the very last aggregation step.
- The strict global parameters are obtained from a transformation or map to parameter space, such as for instance a histogram, the Fourier transform or the non-local box-counting fractal dimension. The information of the spatial location gets lost but information of the spatial or structural relations of all voxels are contained in parameter space. The direct secant method is an example of such a global method, it uses the histogram of the mean intercept lengths as its parameter space. The structural parameter is generally derived

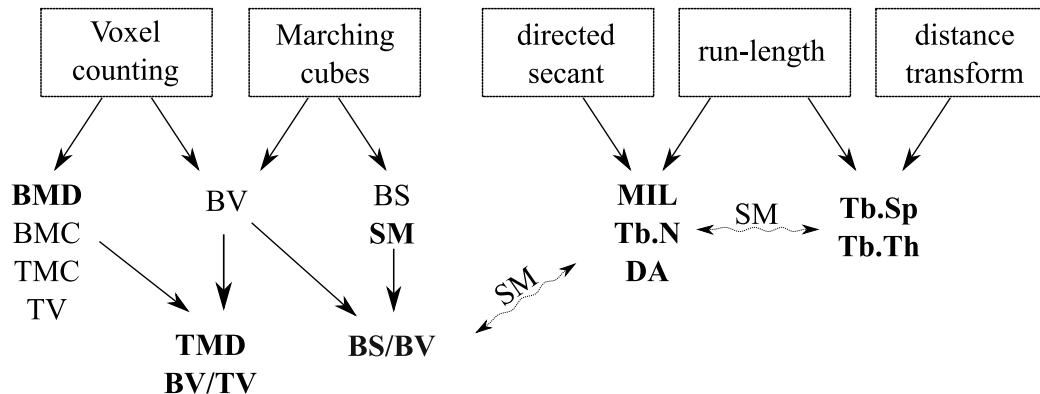


Figure 2.7: Most important morphometric methods and derived quantities. Bold measures are relative measures that apply for the characterization of bone health. The structure model (SM) relates BS/BV, Tb.N, Tb.Th and Tb.Sp.

as the average or median over this histogram. It is worth to note that any global method can serve as a local texture parameter by computing the global parameter for each voxel on a separate locally restricted VOI.

The three classes of methods have in common the final aggregation of the obtained measures to one scalar value per VOI, the global micro-structural parameter. Figure 2.7 shows the relation of the proposed methods and obtainable structural parameters which are originally defined for HRpQCT resolution. Some particular structural parameters (e.g. Tb.Sp or BS/BV) can be derived from multiple methods.

The next subsections contains a formal definition of global parameter, Sec. 2.4.1 and of the conduction of the binary representation of the volume, Sec. 2.4.2. Then, the standard methods are reviewed, Fig. 2.7. Some further information of the actual implementation is provided in the chapter about the computer program Structural Insight, Ch. 4, in particular in Sec. 4.4.

2.4.1 Global parameters

A microstructural parameter is mathematically a scalar value which describes a certain property of the VOI. The particular nature of each parameter is defined by (1) a specific preprocessing, which generates a distribution, and (2) an aggregation method that extracts a certain characteristic from the distribution. Let $s_i \in \mathbb{R}$ be the local signal and $w_i \in \mathbb{R}_{\geq 0}$ a weighting of each item s_i . Formulas for the linear operators are based on weighted cumulants [107]. First, the following parameters

are defined,

$$W_p = \sum_i w_i^p \text{ and} \quad (2.7)$$

$$S_p = \sum_i w_i s_i^p. \quad (2.8)$$

Now, the first two weighted cumulants read

$$K_1 = S_1/W_1 \text{ and} \quad (2.9)$$

$$K_2 = (S_2W_1 - S_1^2)/(W_1^2 - W_2). \quad (2.10)$$

The nonlinear operators are computed from weighted quantiles. Let $\xi(1) \dots \xi(N)$ a labeling of the indices, which induces an ascending sorting of the values s_i : $\forall i \in \{1, \dots, N-1\} : s_{\xi(i)} \leq s_{\xi(i+1)}$. The weighted quantile at a given percentile $Pr \in [0, 1]$ reads now:

$$Q_{Pr} = s_{\xi(j)} : \sum_{i=1}^{j-1} w_{\xi(i)} < Pr / \sum_{i=1}^N w_i \leq \sum_{i=1}^j w_{\xi(i)} \quad (2.11)$$

From the definitions above, the following global parameters can be extracted:

- the weighted average,

$$\text{AVG}(s, w) = K_1 \quad (2.12)$$

- the weighted standard deviation,

$$\text{SD}(s, w) = K_2^{(1/2)} \quad (2.13)$$

- the weighted coefficient of variation,

$$\text{CV}(s, w) = K_2^{(1/2)} / K_1 \quad (2.14)$$

- the weighted median,

$$\text{MED}(s, w) = Q_{50\%} \quad (2.15)$$

Under the condition $\forall i, j : w(i) = w(j) > 0$, these global parameters become un-weighted and are in this work expressed as $\text{AVG}(x)$, $\text{SD}(x)$, $\text{MED}(x)$ and so forth.

Additionally the minimum and maximum are always independent of w ,

$$\min(s, w) = Q_{0\%} = \min(x), \quad (2.16)$$

$$\max(s, w) = Q_{100\%} = \max(x). \quad (2.17)$$

2.4.2 The bone map

Most standard micro-structural parameters need a volume containing the likeliness or segmentation of each voxel belonging to bone or marrow. The map which reflects the bone membership is called $\text{Bone}(\vec{x})$. It is typically achieved by applying a transfer map to the input volume V . The simplest form of defining Bone is the application of a crisp threshold t ,

$$\text{Bone}_t(\vec{x}) = \begin{cases} 1, & \text{if } V(\vec{x}) > t \\ 0, & \text{otherwise} \end{cases} \quad (2.18)$$

with V mostly but not necessarily expressed in density values V^{DV} . The optimum choice of t is in practice often an issue [48]. The global threshold is the simplest one, but there exist more sophisticated techniques to map V to $\{0, 1\}$ [142]. A probability function obtained with a crisp threshold contains only two states: 1 for bone and 0 for marrow but it can be generalized to a fuzzy threshold or a real probability function $\text{Bone} \in (0, 1)$, for instance by applying a sigmoidal membership function using the cumulative normal distribution,

$$\text{Bone}_{(t,\sigma)}(\vec{x}) = \Phi_{t,\sigma}(V(\vec{x})) = \frac{1}{\sqrt{2\sigma^2\pi}} \exp\left(-\frac{(u-t)^2}{2\sigma^2}\right) du \quad (2.19)$$

where t is the value where Bone is 0.5 and $\sigma \geq 0$ is the fuzziness factor. Figure 2.8 shows the application to a CT scan for t at the 75% quantile and different choices of σ . For $\sigma \rightarrow \infty$, Bone approximates the linearity,

$$\text{Bone}_{(t,\sigma \rightarrow \infty)}(\vec{x}) \approx 0.5 + \frac{V(\vec{x}) - t}{\sqrt{2\pi\sigma^2}}. \quad (2.20)$$

This condition can be generalized, hence Bone is always ‘‘quasi linear’’ in the interval $[t - \sigma, t + \sigma]$, see Fig. 2.8. For $\sigma > 0$, the original density map can be reconstructed with the inverse cumulative normal distribution Φ^{-1} , hence the fuzzy transform does

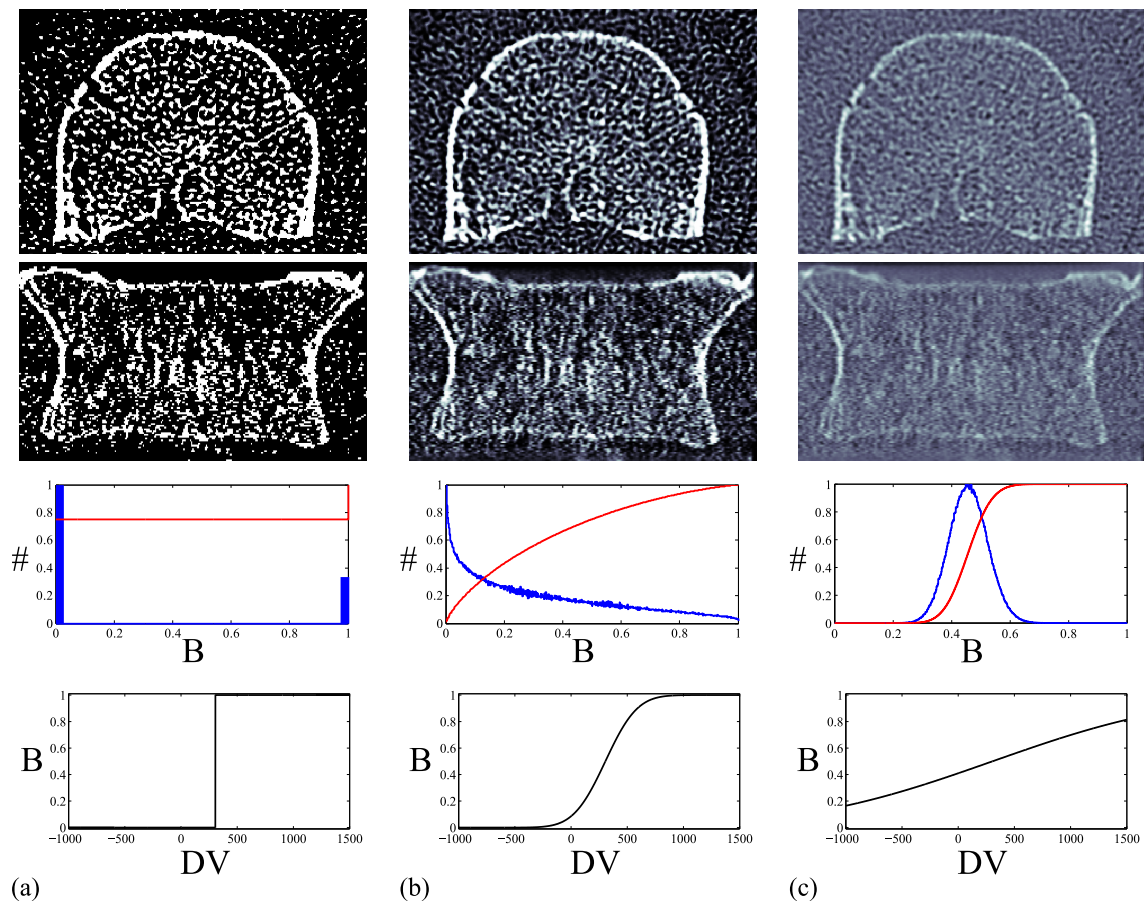


Figure 2.8: Application of the sigmoid function $\text{Bone}_{t,\sigma}$ with t the BMD and varying σ , a) $\text{Bone}_{(\text{BMD},0)}$, b) $\text{Bone}_{(\text{BMD},\text{SD})}$, c) $\text{Bone}_{(\text{BMD},6\text{SD})}$. Rows: 1) transversal view, 2) coronal view, 3) histogram (blue) and cumulative histogram (red) of $\text{Bone}_{t,\sigma}$, 4) map between DV's and $\text{Bone}_{t,\sigma}$.

not discard any information,

$$V(\vec{x}) = \Phi_{t,\sigma}^{-1}(\text{Bone}_{(t,\sigma)}(\vec{x})). \quad (2.21)$$

At the singularity $\sigma = 0$, the map becomes the classical crisp binarization, which cannot be anymore reconstructed,

$$\text{Bone}_{(t,0)}(\vec{x}) = \text{Bone}_t(\vec{x}). \quad (2.22)$$

The value σ defines the difference between the energy of the noise at t and vs. values with an higher offset to t . The correct definition of σ is steered by two

opposed mechanisms, by decreasing σ , the apparent probabilities of Bone become more certain, hence closer to 0 or 1, by increasing σ , the trueness of the signal Bone, in particular at t , increases while meanwhile less voxels contain a clear membership to either bone or marrow.

In practice it is important to chose the values of t and σ with care. Sometimes, in particular when dealing with group studies (compare Ch. 3), separate values of t and σ might apply to each site. One might also define t in terms of the average quantile instead of a fixed density. If V^{DV} was derived with a global calibration, Bone can be likewise computed on V^{HU} or V^{DV} , with t and σ respectively expressed in HU or in mg/cm^3 .

Since defining Bone by transfer functions only does not incorporate local texture information, differences of the point-spread function are not treated. This implies that increasing the threshold lowers the Tb.Th but disconnects simultaneously the bone phase. The following subsections discuss approaches to avoid a disconnection of the bone phase.

2.4.3 Voxel counting

The voxel counting method (VC) extracts structural information without modeling relations between adjacent voxels. The direct measures obtained with this method are the the bone mineral density, the bone volume ratio and tissue mineral density. The bone mineral density reads

$$\text{BMD}[\text{mg}/\text{cm}^3] = \text{AVG}(V^{DV}), \quad (2.23)$$

the bone volume ratio reads

$$\text{BV}/\text{TV}[\text{cm}^3] = \text{AVG}(\text{Bone}) \quad (2.24)$$

and the tissue mineral density reads

$$\text{TMD}[\text{mg}/\text{cm}^3] = \text{AVG}(V^{DV}, \text{Bone}). \quad (2.25)$$

From the measure total volume (TV)

$$\text{TV}[\text{cm}^3] = |\vec{x}| = \sum_{\vec{x}} \prod \epsilon_i, \quad (2.26)$$

and the voxel spacing $\vec{\epsilon} = \langle \epsilon_1, \epsilon_2, \epsilon_3 \rangle$. The following quantitative measures can be computed: bone mineral content,

$$\text{BMC}[\text{mg}] = \text{TV BMD} = \prod \epsilon_i \sum_{\vec{x}} V^{\text{DV}}(\vec{x}), \quad (2.27)$$

bone volume,

$$\text{BV}[\text{cm}^3] = \prod \epsilon_i \sum_{\vec{x}} \text{Bone}(\vec{x}) \quad (2.28)$$

and tissue mineral content,

$$\text{TMC}[\text{mg}] = \text{BV TMD} = \prod \epsilon_i \sum_{\vec{x}} V^{\text{DV}}(\vec{x}) \text{Bone}(\vec{x}). \quad (2.29)$$

For parameters that use Bone, generally a crisp threshold in mg/cm^3 is used, for instance Bone_{200} , but also fuzzy threshold functions are possible, $\text{Bone}_{(200,100)}$.

2.4.4 Marching Cubes

The marching cubes method (MC) [78, 21] is an alternative method to access the bone volume, it yields additionally the model independent bone surface (BS) and can be used to get insights of the structure model with the structure model index (SMI) [53] or trabecular bone pattern factor (TBPf) [47]. MC transforms the voxel representation into a polygon mesh. An object of the polygon mesh is defined by 8 voxels taking into account the 8 phases and their local density. The authors of the original paper stated 15 different configurations, how the boundaries can be aligned in the polygon objects, see Fig. 2.9. The exact positions of the triangles inside the cubes are defined by the actual BV/TV's of the 8 voxels. The BS and the BV determined by this method appear more natural (see Fig. 2.10 adapted from [88]). The BS is already smoother in the MC-representation, Fig. 2.10 b), but to assess an optimal representation, the triangle mesh needs to be smoothed with an a-posteriori smoothing operation, which minimizes the energy at the corners of the triangles. This improves the BS and as well the BV, but can also suppress high frequency

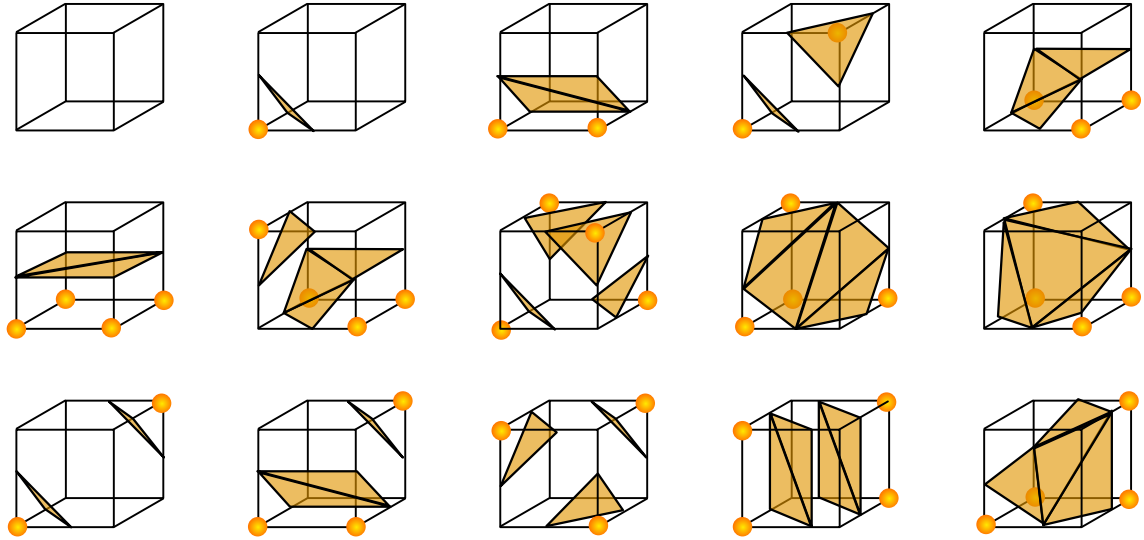


Figure 2.9: Original published 15 prototypes of the Marching Cubes algorithm. The actual position of the triangles is derived by linear interpolation between adjacent local BV/TV's.

information, if too many iterations are applied. An extension of this method uses 33 prototypes by dividing some of the 15 prototypes into sub-cases depending on the actual BV/TV's, [21].

The Bone surface generated with MC is dependent on the scale. Small details are erased during the iterative smoothing operations or absent due to too low effective resolution. Cipoletti et al. [23] introduced a method to apply a fractal extrapolation to the estimation of the boundary of a 2D structure by examination of the fractal slope of the results of down-sampled representations. This approach can also be applied to 3D.

2.4.5 Direct secant method and run-length method

The direct secant method (DSM) [98, 122] computes the distribution of intercept lengths, which defines the mean intercept length (MIL) and degree of anisotropy (DA). In combination with a model of the structure model, for instance parallel plate model (PPM), one can also derive the Tb.Th and Tb.Sp. The DSM uses a parallel grid of search rays intersecting the VOI. The compound phases of bone or marrow on the search rays are summarized to p_θ . The lengths of the search rays are summarized to l_θ , both for a set of examined orientations $\theta_1, \dots, \theta_n$. Every

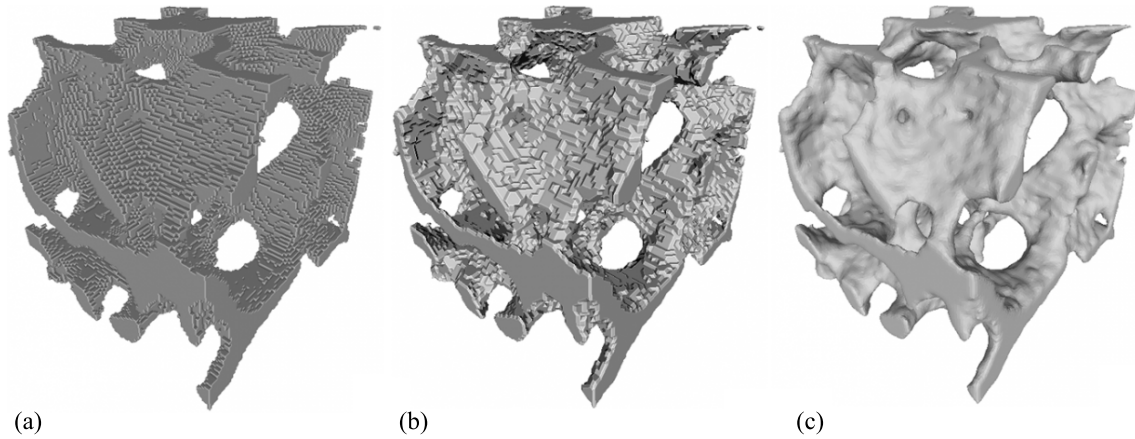


Figure 2.10: Comparison of the BV with voxel counting and marching cubes. The three images show one sample meshed in different ways: a) the mesh shows the voxels of the samples, b) simple triangulation of the surface, c) same as b) but smoothed with 2 iteration steps.

orientation defines a mean intercept length (MIL_θ):

$$MIL_\theta = \frac{l_\theta}{p_\theta} \quad (2.30)$$

The Tb.Di is the average of all MIL's:

$$Tb.Di = \frac{\sum_\theta MIL_\theta}{n} \quad (2.31)$$

and the Tb.N is its reciprocal, when using the parallel plate model:

$$Tb.N = 1/Tb.Di. \quad (2.32)$$

The different examined orientations to configure a nearly regular grid on the surface of a unit sphere and were achieved from [50]. To prevent a bias induced by the size of the VOI, the method can be modified as follows: The examined rays do not start just inside the VOI but outside at the next phase change. The first line segment, which is cutting the VOI contributes to the length l_θ and the phase sum p_θ only with the ratio of voxels, which lay inside the VOI. The run-length method (RLM) [30] is a variant of the direct secant method, which does not only count the phase changes and the complete length of the ray but instead the lengths of the all line-segments

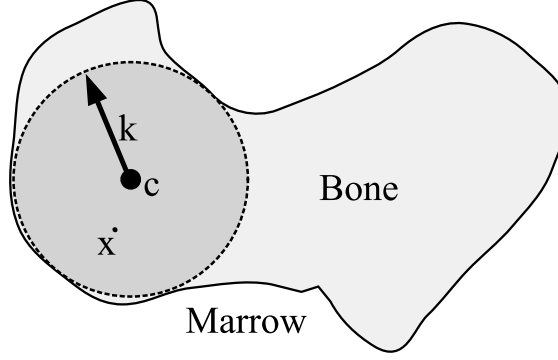


Figure 2.11: Distance transform method: The sphere $\mathcal{N}_k^{\text{Euc}}(\vec{c})$ is entirely contained in the bone phase Bone. The thickness at \vec{x} is $2k$ since the depicted sphere with radius k and center \vec{c} is the maximum possible sphere that contains \vec{x} .

of the marrow or bone phase. The histogram of the marrow phases follows a power law and the Tb.Sp is defined as the median. The same can be done for Tb.Th.

2.4.6 Distance transform method

The Distance transform method (DT) was introduced by Hildebrand and Rüegsegger [54]. It is defined for μCT resolution and assumes a binarization of the 3D volume. This method is the most widely used method for estimating thickness on segmented images because it is model independent and intuitive. It serves to calculate the Tb.Sp and Tb.Th. The bone and marrow phase are separately analyzed. The Tb.Sp is locally calculated for every point \vec{x} of the marrow phase as the diameter of the largest sphere which fits in the marrow space and contains \vec{x} . Note that the center \vec{c} of this largest sphere $\mathcal{N}_k^{\text{Euc}}$ can differ from the examined point \vec{x} , see Fig. 2.11,

$$\text{Th}(\vec{x}) = 2 \max\{k \mid \|\vec{c} - \vec{x}\|_2 < k, \mathcal{N}_k^{\text{Euc}}(\vec{c}) \subseteq \text{Bone}\}. \quad (2.33)$$

The authors of the original paper use the Euclidean distance transform to generate the thickness representation from the binary phase image Bone:

- Create an Euclidean distance transform DT of the binary volume Bone.
- Initialize a thickness map Th with zeros.
- Compute the local thickness for every voxel:

$$\forall \vec{c} \in \text{Bone} \wedge \forall \vec{x} \in \mathcal{N}_k^{\text{Euc}} \text{DT}(\vec{c}) : \text{Th}(\vec{x}) = \max(\text{Th}(\vec{x}), 2 \text{DT}(\vec{c})). \quad (2.34)$$

- Aggregate the local thickness for the entire VOI in one structural variable Tb.Th:

$$\text{Tb.Th} = \sum_{\vec{x} \in \text{Bone}} \text{Th}(\vec{x})/\text{BV} \quad (2.35)$$

The same method is used to compute the Tb.Sp, but by replacing Bone with $1 - \text{Bone}$. Improvements of that method can be achieved by up-sampling the volume with a factor of 2, because the distance transform calculates the radius but not the diameter. This method is defined for binary images, and does not take into account any noise treatment, which makes it problematic to apply this method directly to HRQCT images.

The distance transform method is used for two settings, the computation of the cortical thickness and the computation of cancellous parameters. The computation of the cortical thickness uses only the segmentation mask, thus does not require a threshold, while the segmentation into bone and marrow on the spongiosa is derived from the threshold binarization. Additionally to the standard parameters of the distance transform method, Graeff suggests a weighted thickness and separation at every voxel [46]:

$$wTh(\vec{x}) = Th(\vec{x}) (V^{DV}(\vec{x}) - DV^{\text{Marrow}})/(DV^{\text{Bone}} - DV^{\text{Marrow}}) \quad (2.36)$$

$$wSp(\vec{x}) = Sp(\vec{x}) (DV^{\text{Bone}} - V^{DV}(\vec{x}))/ (DV^{\text{Bone}} - DV^{\text{Marrow}}) \quad (2.37)$$

with Th the thickness transform of a voxel of the bone phase, Sp the thickness transform of a voxel of the marrow phase and $DV^{\text{Bone}} = 1200\text{mg}/\text{cm}^3$ the density at full mineralization and $DV^{\text{Marrow}} = 0\text{mg}/\text{cm}^3$ the density of marrow tissue. Finally, the average and standard deviation over all values inside the VOI are computed. Alternatively to wTh and wSp , the sigmoidal bone membership $\text{Bone}_{(t,\sigma)}$ can be used as the weighting function:

$$wTh^*(\vec{x}) = Th(\vec{x}) \text{Bone}_{(t,\sigma)}(\vec{x}) \quad (2.38)$$

$$wSp^*(\vec{x}) = Sp(\vec{x}) (1 - \text{Bone}_{(t,\sigma)}(\vec{x})) \quad (2.39)$$

Extensions of the distance transform method

The fuzzy distance transform [113] is an alternative to the Euclidean distance transform. It can be meaningful to replace the straight Euclidean distance with the fuzzy

distance, if the roughness of the surface shall be included or the object boundaries are weakly defined [127]. As the boundaries of the bone phase are uncertain, the obtained parameter is the trabecular distance (Tb.Di) rather than the trabecular separation Tb.Sp (Tb.Di = Tb.Sp + Tb.Th). In this context, the fuzzy distance transform has been used for the computation of the trabecular distance from an initial hard skeletonization [26], and alternatively to compute a thinning of the bone structure [71], thus replacing an Euclidean skeletonization.

The granulometric distance transform was suggested by Moreno et al. [90]. The first 3 steps of the DT-algorithm are equivalent to the result of an morphological opening procedure with 3D spheres as structure elements. As the morphological opening is not only defined for binary volumes but as well for gray-value volumes, it is possible to calculate the Tb.Sp direct on the texture. The so derived Tb.Sp is a fuzzy Tb.Sp, which is not induced by the fuzzy distance transform but instead a fuzzy version of the Euclidean distance transform: Every point is assigned a distribution of memberships by Euclidean distances. The non-fuzzy approach generates only one (maximal) distance, which owns the assigned membership of one. Here every point owns a large number of distances, thus the thickness map *Th* (compare Eq. 2.33) becomes 4 dimensional, rendering this algorithm more complex to understand and in terms of run-time.

The distance transform was also modified by using anisotropic Euclidean distances [29]. Instead of fitting the maximum sphere inside the bone phase, ellipsoids with the maximum volume are fitted. This allows to extend the number of derived structural parameters to local anisotropy measures, which relate the moduli of the 3 principal axes $\lambda_1 \geq \lambda_2 \geq \lambda_3$ of the ellipsoids to each other, for instance

$$\text{Degree of anisotropy} = \lambda_1/\lambda_3 \in [1, \infty) \quad (2.40)$$

$$\text{Isotropy index} = \lambda_3/\lambda_1 \in [0, 1] \quad (2.41)$$

$$\text{Elongation index} = 1 - \lambda_3/\lambda_1 \in [0, 1] \quad (2.42)$$

However, this method is at least as sensitive to noise, as the original distance transform method, hence not yet applicable to clinical CT.

2.4.7 Further standard methods and issues

Another method to obtain Tb.Sp and Tb.Th is the star volume method, which follows a similar idea than the distance transform, but obtains the distance measure only over some angles. Euler characteristics and the box counting dimension are also implemented, though not standard in the literature. A list and a short description of the standard methods can be obtained from <http://bruker-microct.com/next/CTAn03.pdf>, <http://bonej.org/> and from [98, 46, 49].

Sometimes a specific resampling method for CT volumes is used [57]. This method upsamples the volume to a sufficient high isotropic resolution, such that every voxel has a full or void mineralization. It is designed for the case of having only two different phases: bone and marrow. A voxel is iteratively split into 8 sub-voxels, with the information of the 27-neighborhood. This method was for instance used as a preprocessing step of a 3D skeletonization [112].

The central issue of standard methods is their generally poor performance on clinical in-vivo data since the early application of the threshold discards an important portion of information. When applying the standard methods to clinical QCT, the structural fine scale frequencies cannot be assessed. Hence, only parameters that are defined for coarse scale frequencies, for instance the BMD, are computable. Structural parameters require certain techniques to either recover or extrapolate the fine scale frequencies [23, 57]. Some of those approaches are developed in the following chapter. Alternatively, the reconstruction from the obtained CT data in Radon space to spatial domain can be improved.

2.5 Reconstruction techniques

Iterative reconstruction methods are an alternative to the standard reconstruction with filtered back projection. While iterative reconstruction methods have been applied to chest and lung scanning [64], only few studies have yet been conducted to investigate the importance for the computation of micro-structural parameters [11, 14].

Figure 2.12 shows the data obtained for an ongoing study on that issue. The filtered back projection with increased exposure is used to obtain the ground truth structural information. Different iterative reconstruction methods, implemented by Philips and Siemens will be investigated, some of these iDose 1 and 5 or IMR 1-2P

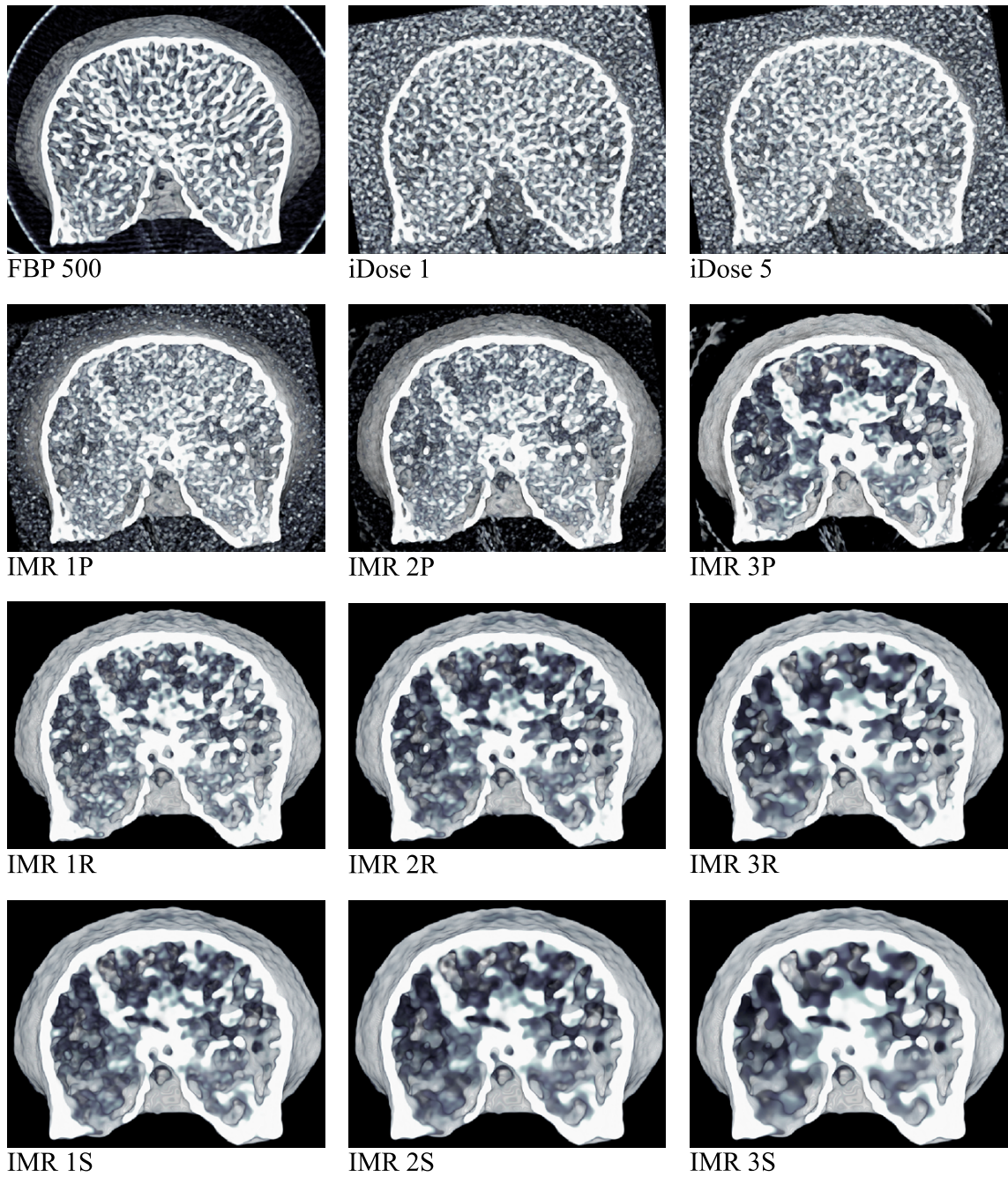


Figure 2.12: Iterative reconstruction methods for a HRQCT scan with 120 kV: filtered back-projection with 500 mAs (FBP 500), iterative reconstructions for same vertebra but 360 mAs: Philips iDose 1 and 5, iterative model reconstructions (IMR), type 1-3 P, 1-3 R and 1-3 S.

seem to maintain the structural information by simultaneously suppressing noise, while others IMR 1-3S and IMR 1-3R suppress not only noise but discard also significant portions of the structural fine scale information.

Chapter 3

Robust microstructural CT parameters for in-vivo data

The computation of microstructural parameters from clinical volumes contains several issues. If several patients are compared in a group study, the obtained parameters must be invariant of systematic changes in between the obtained cases. Sources of systematic differences between CT volumes can be due to different problems:

- In hospitals, the used CT scanners are periodically replaced with new models. The new CT scanners contain generally not only improved mechanical parts but often also improved reconstruction software, such as the availability of iterative reconstruction algorithms. These aspects not only provide more comfort to the radiologists and patients but also improve the quality of the obtained data in terms of decreased noise and increased effective spatial and frequency resolution. While these improvements are beneficial for the ad-hoc analysis of patient data, it might impair the ability to compare data obtained with the former scanner.
- When the same CT scanner is used for the entire study-data it is common that small changes of the scan and reconstruction protocols involve large implications for the computed microstructure parameters. For instance differences in ray exposure, voltage, table height, and variations of the reconstruction kernels imply differences of the noise level. Changes of the spatial resolution (or field-of-view) change the range of the obtained frequencies and thus also bias most of the microstructure parameters.

- The preparation of the patient or specimen also influences the obtained image quality: the image quality of a particular slice decreases if that slice contains more physical material, or if the ray on its way through the volume passes many edges. The image quality of an in-vivo scan of the T12 increases if the patient puts his arms over his head during the scan. Bolus bags serve to fill eventual free gaps between the lounger and the body or specimen. Finally, different noise levels can be observed between obese and thin persons.
- The calibration phantom can be another source of impairments. Firstly, different calibration phantoms or different calibration substances imply also differences in the obtained density values. Secondly, the physical distance between the calibration phantom and the VOI biases the calibration, this is sometimes corrected with the field-uniform correction (FUC). Finally, the kind of calibration (global vs local calibration or manual vs automatic calibration) might also be a source of differences between scans.

There are basically two concepts that deal with the compensation of differences between obtained scans. With adequate preprocessing methods, the volumes can be elevated to a common noise and resolution format. The obtained microstructure parameters contain then a similar resolution and noise spectrum and hence gain comparability between each other.

The other approach deals directly with a (re-)formulation of the microstructural parameters. Parameters that base on scale-space or fractal methods are known to be robust against resolution issues. Also robustness against noise or against blurring can be obtained by incorporating particular information of the noise spectrum or the point-spread function. First, the used volume data is presented in Sec. 3.1, then the principal concept of local parameters is explained in Sec. 3.2. Methods of CT-preprocessing are discussed in Sec. 3.3. The next two sections describe two different approaches for the computation of the rod-volume- or plate-volume-fraction ratio. The first approach, Sec. 3.4, uses 3D rose diagrams and the second uses a local fractal dimension, Sec. 3.5. Finally, a direct application of the local texture descriptors is presented, using instead of CT volumes magnetic resonance volumes, Sec. 3.6. This allows the direct application of a voxel-based analysis without the need of an a-posteriori global aggregation method.

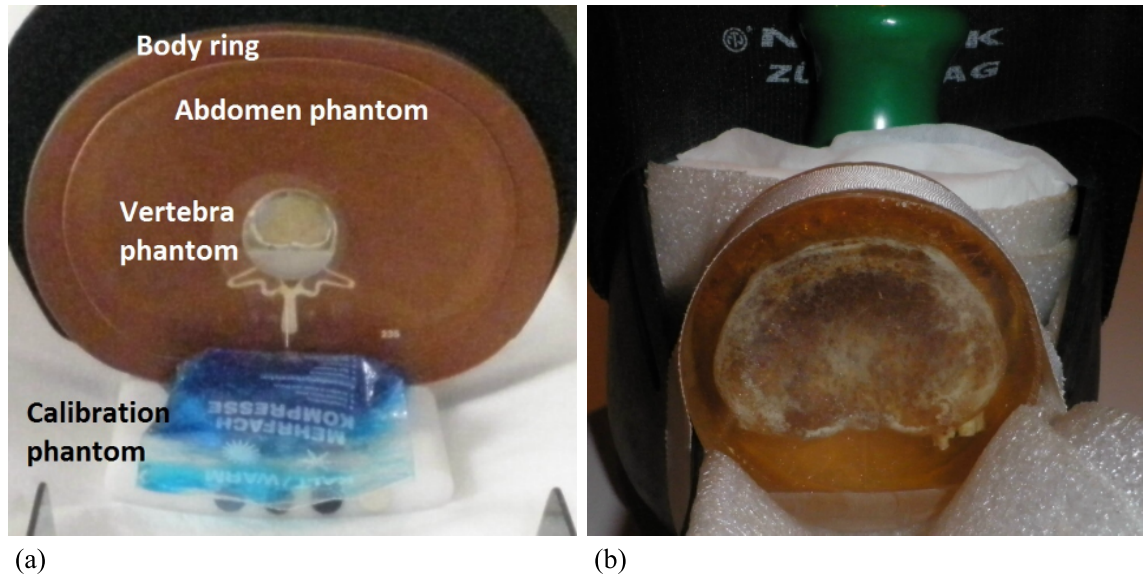


Figure 3.1: a) Simulated in-vivo scan: the vertebra phantom is embedded in the abdomen phantom with body ring (quasi in-situ). The calibration phantom enables to achieve the density values, b) reference ex-situ scan: the vertebra phantom is scanned without abdomen phantom (quasi ex situ).

3.1 CT volumes and statistical methods

The experiments of the CT-method were tested on two data-sets: one to analyze robustness of the proposed methods in terms of precision and accuracy and the second to predict the experimentally derived maximum failure load F_{exp} (experimentally derived force). A third in silico data was used to tune the developed parameters. It allows to vary the noise and knowing the exact ground-truth structure.

3.1.1 The vertebra phantom

The conducted experiment serves to analyze robustness of the proposed methods in terms of precision and accuracy. It allows to analyze the noise of a specific setting and as a function of body size and ray exposure.

Five human T12 vertebral specimens were harvested from deceased donors, surrounding soft tissue and marrow was removed and the vertebrae were then embedded in epoxy resin (Technovit Epox, Heraeus Kulzer GmbH, Hanau, Germany). The vertebrae were obtained from the anatomical institute of the Christian-Albrechts-University at Kiel, Germany and the department of legal medicine of the University

Hospital Hamburg-Eppendorf, Germany. The vertebra phantoms were inserted in an abdomen phantom (Model 235, Computerized Imaging Reference Systems Inc, Norfolk, VA, USA) and repeatedly scanned with different settings in a clinical CT-scanner (Somatom Sensation 64, Siemens AG, Forchheim, Germany), thereby simulating different in-vivo conditions. Two protocols, a high-resolution (355 mAs) and a standard resolution (140 mAs) were applied, both with 120 kVp and voxel size $188 \times 188 \times 300 \mu\text{m}^3$.

Each setting was repeated 3 times with the abdomen phantom and additionally 2 times by using both, the abdomen phantom and the body ring, resulting in four different noise regimes and ten repeated scans per VOI. Taking only the 3 scans without body ring gives insight into the systematic variance induced by noise of the HRQCT or QCT setting. The second setting with additional body ring simulates the in-vivo noise of obese patients, see Fig. 3.1. The 5 scans together enable to measure changes of body size, which applies for long-term studies that last several years. The complete 10 scans can be used to analyze the impact of all variables: change of patient size and change of noise characteristics. This is also medical reality since long term studies are often performed on different scanners, with different noise characteristics, since the hospitals regularly replace old scanners with new models.

All scans contained a nominal anisotropic voxel resolution of $188 \times 188 \times 300 \mu\text{m}^3$. It is worth to note, that the effective resolution is much lower at a level of $500 \times 500 \times 500 \mu\text{m}^3$, depending on the protocol, thus spongy bone could not be resolved until 1 voxel on these typical HRQCT in-vivo scans. A CT calibration phantom (Model 3, Mindways Software, Austin, Texas, USA) was included to derive mineral values in mg K_2HPO_4 scale. Four equally sized disjoint spongy VOIs (volume ≈ 1.1 to $1.7 \text{cm}^3 = 1.02$ to 1.64×10^5 voxels) were manually placed in one scan of each vertebra and automatically registered to the nine remaining scans. This sample size allows to derive statistical significant precision estimates [40].

Two reference ground-truth scans were performed, one on the clinical CT scanner and one on a HRpQCT scanner. Both were performed with increased ray exposure and without abdomen phantom. The clinical CT scan was performed on the same scanner and with the same calibration technique as the other QCT scans, but with 140kV and 360mAs and with voxel size $137 \times 137 \times 300 \mu\text{m}^3$. This scan shows the maximum obtainable information with the CT scanner, thus with very low noise but still with the absence of a certain part of high frequency information due too

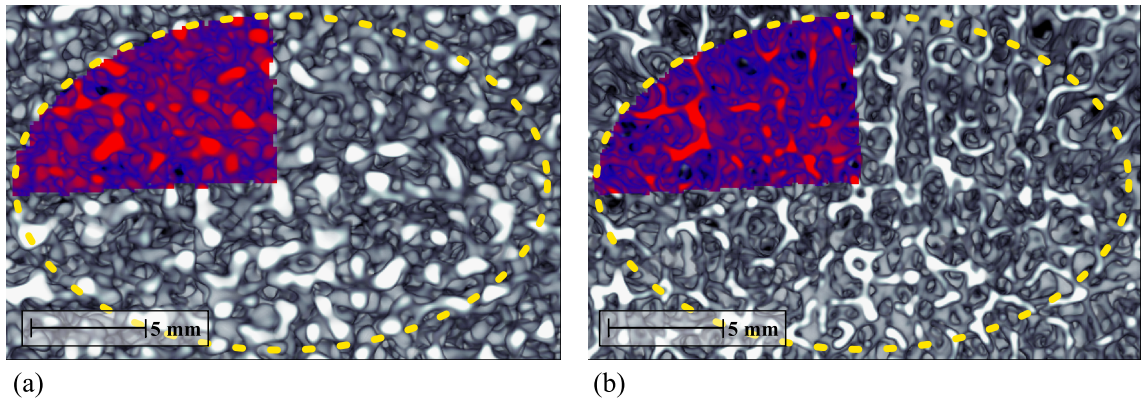


Figure 3.2: Ray casting volume rendering of (a) HRQCT scan (120 kV, 355 mAs) with one of the four VOIs, and (b) HRpQCT scan of the same specimen.

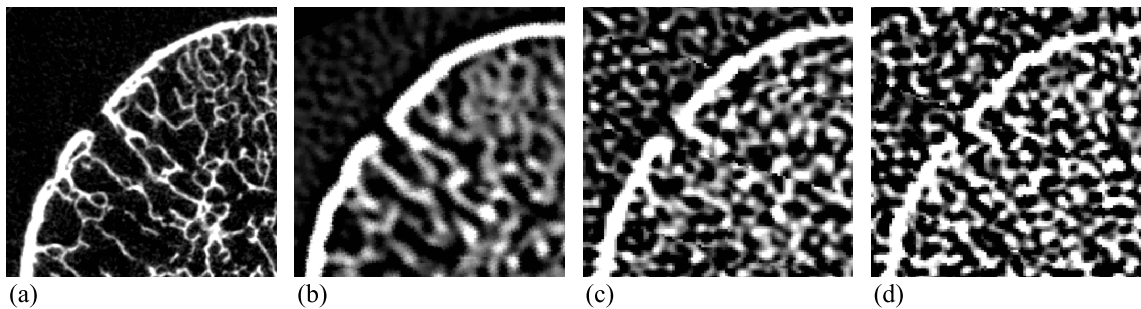


Figure 3.3: Calibrated and registered scans of a sample specimen (sample 5c): a) Ground truth (1), b) Ground truth (2), c) Standard HRQCT, d) Standard QCT.

the voxel resolution. HRpQCT scans of each vertebra phantom were obtained on a XCT scanner (XCT I, Scanco Medical AG, Bassersdorf, Switzerland, voxel size $82 \times 82 \times 82 \mu\text{m}^3$, 59.4kV and 900mAs), but calibrated to a distinct mineral scale [mg CaHA] and with the implemented software of the XCT device, details of which were published elsewhere [130, 102]. The reference scans were automatically registered to obtain the same VOIs of the QCT scans. The registration and calibration of the QCT data was performed with Structural Insight (v3, Biomedical Imaging, University of Kiel, Germany).

The different settings are listed in table 3.1 and the visual differences are depicted in Fig. 3.3.

Name	Mod	Voltage	Exposure	Resolution	A/B	Rep
Ground truth (1)	HRpQCT	59.4kV	900mAs	$82^3 \mu m^3$	-	1
Ground truth (2)	HRQCT	140kV	360mAs	$137^2 \times 300 \mu m^3$	-	1
Standard HRQCT	HRQCT	120kV	355mAs	$188^2 \times 300 \mu m^3$	A	3
Obese HRQCT	HRQCT	120kV	355mAs	$188^2 \times 300 \mu m^3$	A,B	2
Standard QCT	QCT	120kV	140mAs	$188^2 \times 300 \mu m^3$	A	3
Obese QCT	QCT	120kV	140mAs	$188^2 \times 300 \mu m^3$	A,B	2

Table 3.1: Performed scans of each vertebra phantom: name, modality (Mod), voltage, exposure, nominal resolution, with abdomen phantom (A), with body ring (B) and number of repetitions (Rep).

3.1.2 Assessment of precision and accuracy

To measure the performance of structural parameters or pre-processing methods, such as adapted thresholds, the precision and accuracy are computed. The precision of one parameter is obtained as the normalized short-term precision for repeated scans (STP) [40],

$$STP = \sqrt{\frac{\sum_{i=1}^N \sum_{j=1}^M (x_{ij} - \bar{x}_i)^2}{N(M-1)(\max_i\{\tilde{x}_i\} - \min_i\{\tilde{x}_i\})^2}}, \quad (3.1)$$

with $N = 20$ the number of VOIs, $M = 10$ the number of repeated scans per VOI, x_{ij} the structural parameter at VOI i and scan j , \bar{x}_i its arithmetic mean, and \tilde{x}_i the median at VOI i .

The accuracy is obtained in terms of the long-term precision (LTP), which relates the QCT or HRQCT structural parameter (x) with the parameter computed on the ground truth volumes (y). Again, to allow comparison between parameters, this parameter was normalized by the range in ground truth domain,

$$LTP = \sqrt{\frac{\sum_{i=1}^N (y_i - \hat{y}_i)^2}{(N-2)(\max_i\{y_i\} - \min_i\{y_i\})^2}}, \quad (3.2)$$

with $\hat{y}_i = a + b\tilde{x}_i$ the linear estimate of y_i from the QCT.

The statistic STP is identical with the normalized root-mean-square deviation and gives insight into the precision and reproducibility of the technique. The statistic LTP is the normalized root-mean-square error of the fitted data and gives insight into the accuracy and thus to estimate the ground-truth. The original names of

the not normalized parameters[40] are SD and SEE, but they are renamed here to avoid confusion with the standard deviation (SD). The sample size and the number of repeated scans were sufficient to claim statistical significance at a level considered appropriate for characterizing STP and LTP [40].

Statistical significance of the improvement between two techniques (a and b) which compute the same micro-structural entity can be obtained with Fisher's r-to-Z transform. Let x_{ij}^a be the measurement on the QCT or HRQCT data on VOI i and repeated scans j using method a and x_{ij}^b the same measure, but obtained with method b.

- The improvement of the precision between two techniques a and b is obtained from an one factorial ANOVA analysis. The nominal variable of the groups i is related with the parameters x_{ij} . Hence yielding R_a^2 on i vs. x_{ij}^a and R_b^2 on i vs. x_{ij}^b respectively.
- The improvement of the accuracy between x_{ij}^a and x_{ij}^b in relation to a ground truth measure y_i is obtained from linear regression analysis. Hence the ground truth data y_i is expressed as a function of the groups medians \tilde{x}_i . This yields R_a^2 from y_i vs. \tilde{x}_i^a and R_b^2 from y_i vs. \tilde{x}_i^b , respectively.

In both cases of computing either the accuracy or the precision, the inverse one sided p-value that $R_a^2 > R_b^2$ is computed as:

$$p(R_a^2, R_b^2) = 2\Phi \left(-\frac{\operatorname{arctanh}\sqrt{R_a^2} - \operatorname{arctanh}\sqrt{R_b^2}}{\sqrt{2/(N-3)}} \right), \quad (3.3)$$

with N the number of VOIs, which are in this study $5\text{vertebrae} \cdot 4\text{VOIs/vertebra} = 20$, and Φ the cumulative standard normal distribution. R_a^2 is significant higher than R_b^2 if $p < 0.05$.

3.1.3 The Bioasset study

The second experiment was derived out of a larger ex-situ study (BioAsset[41]) performed in total on 33 deceased patients who had osteoporosis. Each spinal specimen contained three vertebrae (T11, T12, L1) and their respective intermediate intervertebral discs. The vertebrae were scanned and calibrated with the same HRQCT

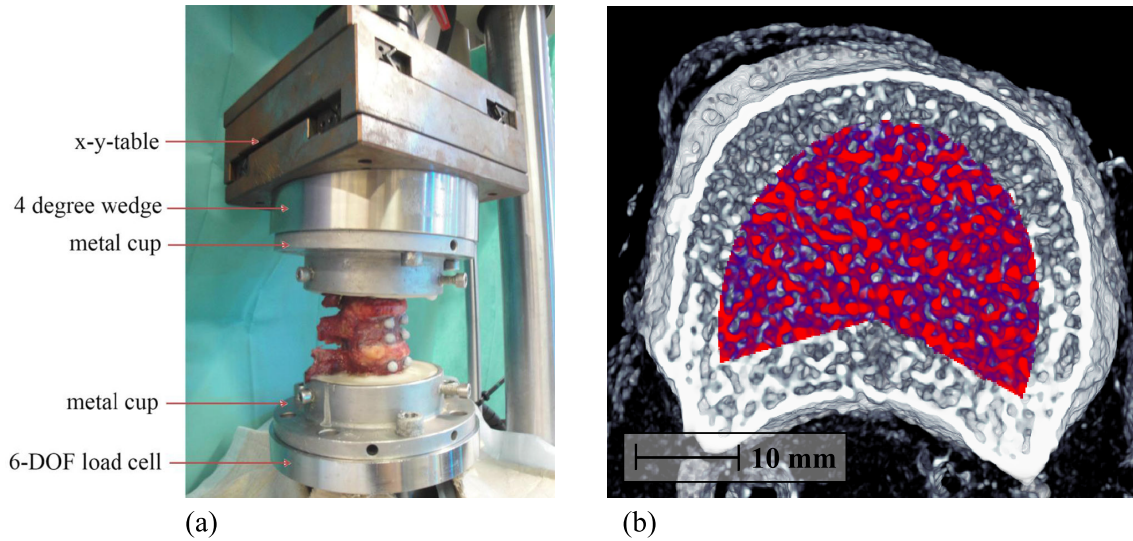


Figure 3.4: (a) Experimental set up to derive the failure load and (b) HRQCT BioAsset scan with Pacman-shaped VOI to compute structural parameters.

procedure as used for the vertebrae phantoms, but segmented with one Pacman-shaped VOI per vertebra. HRQCT data of 76 vertebrae remained after excluding not sufficiently large VOIs. Data of the experimentally derived maximum failure load F_{exp} at T12 were experimentally derived from a subset of 20 patients [81]. The spinal segments were fixed to a servohydraulic testing machine (Bionix 858.2, MTS Systems, Eden Prairie, MN, USA). After preconditioning, a quasistatic uniaxial compression (6 mm/min) with a 4° flexion angle was applied on each spinal segment until resulting failure of the middle vertebral body (T12). Further details of the loading can be found elsewhere [80]. Seventeen T12 vertebrae remained for correlations between F_{exp} and HRQCT parameters after excluding those with an insufficient size. Figure 3.4 shows a sample CT volume and the set up to derive the maximum failure load. Also HRpQCT scans were obtained [41, 81] but not analyzed in this study.

3.1.4 Prediction of failure load

Since BMD has generally the highest correlation with the maximum failure load F_{exp} , the interest regarding this experiment is, which linear combination of additional micro-structural variables improves eventually the correlation with F_{exp} . Thus, the optimum linear models for the prediction of F_{exp} were derived from BMD

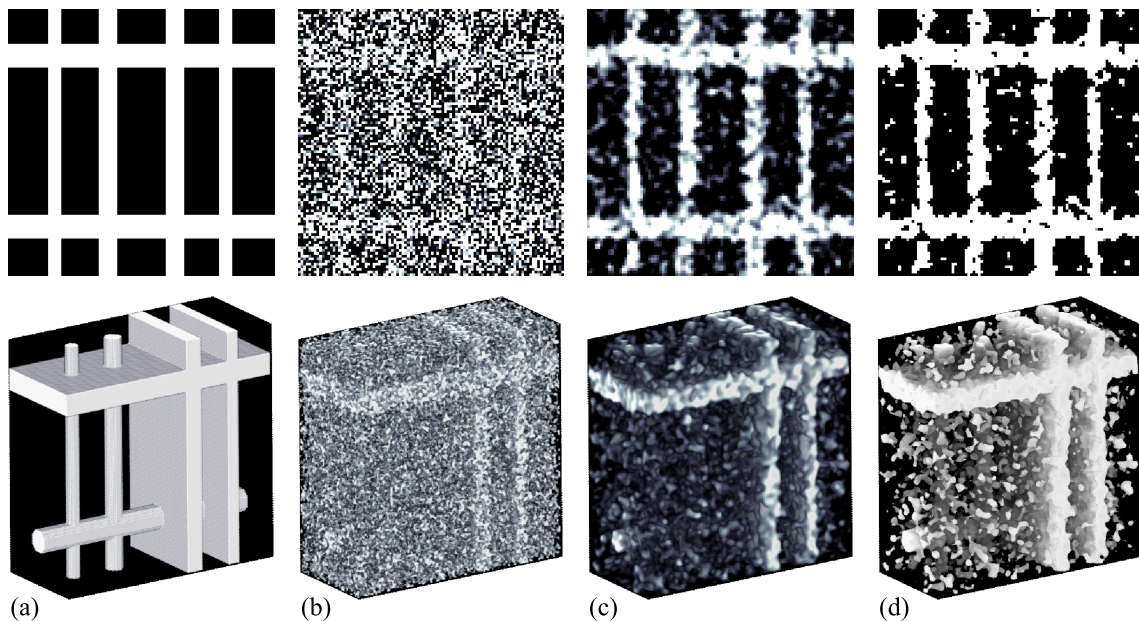


Figure 3.5: Steps for the generating of CT-like noise conditions with $\text{SNR} = 11.7$ (a) Noise-free input volume, (b) sum of input volume and noise, (c) noisy volume after blurring, (d) binary noisy volume.

in combination with up to four structural parameters. The adjusted coefficient of correlation (adj. R^2) and root-mean-square error (RMSE) were computed to assess the quality of the model for a given number of parameters.

The Akaike corrected information criterion (AICc) was applied to compare among models with different numbers of parameters and to select the best model. The AICc is superior to the Bayes information criterion [18] and more widely applied for those analyses [2]. The gain of information between two models can be assessed by the relative likelihood

$$p(m_1, m_2) = \exp\left(\frac{\text{AICc}(m_1) - \text{AICc}(m_2)}{2}\right), \quad (3.4)$$

with m_1 and m_2 the models. An F-test $p(F)$ was used to detect significant different correlations between models.

3.1.5 In silico data

The in silico data is used to investigate the robustness of the local parameters in relation to varying resolution and noise. The test volumes are generated in 3 steps:

(1) The ground truth V is defined by placing rods and plates of defined orientations and thicknesses. The background contains zeros, and the bone material contains ones. (2) Gaussian random noise η with standard deviation σ is added to the volume,

$$V_\eta(\vec{x}) = V(\vec{x}) + \sigma\eta. \quad (3.5)$$

(3) The noisy volume is convolved with the Gaussian,

$$V_{\text{blur}}(\vec{x}) = \text{AVG}_{\mathcal{N}_k^{\text{Gauss}}}(V_\eta; 1; \vec{x}). \quad (3.6)$$

The radius k of that Gaussian defines the resulting spatial resolution. Figure 3.5 shows the three described steps and additionally the noisy binary volume. By varying the parameter σ and k , different noise settings can be produced. The signal-to-noise ratio of the binary volume $H(V(\vec{x}) - t)$ with H the Heaviside function, is computed by

$$\text{SNR}(V, V') = \frac{\sum_{\vec{x}} 1 - |H(V(\vec{x}) - t) - H(V'(\vec{x}) - t)|}{\sum_{\vec{x}} |H(V(\vec{x}) - t) - H(V'(\vec{x}) - t)|}. \quad (3.7)$$

with V the ground-truth and V' a test signal.

3.2 Neighborhood operators

Local operators, which use a local neighborhood are often used for image/volume enhancement to enhance the images or volumes for the computation of the microstructural parameters. The processing with a local neighborhood, defined by a mask, can serve for different specific tasks and can use different techniques, such as convolution or morphology. Isotropic masks are often used for processing 2D images but almost never apply to medical 3D imaging, since the voxel resolution in CT or MRI images is generally anisotropic. Furthermore, classical unweighted and unscaled 3D neighborhood-relationships with for instance 6, 14 or 26 neighbors are a poor choice if image quality is less than optimal and if the relation between voxel-resolution and contained information is anisotropic. Some common preprocessing methods, based on neighborhood operators, are

- **Binarization** of the data into bone and marrow phase serves for the computation of nearly most structural parameters, methods can be based on fixed or Ostu-thresholding but also on the (neighborhood based) Monogenic signal.
- Computation of the **local trabecular thickness** when performed with model independent method. The step, where the distance transformed volume is mapped to the actual thicknesses uses structural elements of varying sizes.
- **Thinning and skeletonization** aims to find the ridges of the bone and to derive structural parameters as the rod volume or plate volume.
- **Resampling** can be used to generate isotropic nominal resolution, which generally allows the application of simpler structural parameters, see [57].
- **Energy minimization** with the Ising model, **median or morphological filtering** serve among others to remove image artifacts and noise.

Further examples of local preprocessing methods, that are not enhancing the data, but mapping the data to other spaces, are

- Tessellation with **marching cubes** allows to compute alternative measures of the bone volume and can be used for the structure model index.
- Assessment of the **local anisotropy** based on the star volume and rose diagrams.
- The **local fractal dimension** aims to access texture parameters and can be adapted to compute the rod- and plate-volume or the trabecular thickness.

3.2.1 Structural elements

The term structural element refers in this thesis to masks with positive entries, defining the membership of the neighboring voxels for the computation of local characteristics. Please note that following this definition, in particular the center voxel is part of its own neighborhood. Examples of isotropic not scalable $3 \times 3 \times 3$ neighborhoods are the one that shares a common side with the center voxel $\mathcal{N}_7^{\text{Vox}}$, the one that considers all neighboring voxel with a common edge $\mathcal{N}_{19}^{\text{Vox}}$, and the one

that activates all neighboring voxels with a common corner $\mathcal{N}_{27}^{\text{Vox}}$,

$$\mathcal{N}_k^{\text{Vox}}(\vec{c}|c_x, c_y, c_z \in \{-1, 0, 1\}) = \begin{cases} 1, & \text{if } |\vec{c}| \leq \sqrt{a_k} \\ 0, & \text{otherwise} \end{cases}, \quad (3.8)$$

with \vec{c} a 3D-offset in voxel coordinates, $|\vec{c}|$ its Euclidean norm, and $a_7 = 1$, $a_{19} = 2$ and $a_{27} = 3$. These fixed structural elements are not scalable and thus have very limited applications.

Scalable structural elements

Some structural elements are proposed, which are used for the computation of the thinning operator and other local characteristics, introduced later. In particular for the computation of the local fractal dimension (Sec. 3.5) the n-dimensional structural element must fulfill the following two requirements:

- The structural element must be positive:

$$\forall \vec{c}: \mathcal{N}(\vec{c}) \geq 0 \quad (3.9)$$

- In n dimensions, the total mass must grow with the n'th power of the radius k .

$$\sum_{\vec{c}} \mathcal{N}_k(\vec{c}) < \sum_{\vec{c}} \mathcal{N}_{k+\delta}(\vec{c}) \rightarrow \frac{\log \sum_{\vec{c}} \mathcal{N}_k(\vec{c}) - \log \sum_{\vec{c}} \mathcal{N}_{k+\delta}(\vec{c})}{\log(k + \delta) - \log(k)} \cong n \quad (3.10)$$

In literature, different structural elements are used, the discrete structural element $\mathcal{N}_k^{\text{metr}}$ reads:

$$\mathcal{N}_k^{\text{metric}}(\vec{c}) = \begin{cases} 1, & \text{if } \|\vec{c}\|_{\text{metric}} < k \\ 0, & \text{otherwise} \end{cases} \quad (3.11)$$

where “metric” denotes the metric and k the radius. The simplest structure element is the box (or cube in 3D) \mathcal{N}_k^∞ , which finds application, though in different form, in the box-counting fractal dimension. This structural element is often used for the computation of the fractal dimension, since it is separable. Though, the main disadvantage of \mathcal{N}_k^∞ is its missing rotational invariance. Spherical or point symmetric structural elements are generally not separable. The discrete version of the spherical structural element uses the Euclidean metric $\mathcal{N}_k^{\text{Euc}}$.

In the case of continuous structural elements, condition Eq. 3.10 can be hardened as

$$\forall \delta > 0 : \frac{\log \sum_{\vec{c}} \mathcal{N}_{k+\delta}(\vec{c}) - \log \sum \mathcal{N}_k(\vec{c})}{\log(k + \delta) - \log(k)} = n, \quad (3.12)$$

thus the growth of the total mass is directly observable for every change in k , which implies in particular $\forall \delta > 0 : \sum \mathcal{N}_{k+\delta} > \sum \mathcal{N}_k$. The continuous version of the spherical structural element $\mathcal{N}_k^{\text{Sphere}}$ models also the point symmetry more precisely than its discrete counterpart:

$$\mathcal{N}_k^{\text{Sphere}}(\vec{c}) = \prod_{i=1}^3 \frac{1}{\epsilon_i} \iiint_0^{\vec{c}} \mathcal{N}_k^{\text{Euc}}(\vec{c} - \vec{c}/2 + \vec{\psi}) d\vec{\psi}. \quad (3.13)$$

where \vec{c} is the voxel spacing or diameter of one voxel.

The Gaussian structural element

The Gaussian structural element $\mathcal{N}_k^{\text{Gauss}}$ contains special properties, it is point symmetric, contains an infinite support and is separable. The Gaussian in 1D reads

$$\widehat{\mathbf{G}}_{\sigma}(x) = \frac{1}{\sqrt{2\pi\sigma^2}} \exp\left(-\frac{x^2}{2\sigma^2}\right). \quad (3.14)$$

and sums to one $\sum_x \mathbf{G}_{\sigma}(x) = 1$. In practice, the support of the Gaussian is restricted. For the purpose of not losing the normalization, the Gaussian needs to be explicitly normalized hence the initial normalization factor loses its importance,

$$\mathbf{G}_{\sigma}(x) = \frac{\widehat{\mathbf{G}}_{\sigma}(x)}{\sum_{y=-\lim}^{\lim} \widehat{\mathbf{G}}_{\sigma}(y)} = \frac{\widehat{\mathbf{G}}_{\sigma}(x)}{|\widehat{\mathbf{G}}_{\sigma}|}. \quad (3.15)$$

The Gaussian in 3D reads

$$\widehat{\mathbf{G}}_{\sigma}^{\text{3D}}(\vec{c}) = \frac{1}{(2\pi\sigma^2)^{(3/2)}} \exp\left(-\frac{|\vec{c}|^2}{2\sigma^2}\right), \quad (3.16)$$

and accordingly the normalized Gaussian in 3D,

$$\mathbf{G}_{\sigma}^{\text{3D}}(\vec{c}) = \frac{\widehat{\mathbf{G}}_{\sigma}^{\text{3D}}(x)}{|\widehat{\mathbf{G}}_{\sigma}^{\text{3D}}|}. \quad (3.17)$$

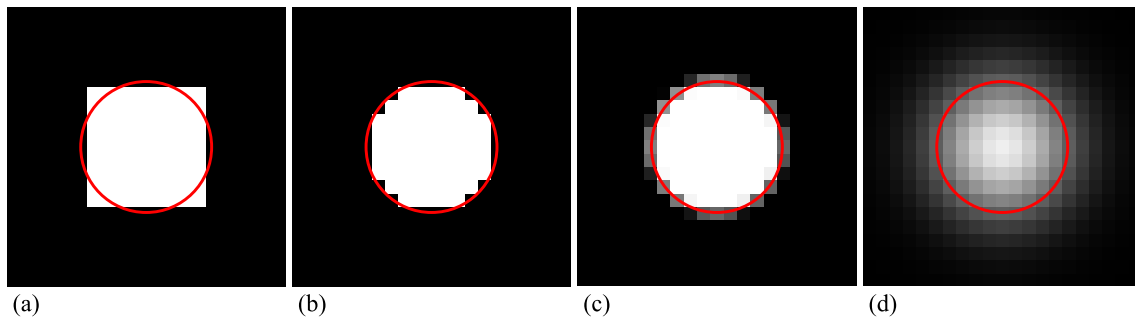


Figure 3.6: Sample structural elements with radius $k = 5$, discrete structural elements a: \mathcal{N}_5^∞ and b: $\mathcal{N}_5^{\text{Euc}}$ and continuous structural elements c: $\mathcal{N}_5^{\text{Sphere}}$ and d: $\mathcal{N}_5^{\text{Gauss}}$. The red circle depicts $\|\vec{c}\|_2 = k$.

The Gaussian structural element uses the normalized Gaussian in 3D but differs, to fulfill Eq. 3.10,

$$\mathcal{N}_k^{\text{Gauss}}(\vec{c}) = \frac{4}{3}\pi k^3 G_{ak}^{3\text{D}}(\vec{c}) \quad (3.18)$$

where k is the radius and a an additional factor,

$$a = \sqrt[3]{\frac{4}{3}\pi k^3 G_k^{3\text{D}}(\vec{0})}. \quad (3.19)$$

The 3D Gaussian is separable,

$$(\mathbf{V} * G_\sigma^{3\text{D}})(\vec{x}) = (((\mathbf{V} * G_\sigma^{1\text{D}x}) * G_\sigma^{1\text{D}y}) * G_\sigma^{1\text{D}z})(\vec{x}) \quad (3.20)$$

with three, except for rotation, identical 1D Gaussian normal distributions. This reduces the complexity of a convolution in 3D from a cubic (n^3) to a linear ($3n$) number of steps, with n the size of the 1D mask. The separability redirects also to the Gaussian structural element,

$$(\mathbf{V} * \mathcal{N}_k^{\text{Gauss}})(\vec{x}) = (\mathbf{V} * \frac{4}{3}\pi k^3 G_{ak}^{3\text{D}})(\vec{x}) = \frac{4}{3}\pi k^3 (\mathbf{V} * G_{ak}^{3\text{D}})(\vec{x}). \quad (3.21)$$

Figure 3.6 shows the 2D projections of the structural elements \mathcal{N}_5^∞ , $\mathcal{N}_5^{\text{Euc}}$, $\mathcal{N}_5^{\text{Sphere}}$ and $\mathcal{N}_5^{\text{Gauss}}$. Neighborhoods with normalized memberships are connoted with an asterisk symbol: $\mathcal{N}^{\text{Euc}*}$, $\mathcal{N}^{\text{Sphere}*}$ or $\mathcal{N}^{\text{Gauss}*}$. These masks are obtained by

$$\mathcal{N}^*(\vec{c}) = \mathcal{N}(\vec{c})/|\mathcal{N}|. \quad (3.22)$$

3.2.2 Local operators

Local texture parameters can be computed for each neighborhood in a similar way as the global parameters 2.4.1 were computed for a general distribution or the entire VOI. The computation of the global parameters was defined for the local signal x_i and a weighting function w_i . In the case of local operators, the structural element acts as a selection operator of the signal $s(\vec{x})$ which is combined with the weighting function $w(\vec{x})$. Hence, the local pendants of Eq. 2.7 and Eq. 2.8 read,

$$W_p(\vec{x}) = (w * (\mathcal{N}_k)^p)(\vec{x}) \text{ and} \quad (3.23)$$

$$S_p(\vec{x}) = ((w \cdot s^p) * \mathcal{N}_k)(\vec{x}). \quad (3.24)$$

Now, the the formulas for the first two weighted cumulants $K_1(\vec{x})$, $K_2(\vec{x})$ are identical to the definition of the global parameters, except for being computed locally for every voxel \vec{x} . The third weighted cumulant reads,

$$K_3(\vec{x}) = \left(\frac{S_3 W_1^2 - 3S_1 S_2 W_1 - 2S_1^3}{W_1^3 - 3W_1 W_2 + 2W_3} \right) (\vec{x}). \quad (3.25)$$

The local nonlinear operators follow the same principle: Let $\vec{\xi}_1 \dots \vec{\xi}_N$ be a labeling of the 3D positions, which induce an ascending sorting of the values of s : $\forall i \in \{1, \dots, N-1\} : s(\vec{\xi}_i) \leq s(\vec{\xi}_{i+1})$. The weighted quantile at a given percentile $Pr \in [0, 1]$ reads now,

$$Q_{Pr}(\vec{x}) = s(\vec{\xi}_j) : \sum_{i=1}^{j-1} \mathcal{N}(\vec{\xi}_i - \vec{x}) w(\vec{\xi}_i) < Pr / W_1(\vec{x}) \leq \sum_{i=1}^j \mathcal{N}(\vec{\xi}_i - \vec{x}) w(\vec{\xi}_i). \quad (3.26)$$

From the definitions above, the same parameters as in the global case can be extracted. However, since the local operators can act like (black-boxed) texture operators, the set of aggregates can be essentially extended:

- the weighted average,

$$\text{AVG}_{\mathcal{N}}(s, w; \vec{x}) = K_1(\vec{x}) \quad (3.27)$$

- the weighted standard deviation,

$$\text{SD}_{\mathcal{N}}(s, w; \vec{x}) = K_2^{(1/2)}(\vec{x}) \quad (3.28)$$

- the weighted coefficient of variation,

$$CV_{\mathcal{N}}(s, w; \vec{x}) = (K_2^{(1/2)} / K_1)(\vec{x}) \quad (3.29)$$

- the weighted standardized skewness,

$$SKW_{\mathcal{N}}(s, w; \vec{x}) = (K_3 / K_2^{(3/2)})(\vec{x}) \quad (3.30)$$

- the weighted median,

$$MED_{\mathcal{N}}(s, w; \vec{x}) = Q_{50\%}(\vec{x}) \quad (3.31)$$

- the robust minimum,

$$MIN_{\mathcal{N}}(s, w; \vec{x}) = Q_{10\%}(\vec{x}) \quad (3.32)$$

- the robust maximum,

$$MAX_{\mathcal{N}}(s, w; \vec{x}) = Q_{90\%}(\vec{x}) \quad (3.33)$$

- the weighted inter-quartile range,

$$IQR_{\mathcal{N}}(s, w; \vec{x}) = (Q_{75\%} - Q_{25\%})(\vec{x}) \quad (3.34)$$

- and the weighted quartile coefficient of variation

$$QCV_{\mathcal{N}}(s, w; \vec{x}) = \left(\frac{Q_{75\%} - Q_{25\%}}{Q_{75\%} + Q_{25\%}} \right) (\vec{x}). \quad (3.35)$$

The local texture variables will be sometimes abbreviated as $AVG_{\mathcal{N}}(\vec{x})$, $SD_{\mathcal{N}}(\vec{x})$ etc., if the choices of s and w are clear from the context. If the structural element is constant and contains an infinite support, the local operators become identical to the global operators introduced in Sec. 2.4.1. An application of the local texture operators will be shown in Sec. 3.6.

Relation to morphology

The local non-linear operators can be interpreted as a gray-value extension of morphological operators, in particular if $w > 0$ is constant for all voxels, the signals $Q_{0\%}$ and $Q_{100\%}$ become the classical erosion and dilation,

$$w \text{ constant} \rightarrow Q_{0\%}(\vec{x}) = (s \ominus \mathcal{N})(\vec{x}), \text{ and} \quad (3.36)$$

$$w \text{ constant} \rightarrow Q_{100\%}(\vec{x}) = (s \oplus \mathcal{N})(\vec{x}). \quad (3.37)$$

The actual weighting of the \mathcal{N} becomes irrelevant for these extreme cases ($Q_{0\%}$ and $Q_{100\%}$). For the purpose of using the actual weights of \mathcal{N} the weighted dilation and erosion required the application of more central percentiles, like for instance 10% and 90%,

$$w \text{ constant} \rightarrow Q_{10\%}(\vec{x}) = (s \ominus^* \mathcal{N})(\vec{x}), \text{ and} \quad (3.38)$$

$$w \text{ constant} \rightarrow Q_{90\%}(\vec{x}) = (s \oplus^* \mathcal{N})(\vec{x}), \quad (3.39)$$

where \ominus^* is the weighted erosion and \oplus^* the weighted dilation.

3.3 Preprocessing

Adequate preprocessing methods can contribute to compute structural parameters in a stable manner. The calibration to from Hounsfield to density values and the definition of the bone map Bone are standard examples for the pre-processing of CT volumes. This section contains further examples, 1) for the computation of the bone ridge and 2) a micro-structural calibration, which might be useful for the analysis of multi-center CT studies, to analyze CT scans of different quality in a common pool.

3.3.1 The ridge map

Many micro-structural parameters require either a skeleton or thinned representation of the bone. The skeleton of a 2D image is well defined and can be obtained with morphological thinning operators or ridge operators, like the median axis transform. In contrast, the skeleton is difficult to obtain in 3D. The main problem in 3D is the decision, if a given structure has to be reduced to a rod-like or to a plate-like

part of the skeleton. For instance, a skeleton representation of the cortex should be reduced to a plate-like skeleton while inside the spongiosa, both structures should appear, rods and plates. In other anatomic structures, for instance the liver or the lung, the skeleton reduces generally to rods only. Different algorithms for obtaining 3D skeletons were proposed [111, 106, 146, 82]. Also the fuzzy distance transform [113] was adapted to either generate a fuzzy skeleton [71] or to improve directly the micro-structural parameters, like the Tb.Th or Tb.Sp [127, 26]. The 3D skeletonization applies not only in CT imaging but is an important method in brain MRI to obtain the skeleton of the white matter.

For many operators, it is not required to obtain a complete skeleton of the structure, but it might be sufficient to thin the initial bone structure. Furthermore, the classical skeletonization algorithms are sensitive to noise and require a connected structure in the initial input volume. Scale space approaches can generally be used to obtain edges and ridges of 2D images with a high amount of robustness against image noise [74].

The proposed method defines the ridge Ridge of the bone from a fuzzy bone map $\text{Bone}_{t,\sigma}$ and a normalized 3D structural element. The ridge map Ridge , basically a thinning of the bone probability map Bone (Eq. 2.19) for voxels that are close to the ridge, is obtained with

$$\text{Ridge}(\vec{x}) = (\text{Bone} * \mathcal{N}_k^{\text{Gauss}^*})^q(\vec{x}), \quad (3.40)$$

with $\mathcal{N}_k^{\text{Gauss}^*}$ a normalized Gaussian structural element with radius k and $*$ the 3D convolution operator, alternatively the normalized weighted Euclidean structural element $\mathcal{N}_k^{\text{Sphere}^*}$ could be used. The radius k is an a-priori approximation of the thickness of the structure in Bone , and $1 < q \approx 3$ is used to steer the sharpness of the thinning procedure. The fixpoint of Eq. 3.40 is reached if the bone map Bone is already one voxel wide, hence in the case $\text{Bone} \equiv \text{Ridge}$ further iterative applications of Eq. 3.40 do not produce further changes of Bone .

3.3.2 The Monogenic signal

The 2D Monogenic signal [34] is a specific scale space method, which was already analyzed in the author's Diploma thesis [128]. The Monogenic signal is an extension of the 1D analytic signal to higher dimensions. The 1D analytic signal splits a

(1D) function locally into phase and amplitude, representing the qualitative and quantitative information. The Monogenic signal computes additionally to the phase ϕ and amplitude a also the main gradient of the image flux ∇ . The original concept is based on Laplacian filters, originally defined as a set of difference of Poissons filters (DoP) which aim as bandpass filters and to derive directional information. While the Poisson filter is optimal for the purpose of computing the Monogenic signal, it has the disadvantage of not being separable. Fortunately, the Poisson filter can be approximated with a Gaussian [34], which owns the missing property of being separable (see Sec. 3.2.1). For the computation of the 3D Monogenic signal, four bandpass filters as difference of Gaussians (DoG) are derived, with $\sigma_f < \sigma_c$ the fine and coarse scales:

$$K_{xyz}(\vec{c}) = (\mathbf{G}_{\sigma_f}^{3D} - \mathbf{G}_{\sigma_c}^{3D})(\vec{c}), \quad (3.41)$$

$$K_x(\vec{c}) = \left(\frac{\vec{e}_x \cdot \vec{c}}{\sigma_f} \mathbf{G}_{\sigma_f}^{3D} - \frac{\vec{e}_x \cdot \vec{c}}{\sigma_c} \mathbf{G}_{\sigma_c}^{3D} \right) (\vec{c}), \quad (3.42)$$

$$K_y(\vec{c}) = \left(\frac{\vec{e}_y \cdot \vec{c}}{\sigma_f} \mathbf{G}_{\sigma_f}^{3D} - \frac{\vec{e}_y \cdot \vec{c}}{\sigma_c} \mathbf{G}_{\sigma_c}^{3D} \right) (\vec{c}), \quad (3.43)$$

$$K_z(\vec{c}) = \left(\frac{\vec{e}_z \cdot \vec{c}}{\sigma_f} \mathbf{G}_{\sigma_f}^{3D} - \frac{\vec{e}_z \cdot \vec{c}}{\sigma_c} \mathbf{G}_{\sigma_c}^{3D} \right) (\vec{c}) \quad (3.44)$$

with \vec{e}_x , \vec{e}_y and \vec{e}_z the unit vectors in x-, y- and z- direction and \cdot the point-wise multiplication. Four convolutions of the 3D input signal V are obtained,

$$\nabla_u(\vec{x}) = (V * K_u)(\vec{x}) \quad (3.45)$$

with u a placeholder of xyz , x , y or z . Then, the following signals are extracted.

- The modulus of the gradient,

$$|\nabla|(\vec{x}) = \sqrt{\nabla_x^2 + \nabla_y^2 + \nabla_z^2}(\vec{x}). \quad (3.46)$$

- The local amplitude:

$$A(\vec{x}) = \sqrt{\nabla_{xyz}^2 + \nabla_x^2 + \nabla_y^2 + \nabla_z^2}(\vec{x}). \quad (3.47)$$

- The local phase:

$$\phi(\vec{x}) = \arctan\left(\frac{|\nabla|}{\nabla_{xyz}}\right)(\vec{x}). \quad (3.48)$$

- The normalized gradient or local main orientation:

$$\Theta(\vec{x}) = \left(\frac{\langle \nabla_x, \nabla_y, \nabla_z \rangle}{|\nabla|}\right)(\vec{x}). \quad (3.49)$$

The signal ∇_{xyz} is also called the reconstruction of A and ϕ , since

$$\nabla_{xyz}(\vec{x}) = A(\vec{x}) \cos(\phi(\vec{x})). \quad (3.50)$$

Figure 3.7 shows the application of the monogenic signal on a vertebra for different scales. For the implementation with a finite support, the masks must be normalized to match the following constraints:

- The sum of the Gaussians must be normalized to one (see Eq. 3.17).
- The support must be defined to fix the energy of the larger Gaussian, for instance with $p = 95\%$:

$$p = |\mathbf{G}_{\sigma_c}^{3D}| = \sum_{\vec{c}} \mathbf{G}_{\sigma_c}^{3D}(\vec{c}). \quad (3.51)$$

- The energy of the bandpass kernel K_{xyz} must be aligned to the one of the gradient kernels:

$$K_{xyz}^*(\vec{c}) = \left(\sqrt{\frac{\sum_{\vec{d}} (K_{\nabla_x}^2 + K_{\nabla_y}^2 + K_{\nabla_z}^2)(\vec{d})}{\sum_{\vec{d}} K_{xyz}^2(\vec{d})}}\right) K_{xyz}(\vec{c}). \quad (3.52)$$

The advantage of replacing the Poisson mask, as defined originally, with the Gaussian mask is the separability, which redirects to the Monogenic signal.

The Monogenic signal in scale space

An image or volume contains generally local information of different scales. The optimum local scale can be detected by computing the Monogenic signal for a constant

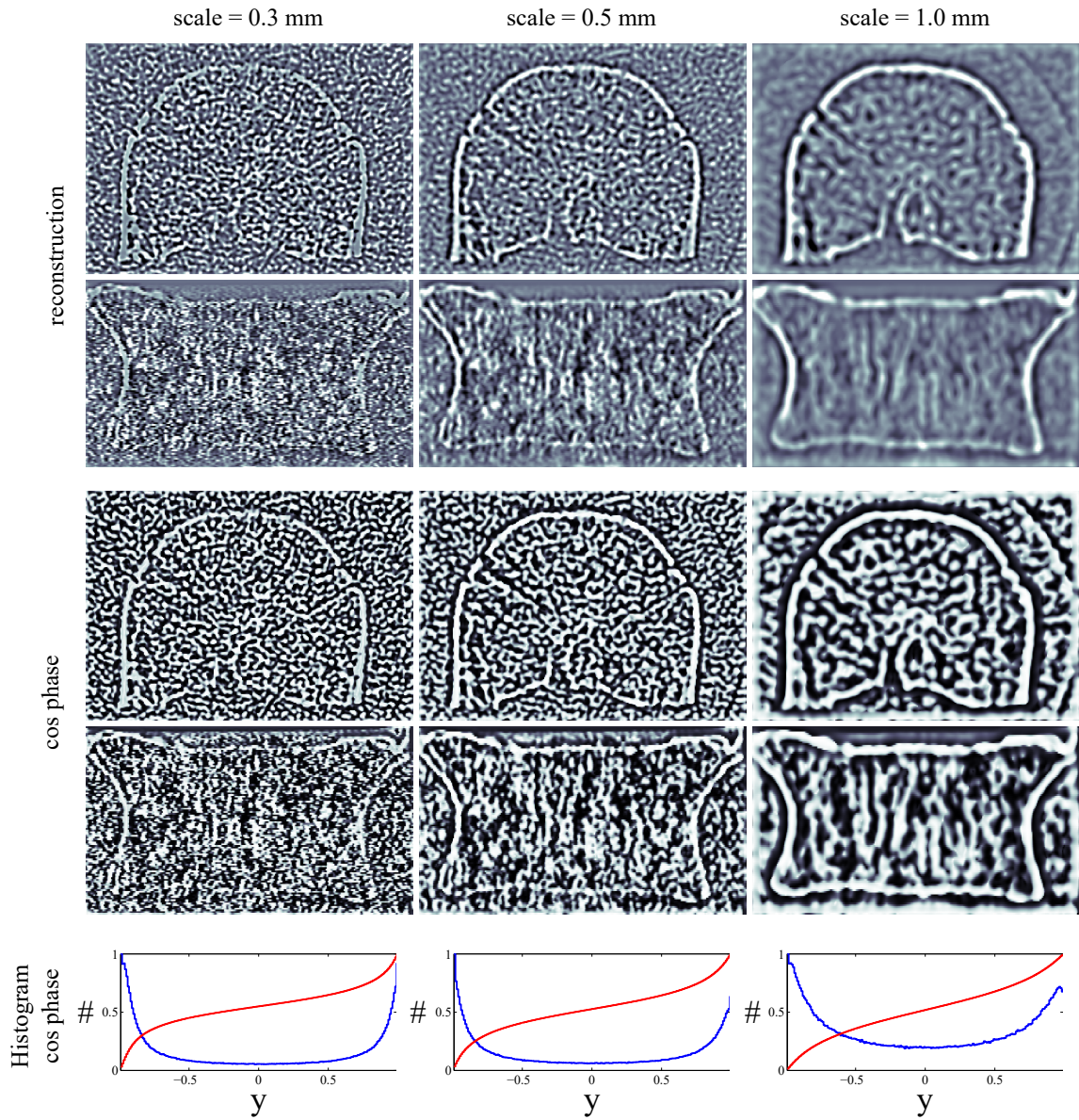


Figure 3.7: Monogenic signal. Reconstruction and phase for different scales (0.3, 0.5 and 1.0 mm).

bandwidth w and different scales:

$$s_i = \exp \left(\log(s_0) + i \frac{\log(s_{N-1}) - \log(s_0)}{N-1} \right). \quad (3.53)$$

The parameters of the bandpass filters read

$$\sigma_{f_i} = s_i/w \text{ and} \quad (3.54)$$

$$\sigma_{c_i} = s_i w. \quad (3.55)$$

Accordingly, one obtains for every scale s_i all signals ϕ_i , A_i , Θ_i and $|\nabla|_i$. The classical approach for selecting the optimum scale is based on the maximum modulus of the gradient,

$$s_{|\nabla|}(\vec{x}) = \arg \max_i \{ |\nabla|_i(\vec{x}) \}. \quad (3.56)$$

Alternatively, the optimum scale can be selected as the one that produces locally the smoothest amplitude,

$$S_{CV}(\vec{x}) = \arg \min_i \{ CV_{\mathcal{N}}(A_i, \mathbf{1}; \vec{x}) \}. \quad (3.57)$$

The local weighted CV is described in Eq. 3.29. Both approaches yield different results, $\cos(\phi_{s_{|\nabla|}})$ reveals a higher amount of details while $\cos(\phi_{S_{CV}})$ is superior in terms of connectivity.

Detection of ridges and edges

The application of the Monogenic signal to CT volumes reveals (1) the qualitative information if a voxel is part of bone and (2) the quantitative information of the ridgeness of the bone. The signal $\phi \in [0, \pi]$ contains the qualitative information

- the voxel belongs to a bone ridge, if $\cos(\phi) = 1$,
- the voxel belongs to an intersection between bone and marrow if $\sin(\phi) = 1$.
- the voxel belongs to a bone basin, if $\cos(\phi) = -1$ and

Thus, a probability function of being a ridge P_r , a basin P_b or intersection P_{br} can be established as:

$$P_r(\vec{x}) = \max\{0, \cos(\phi(\vec{x}))\}^\alpha, \quad (3.58)$$

$$P_b(\vec{x}) = \max\{0, -\cos(\phi(\vec{x}))\}^\alpha, \quad (3.59)$$

$$P_{rb}(\vec{x}) = \sin(\phi(\vec{x}))^\alpha \quad (3.60)$$

with $\alpha \in (0, \infty)$ a parameter of the sharpness. The probabilities P_r , P_b and P_{rb} are purely qualitative, which means they are unweighted according to the local bone density and detect therefore false positive voxels outside the vertebra. The weighting according to the local bone density can be obtained by involving the blurred version of Bone which is the signal Ridge obtained with a Gaussian structural element and $q = 1$, Eq. 3.40. The value k in that equation serves as a blurring range, for instance $k = 0.4\text{mm}$. The final Monogenic ridge map reads

$$\text{Ridge}^{MS}(\vec{x}) = (P_r \cdot \text{Ridge})(\vec{x}). \quad (3.61)$$

Figure 3.8 shows a sample case of Ridge^{MS} . Similar to Ridge^{MS} the maps of the intersections and the basins can be defined via

$$\text{Basin}^{MS}(\vec{x}) = (P_b (1 - \text{Ridge}))(\vec{x}), \quad (3.62)$$

$$\text{Intersection}^{MS}(\vec{x}) = (P_{rb} (1 - |1 - 2 \text{Ridge}|))(\vec{x}). \quad (3.63)$$

Microstructural parameters

The Monogenic signal can be used to obtain a segmentation of the bone phase, which suppresses noise. This might improve the computation of standard structural parameters. Furthermore, the Monogenic signal allows the direct extraction of structural parameters. When interpreting the signal Ridge^{MS} as a measure of the local BV/TV, the monogenic bone volume ratio (BV/TV) is defined as

$$\text{BV/TV}^{MS} = \text{AVG}(\text{Ridge}^{MS}). \quad (3.64)$$

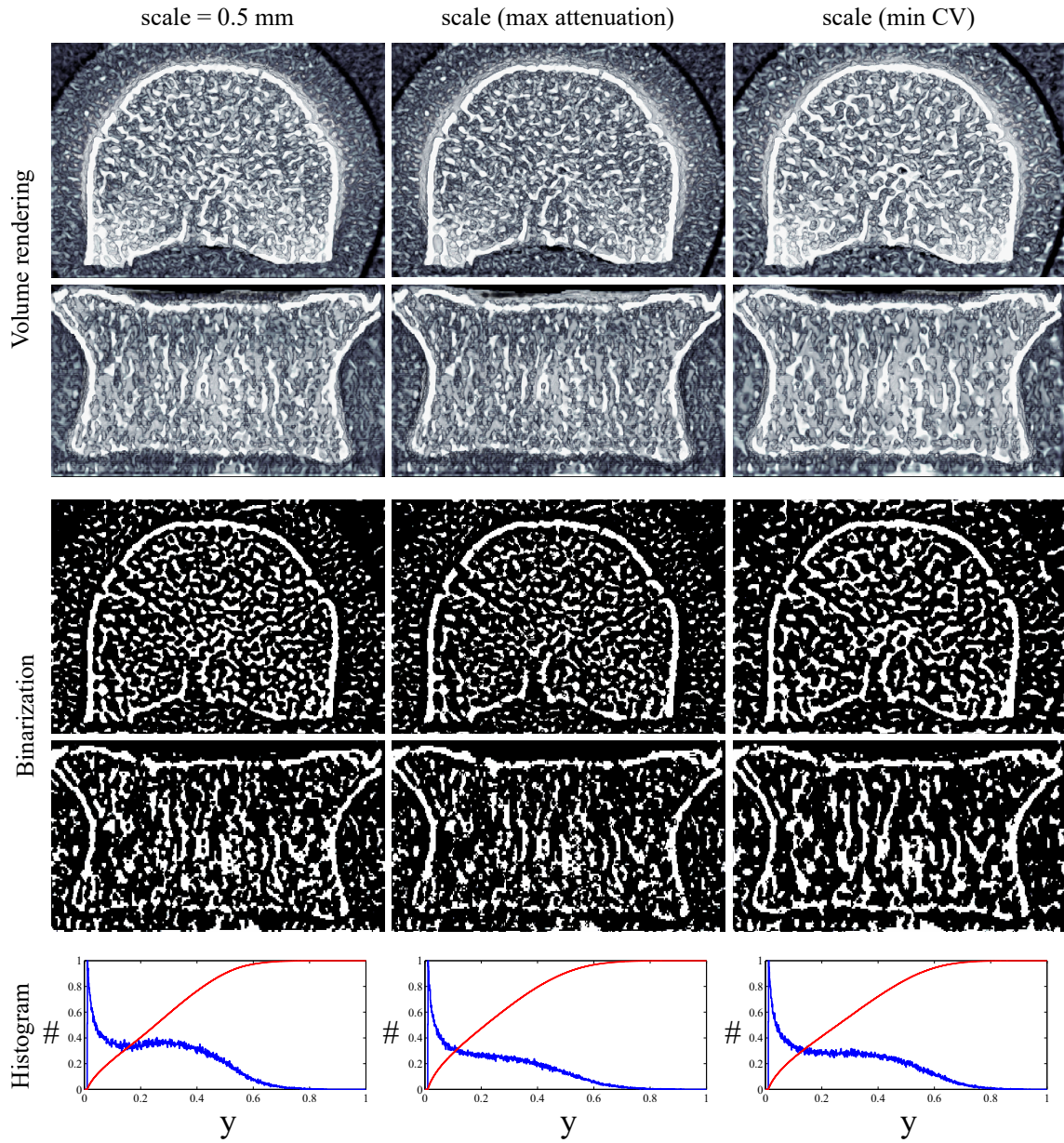


Figure 3.8: Monogenic signal. The Monogenic ridge Ridge^{MS} based on scale 0.5mm, $s_{|\nabla|}$ and s_{CV} .

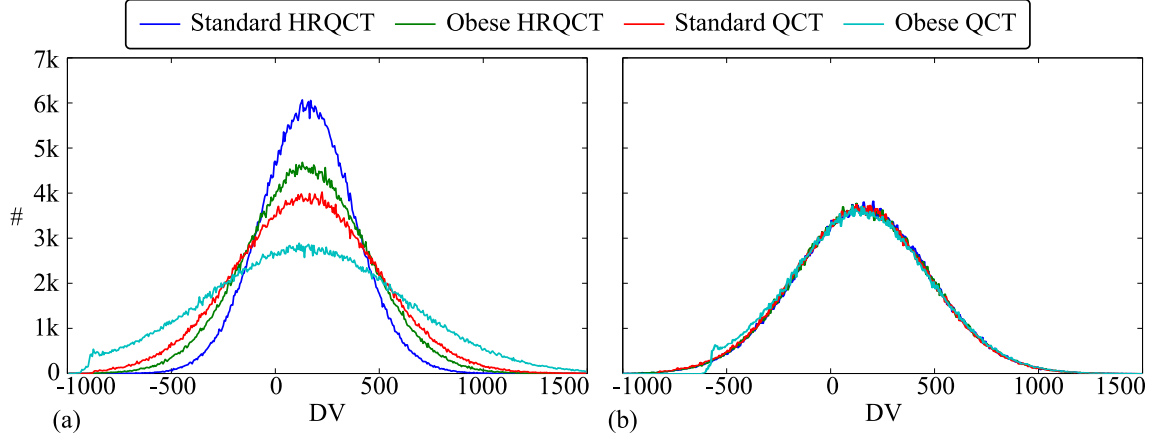


Figure 3.9: Histogram of the same specimen but under different settings V^{DV} : a) histograms (from tight to wide) are 355mAs without body ring, 355mAs with body ring, 140mAs without body ring and 140mAs with body ring, b) histograms after correction with the histogram-based global method V^{Global} .

Additionally, $Ridge^{MS}$ can be interpreted as a fuzzy segmentation, which yields the monogenic tissue mineral density (TMD):

$$TMD^{MS} = \text{AVG}(V^{DV}, \text{Ridge}^{MS}). \quad (3.65)$$

Finally, the detected scales $s_{|\nabla|}$ or s_{CV} can be interpreted as a structural parameter, which might be related with the Tb.Th, with s_* either $s_{|\nabla|}$ or s_{CV} :

$$\text{Tb.Th}^{MS} = \text{AVG}(s_*, \text{Ridge}^{MS}). \quad (3.66)$$

3.3.3 Micro-structural calibration

The calibration of density values enables the computation of BMD and micro-structural parameters. In studies, which contain differences in the noise spectrum, the standard calibration (Eq. 2.2) is generally not sufficient for an accurate obtainment of micro-structural parameters. Differences of the noise spectrum manifest in the histogram of the density values, where a high signal-to-noise ratio produces a high standard deviation of the distribution (Fig. 3.9). A global histogram based and a local technique to normalize the volumes and to compensate the image noise are presented. The resulting histograms of the global (V^{Global}) and local micro-structural calibration V^{Local} are nearly identical.

Global micro-structural calibration

Let, according to Eq. 2.2, be $V_{i,j}^{\text{DV}}(\vec{x})$ the density at voxel \vec{x} of the i 'th calibrated volume of group j . Furthermore, BMD_{ij} is the BMD and $\text{SD}_{ij} = \text{SD}(V_{ij}^{\text{DV}})$ the standard deviation of V_{ij} . The mean standard deviation of group j reads:

$$\overline{\text{SD}}_j = \text{AVG}(\text{SD}_{1j}, \dots, \text{SD}_{Nj}). \quad (3.67)$$

The global normalization V^{Global} applies a linear scaling of the histogram, such that the standard deviation of the resulting histogram becomes constant SD_* for all scans but without changing the BMD,

$$V_{ij}^{\text{Global}}(\vec{x}) = \frac{\text{SD}_* (V_{ij}^{\text{DV}}(\vec{x}) - \text{BMD}_{ij})}{\overline{\text{SD}}_j} + \text{BMD}_{ij}. \quad (3.68)$$

Here, any choice of $\text{SD}_* > 0$ is valid, however the targeted standard deviation might be fixed as the global average SD, see Fig. 3.9,

$$\text{SD}_* = \overline{\text{SD}} = \frac{1}{NM} \sum_{i=1}^N \sum_{j=1}^M \text{SD}_{ij}. \quad (3.69)$$

This normalization has the advantage that a certain fixed threshold for the group study reflects now a fixed BV/TV rather than a fixed density value. The disadvantage of this method is the distortion of apparent density values, in particular on the tails of the histogram.

Local micro-structural calibration

The local calibration removes the bias of the density on the tails of the histogram and while still decreasing the local noise (or contrast). The calibrated volume is decomposed into the low-frequency (low-pass) and high-frequency (high-pass) information,

$$\text{Lowpass}_{ij}(\vec{x}) = (V_{ij}^{\text{DV}} * \mathcal{N}_k^{\text{Gauss}^*})(\vec{x}) \quad (3.70)$$

$$\text{Highpass}_{ij}(\vec{x}) = (V_{ij}^{\text{DV}} - \text{Lowpass}_{ij})(\vec{x}) \quad (3.71)$$

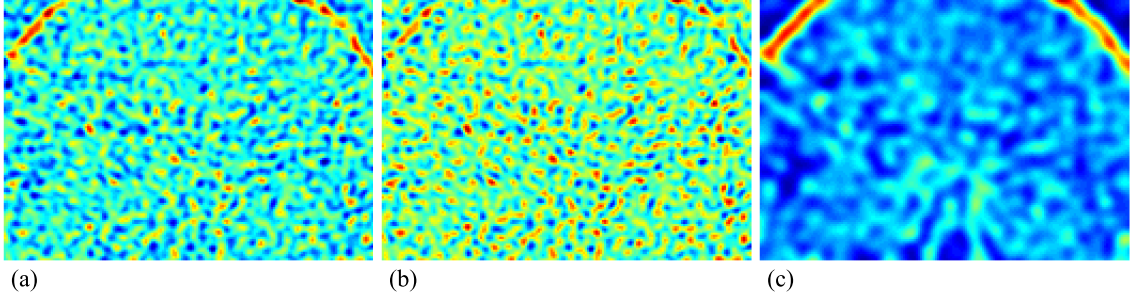


Figure 3.10: Split of the volume for the local micro-structural calibration with scale $s = 0.5\text{mm}$ and image resolution $\langle 0.18\text{mm} \times 0.18\text{mm} \times 0.3\text{mm} \rangle$. (a) input volume V^{DV} , (b) High pass signal Highpass which is rescaled for the micro-structural calibration, (c) low-pass signal or local BMD Lowpass.

The low-pass contains the local average density and the high-pass both, the noise but also the specific structural information. The kernel size k must be big enough to remove the local structural information but small enough to contain the differences of the local BMD. The filtering is applied to the high-pass signal, before the volume is again reconstructed. The standard deviation of the i 'th high-passed volume of group j reads $SD_{ij}^{Local} = SD(Highpass_{ij})$, and the mean standard deviation of the high passed volumes of group j is

$$\overline{SD_j^{Local}} = \text{AVG}(SD_{1j}^{Local}, \dots, SD_{Nj}^{Local}). \quad (3.72)$$

With the signal SD_*^{Local} which is the target standard deviation after filtering the high-passed signal, the local micro-structural calibration reads,

$$V_{ij}^{Local}(\vec{x}) = \frac{SD_*^{Local} \text{Highpass}_{ij}(\vec{x})}{\overline{SD_j^{Local}}} + \text{Lowpass}_{ijV}(\vec{x}). \quad (3.73)$$

Any choice of $SD_*^{Local} > 0$ is valid, in particular the mean of the the entire group study (as in Eq.3.69),

$$SD_*^{Local} = \overline{SD^{Local}} = \frac{1}{NM} \sum_{i=1}^N \sum_{j=1}^M SD_{ij}^{Local}. \quad (3.74)$$

The global method is a special case of the local method. By setting $k = \infty$ both become identical, the low-pass becomes unable to capture any local information and

thus reduces to the BMD,

$$\text{Lowpass} = (V^{\text{DV}} * \mathcal{N}_{\infty}^{\text{Gauss}^*})(\vec{x}) = \text{BMD}, \quad (3.75)$$

accordingly $\overline{\text{SD}}^{\text{Local}}$ becomes $\overline{\text{SD}}$.

It is worth to note that neither of both calibration techniques improve the image quality but both serve only for an enhancement regarding the comparison of structural parameters in inhomogeneous group studies. While the global method rescales the gray values of the entire image, the local approach rescales only the high frequency information, where the noise is located.

Statistical Analysis

For the statistical analysis, the data of the vertebra phantoms was analyzed. Direct measures from voxel counting were bone mineral density (BMD), bone volume fraction (BV/TV) and tissue mineral density (TMD). The mean intercept length (MIL) was computed with the direct secant method, yielding trabecular number (Tb.N), bone surface fraction (BS/BV), trabecular thickness (Tb.Th*) and trabecular separation (Tb.Sp*) from the parallel plate model. Model independent measures were trabecular separation (Tb.Sp), trabecular thickness (Tb.Th) and the structure model index (SMI). All parameters were computed for each of the three calibration techniques: 1) the standard calibration of the density values V^{DV} , 2) the global micro-structural calibration V^{Global} and 3) the local micro-structural calibration V^{Local} . The threshold was chosen at $t = 400 \text{ mg/cm}^3$ which served to obtain an average $\text{BV/TV} \approx 25\%$.

Results

Figure 3.11 shows the structural parameter for a sample case (Tb.Th*). A systematic bias was observed when not performing the micro-structural calibration. The absolute values of Tb.Th* increased with increasing noise level. The global micro-structural calibration was able to increase the precision, but still the values of Tb.Th* were ordered by the noise level, however inverted. The local micro-structural calibration increased additionally the precision and removed simultaneously most of the remaining noise-bias.

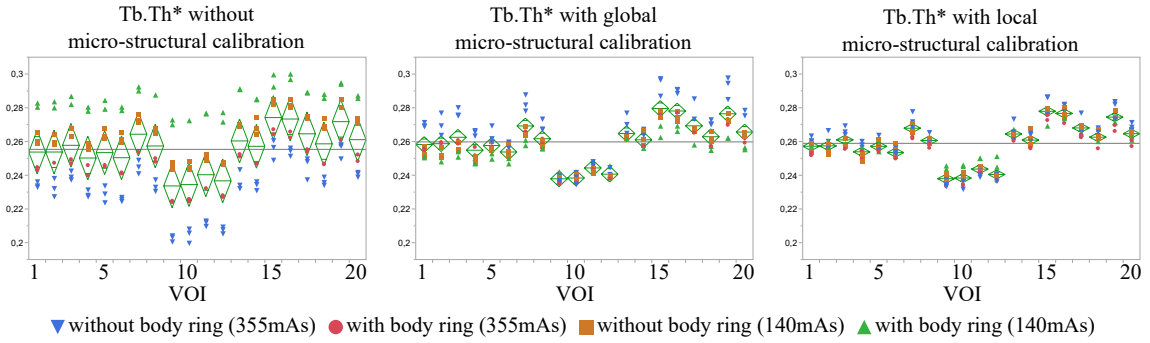


Figure 3.11: Computed values of $Tb.Th^*$ for all 10 repeated scans and all 20 VOIs. Left: application of density calibration only (V^{DV}), middle: global micro-structural calibration (V^{Global}), right: local micro-structural calibration (V^{Local}).

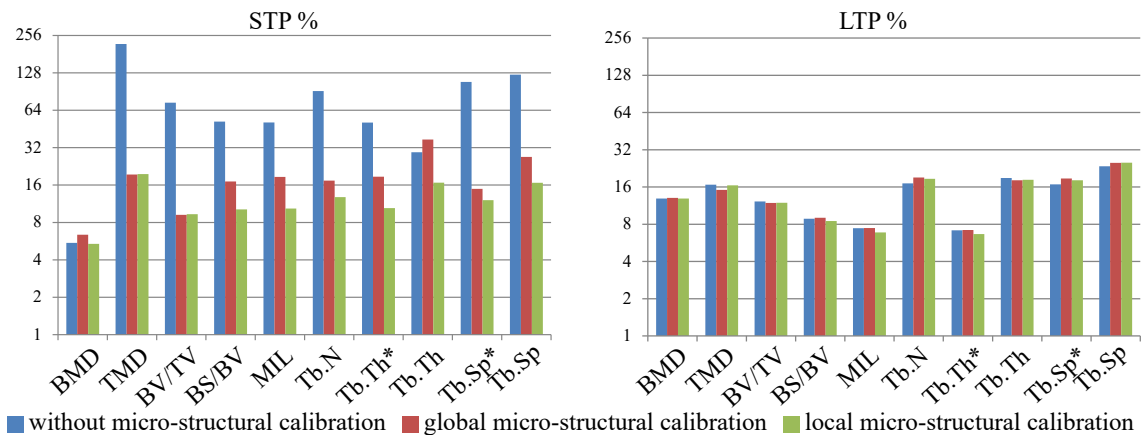


Figure 3.12: Results of the short-term (left) and long-term precision (right) on a logarithmic scale. Blue bar: application of density calibration only (V^{DV}), red bar: global micro-structural calibration (V^{Global}), green bar: local micro-structural calibration (V^{Local}).

Accuracy and precision

Figure 3.12 shows the short-term and long-term precision of all computed structural parameters. The reproducibility (STP) in a group study was improved for all micro-structural parameters (except for BMD) using either the global V^{Global} or the local micro-structural calibration V^{Local} . The largest gain of reproducibility was achieved with V^{Local} , which was in some cases (BMD, TMD, BV/TV) mostly equal to V^{Global} . The STP of the parameters of V^{Local} in relation to the data without micro-structural calibration V^{DV} ranged from 57% for Tb.Th down to 13% for BV/TV, 11% for Tb.Sp* and 9% for TMD. V^{Local} improved 8 from 10 parameters

significantly $p < 0.01$. Only BMD ($p = 0.97$) and Tb.Th ($p = 0.13$) did not improve with statistical significance. In the case of V^{Global} four parameters improved with high statistical significance ($p < 0.01$): TMD, BV/TV, Tb.N and Tb.Sp* and three with simple significance: BS/BV ($p = 0.02$), MIL ($p = 0.03$) and Tb.Th* ($p = 0.03$). Tb.Sp ($p = 0.07$) did not improve significantly and the R^2 of BMD and Tb.Th even declined under V^{Global} . Significant improvements of the long-term precision with micro-structural calibration were not observed. Here the ratio between V^{Local} and V^{DV} ranged from 93% for Tb.Th* up to 109% for Tb.N.

Discussion and conclusion

The experimental work performed in this section focused on the analysis of two important aspects: the precision or reproducibility of the computed micro-structural parameters, expressed as STP and the accuracy or trueness of the parameters, expressed as LTP. The results showed that the standard density calibration was poorly adjusted to heterogeneous group studies, if the threshold remained fixed. If the threshold was adapted to a fixed BV/TV, as assessed with the global micro-structural calibration V^{Global} , all structural parameters improved, with exception of Tb.Th. The linear map of V^{Global} decreases the performance of BMD since this operation distorts the density values. However, the precision of TMD was not affected by this distortion, because the TMD is computed on the statistically corrected right part of the histogram. In contrast, a simple adaption of the threshold for each group to fit a constant BV/TV, but applied on V^{DV} would result in wrong values of the TMD.

The local micro-structural calibration V^{Local} reduces the noise directly without biasing the density values. Hence, the BMD but as well the TMD were correctly computed. However, the performance regarding the TMD and BV/TV was not different to the one with V^{Global} . The reproducibility of the micro-structural parameters improved remarkably, not only towards V^{DV} but as well towards V^{Global} .

Regarding the second statistic (LTP), no obvious differences were observed between either of the three calibration techniques. This means that the structural information which is computed from the QCT scans is not decreased by the proposed methods. For studies that are performed on one homogenous setting, the application of the micro-structural calibration has no negative effect. This is an important finding, since an homogenous setting of a complete in-vivo study is nearly

impossible to obtain. Not only changes of exposure, voltage or the model of the scanner or calibration phantom bias the calibrated volume V^{DV} , but also the patient's location inside the x-ray tube or the patient's size, which might easily change between different patient's visits.

The local micro-structural calibration, as proposed here, were to the author's knowledge so far not proposed for the application of QCT group-studies. A global micro-structural calibration[56], which is, with exception of BMD and TMD, for all structural parameters identical to an adaption of the threshold, was already proposed. Also the problem of threshold selection [48] is a known problem for many structural parameters. In some cases, a correction of the scanner settings is performed post-hoc [42]. Here, a linear fit in the parameter space is applied, transforming for instance the parameter Tb.Sp into an adjusted Tb.Sp. This adjustment is problematic, because it assumes a linearity of the structural parameter with the noise level. Also the absolute scale gets lost, hence an adjusted structural parameter does not serve anymore for quantitative conclusions.

Three calibration methods for the computation of micro-structural parameters on inhomogeneous CT group studies were compared. A simulated inhomogeneous group study consisting of 5 patients, containing each 4 VOIs with in total 10 repeated scans per patient and 2 HRQCT and 2 QCT settings was simulated. Ground-truth data were obtained from reference HRpQCT scans. In particular the novel micro-structural calibration method V^{Local} was able to improve the reproducibility of all considered micro-structural parameters without harming the accuracy. The absence of any bias regarding the ground-truth suggests that any post-hoc adjustment of micro-structural parameters might become obsolete if performing the proposed a-priori correction of the input volumes.

3.4 Soft classification of the plate-rod model with three dimensional rose diagrams

This section presents a local soft classifier of the rod-plate-model and the anisotropy of spongy 3D volumes and is an extension of a method presented at Escuela y Workshop Argentino en Ciencias de las Imágenes, Buenos Aires, 2014 [129]. The operator is intended to operate correctly at junctions and mixed regions between rods and plates. In contrast to other operators, neither skeletonization nor binarization are

required. Moreover the operator presented here works directly on the rose diagram without applying a principal component analysis. The comparison of this approach with standard methods suggests the ability of superior performance on noisy images with low resolution. Although further improvements are still required for real-world CT data, the method might likely be suitable to analyze clinical in-vivo computed tomography scans.

3.4.1 Introduction

The estimation of the plate-rod model is important for many image processing tasks of the analysis of volumetric and spongy volumes, for instance on computed tomographic volumes of the vertebra. The ratio between plates and rods serves as a input of the model dependent trabecular separation and distance of the discrete secant method [122]. Also the finite element analysis for the estimation of the bone-strength could be boosted by including the individual rod-plate model and the directional information. Finally the distribution of orientations of the rods and plates and the rod-plate-ratio can be used as a primary structure parameter for monitoring changes or disorders of the skeletal architecture.

The local acquisition of the rod-plate model at bone images is generally affected by low resolution and the low signal-to-noise ratio, which reduces the accuracy of the parameter estimation. General approaches are based on the local principal components and perform weak at junctions and at non-ridge locations. Figure 3.13 demonstrates that issue. A description with principal components relates only the 3 principal axes to each other $\lambda_1 \geq \lambda_2 \geq \lambda_3$, hence rods are given by $\lambda_1 \gg \lambda_2 \approx \lambda_3$, plates are $\lambda_1 \approx \lambda_2 \gg \lambda_3$ and isotropic neighborhoods are given by $\lambda_1 \approx \lambda_2 \approx \lambda_3$. This methodology contains fails in the case of junctions, detecting a rod-rod junction as a plate, and a rod-plate or plate-plate junction as an isotropic region.

The estimation of the rod-plate model with the SMI and the 3D fragmentation index [123] is only defined for binary structures and does not contain any noise treatment. Further approaches were developed that belong either to the class of eigenvalue- or non-texture-methods (see [91] and references therein) and local estimators of fabric anisotropy and fabric elongation are based on eigenvalues (compare [10] and [63]).

The here proposed method derives the anisotropy and the rod-plate model without applying a principal component analysis, binarization or skeletonization. In-

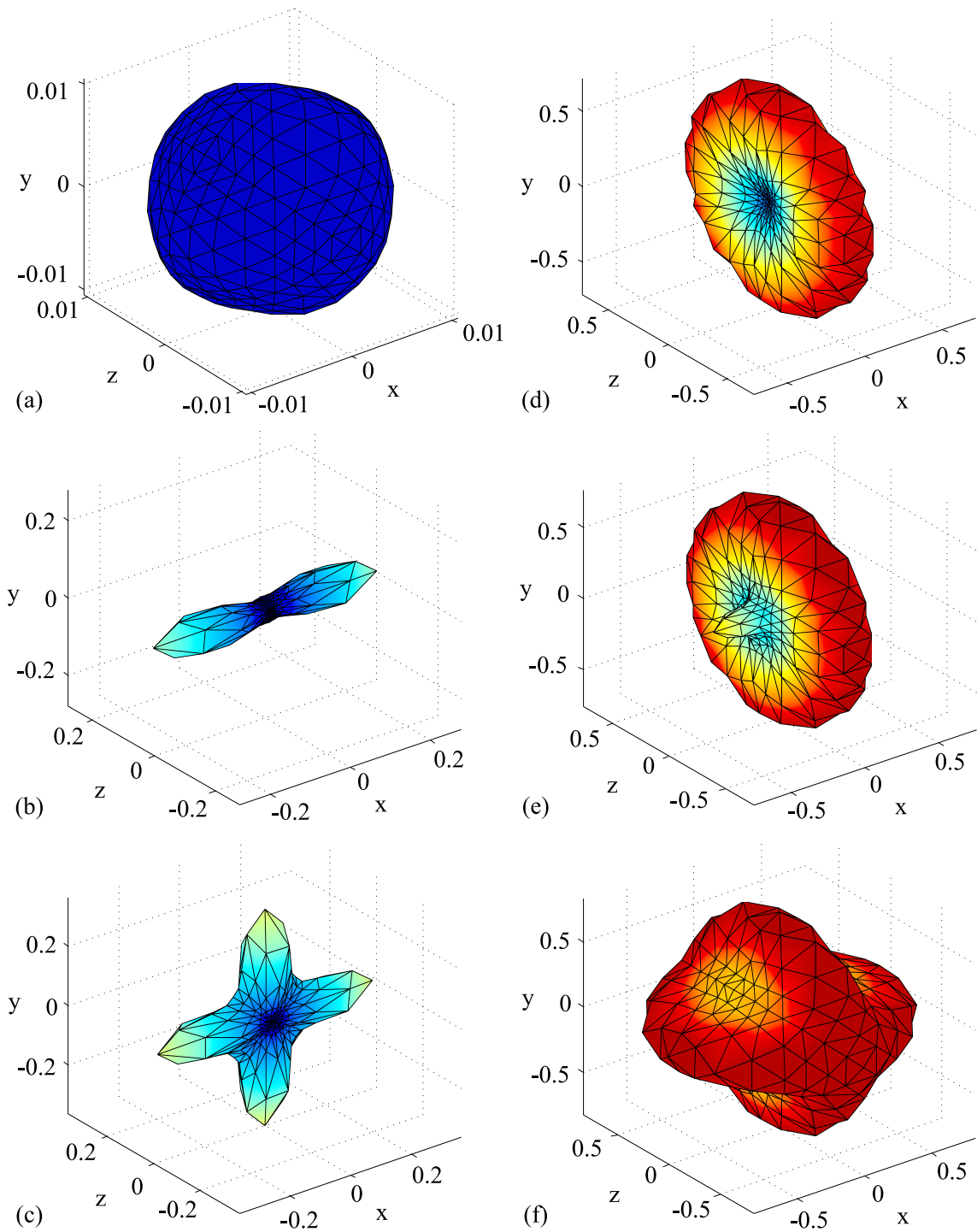


Figure 3.13: Sample rose diagrams based on the inverse standard deviation, weighted by the bone mass a) void, b) rod c) junction of rods d) plate e) junction of rod and plate f) junction of plates.

stead, it analyzes directly the 3D rose diagram of local 1D texture parameters. The features are robust against noise by convolving the local 1D texture inside a neighborhood, following a principle developed by Andrea Silveti [121].

3.4.2 Directional standard deviation

The proposed method transforms the 3D volume V into N new volumes of identical size $VSD_{\theta_1}, \dots, VSD_{\theta_N}$. Each of these new volumes contains the local standard deviation in direction θ . The uniform distribution of orientations $\Theta = \theta_1, \dots, \theta_N$ in 3D, the 3D rose diagram, is supplied by an algorithm which recursively sub-divides an octahedron [63], defining for each 3D orientation θ_i a line grid. Every voxel \vec{x} is the center of a line segment with orientation θ_i and length L . Now, the standard deviation is computed for all line segments, thereby the line segments of all centers and orientations are resampled with the 3D spline method to reach the same length in voxels. Each line segment contains the values

$$\langle V(\vec{x} - L \theta), \dots, V(\vec{x} + L \theta) \rangle. \quad (3.76)$$

The volume that contains the directed standard deviations reads

$$\widehat{VSD}_\theta(\vec{x}) = SD(\langle V(\vec{x} - L \theta), \dots, V(\vec{x} + L \theta) \rangle, \langle w_{-L}, \dots, w_L \rangle), \quad (3.77)$$

where the unweighted standard deviation reads $\forall i : w_i = 1$ and the weighted one uses the 1D Gaussian: $\forall i : w_i = G_L(i)$. It is important to compute the standard deviation directly on the volume data, without applying any smoothing or noise reduction, which would reduce the computed standard deviation. However, a smoothing might be applied after computing the standard deviation, thus following the idea of the 3D local operators with view-range r :

$$VSD_\theta(\vec{x}) = \text{AVG}_{\mathcal{N}_r^{\text{Gauss}}}(\widehat{VSD}_\theta, \widetilde{W}; \vec{x}), \quad (3.78)$$

where \widetilde{W} is a weighting map of same size as V , for instance defined as $\widetilde{W}(\vec{x}) = \text{Ridge}(\vec{x})$. The average operator might alternatively be replaced with the median operator,

$$VSD_\theta(\vec{x}) = \text{MED}_{\mathcal{N}_r^{\text{Gauss}}}(\widehat{VSD}_\theta, \widetilde{W}; \vec{x}), \quad (3.79)$$

obtaining generally a smoothing of higher robustness. For simplicity, both weighting functions W (Eq. 3.77) and \widetilde{W} (Eq. 3.78) are disabled in the conducted tests, hence contain everywhere ones. The abbreviation $VSD(\vec{x})$ refers to the complete 4D data set of standard deviations at \vec{x} in all N directions $\theta_1, \dots, \theta_N$. Increasing the parameters L and r increases the robustness against noise but decrease the spatial resolution, hence they need to be adapted for every specific image class and according to the specific problem.

The signal $VSD_\theta(\vec{x})$ is inverted against common rose diagrams based on mass distributions (Fig 3.13), the principal orientation of the intrinsic structure is given by the minimum standard deviation. The values of $VSD(\vec{x})$ at a void but noisy region is distributed around the noise level η . A region with a rod in orientation θ contains η at θ and higher values at the other orientations. The same counts for a region containing a plate with normal θ . At compound structures, e.g. two perpendicular rods in orientation θ_X and θ_Y , the minimum of $VSD(\vec{x})$ is strictly above the noise level: $VSD_{\theta_X}(\vec{x}) \approx VSD_{\theta_Y}(\vec{x}) > \eta$, this is the case at the junction of the two rods in the test image.

Anisotropy and junction index

An anisotropy index $A^* \in \mathbb{R}^{\geq 0}$ is derived as the median standard deviation,

$$A^*(\vec{x}) = \text{MED}(\{VSD_{\theta_1}(\vec{x}), \dots, VSD_{\theta_N}(\vec{x})\}). \quad (3.80)$$

This signal is mapped to the interval $[0, 1)$ with the cumulative gamma distribution Γ_{CDF} . Let $g_{k,m}(x)$ be the generic function

$$g_{(k,m)}(x) = 2 \max\{0, \Gamma_{CDF}(x; k, \frac{m}{k} \frac{3k + 0.2}{3k - 0.8}) - 0.5\}, \quad (3.81)$$

with k a shape parameter and m the optimum approximation of the median of Γ_{CDF} (see [5]), and $\forall x < m : g_{(k,m)}(x) = 0$. The anisotropy index $A \in [0, 1)$ reads now

$$A(\vec{v}) = g_{(0.5,\eta)}(A^*(\vec{v})) \quad (3.82)$$

with η the noise level as introduced before.

The rose diagram $VSD(\vec{x})$ contains its minimum at orientations, which contribute either to rods or plates. A distinction between rods and plates is derived by

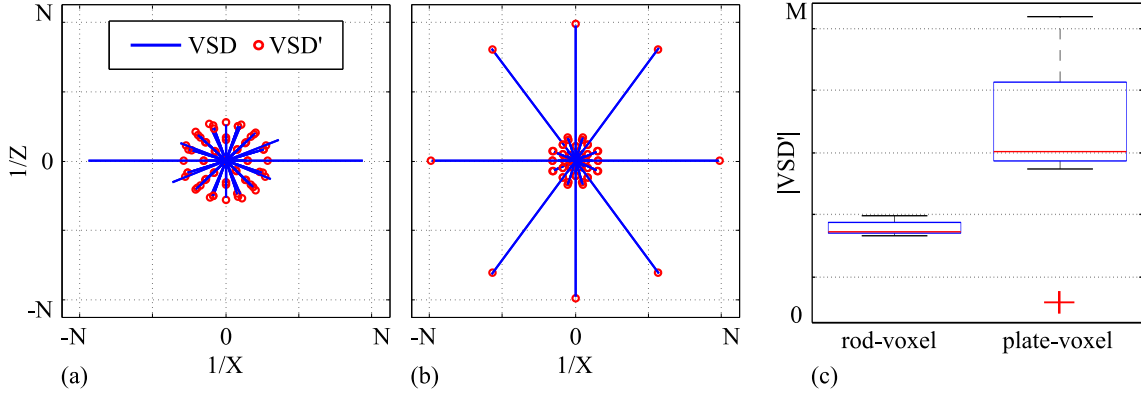


Figure 3.14: a) X-Z-projection of $VSD(\vec{x})$ and $VSD'(\vec{x})$ of a rod in x-orientation and b) of a plate with normal in y-orientation, c) box plot showing the distribution of $VSD'(\vec{x})$ at the rod- and plate- voxel. The ratio between minimum and maximum of the plotted data defines $p_{\text{Rod}}(\vec{x})$.

transforming $VSD(\vec{x})$ to the dual rose diagram VSD^\perp , that contains the median of the orthogonal directions of VSD:

$$VSD_\vartheta^\perp(\vec{x}) = \text{MED}(\{VSD_{\theta_1}(\vec{x}), \dots, VSD_{\theta_M}(\vec{x})\} | \theta_i \perp \vartheta) \quad (3.83)$$

This dual rose diagram is again remapped to the initial directions by using now the minimum operator,

$$VSD'_\theta(\vec{x}) = \min(\{VSD_{\vartheta_1}^\perp(\vec{x}), \dots, VSD_{\vartheta_L}^\perp(\vec{x})\} | \vartheta_i \perp \theta) \quad (3.84)$$

The set $\{VSD_{\vartheta_1}^\perp, \dots, VSD_{\vartheta_L}^\perp\}$ is related to the plate-Hough transform of VSD_θ , and VSD'_θ is the feature extraction from that Hough-space. A local voxel \vec{x} contains a plate, if the following requirement is fulfilled,

$$\begin{aligned} \vec{x} \text{ contains plate} &\Leftrightarrow \exists \phi : VSD_\phi(\vec{x}) = \min\{VSD_{\theta_1}(\vec{x}), \dots, VSD_{\theta_N}(\vec{x})\} \\ &\wedge VSD'_\phi(\vec{x}) = \min\{VSD'_{\theta_1}(\vec{x}), \dots, VSD'_{\theta_N}(\vec{x})\}. \end{aligned} \quad (3.85)$$

Similarly reads the condition that \vec{x} contains a rod in direction ϕ ,

$$\begin{aligned} \vec{x} \text{ contains rod in } \phi &\Leftrightarrow VSD_\phi(\vec{x}) = \min\{VSD_{\theta_1}(\vec{x}), \dots, VSD_{\theta_N}(\vec{x})\} \\ &\wedge VSD'_\phi(\vec{x}) > \min\{VSD'_{\theta_1}(\vec{x}), \dots, VSD'_{\theta_N}(\vec{x})\}. \end{aligned} \quad (3.86)$$

Figure 3.14 illustrates this relation.

Plate and Rod-likeness

The plate-likeness $\text{Plate}(\vec{x}) \in [0, 1)$ and rod-likeness $\text{Rod}(\vec{x}) \in [0, 1)$ are defined as:

$$p_{\text{Rod}}(\vec{x}) = \frac{\min\{\text{VSD}'_{\theta_1}(\vec{x}), \dots, \text{VSD}'_{\theta_N}(\vec{x})\}}{\max\{\text{VSD}'_{\theta_1}(\vec{x}), \dots, \text{VSD}'_{\theta_N}(\vec{x})\}} \quad (3.87)$$

$$\text{Rod}(\vec{x}) = g_{(4,2\eta)}(p_{\text{Rod}}(\vec{x})A^*(\vec{x})) \quad (3.88)$$

$$\text{Plate}(\vec{x}) = g_{(1,2\eta)}((1 - p_{\text{Rod}}(\vec{x}))A^*(\vec{x})), \quad (3.89)$$

with $p_{\text{Rod}}(\vec{x})$ the probability that an existing anisotropy is not induced by a plate, $g_{(k,M)}(x)$ serves to normalize the signal to $[0, 1)$ and η is the noise level as used before, Fig. 3.15.

The global rod volume fraction can be defined with the weighted average and the ridge map $\text{Ridge}(\vec{x})$ as defined in Sec. 3.3.1 and Sec. 3.3.2,

$$\text{RV}/\text{BV}^{\text{Rose}} = \frac{\sum_{\vec{x}} \text{Rod}(\vec{x})\text{Ridge}(\vec{x})}{\sum_{\vec{x}} \text{Ridge}(\vec{x})}. \quad (3.90)$$

Similarly the plate volume fraction reads,

$$\text{PV}/\text{BV}^{\text{Rose}} = \frac{\sum_{\vec{x}} \text{Plate}(\vec{x})\text{Ridge}(\vec{x})}{\sum_{\vec{x}} \text{Ridge}(\vec{x})}. \quad (3.91)$$

Additionally the anisotropic rod volume fraction reads

$$\text{RV}/(\text{RV}+\text{PV})^{\text{Rose}} = \frac{\sum_{\vec{x}} \text{Rod}(\vec{x})\text{Ridge}(\vec{x})}{\sum_{\vec{x}} (\text{Rod}(\vec{x}) + \text{Plate}(\vec{x}))\text{Ridge}(\vec{x})}, \quad (3.92)$$

and the anisotropic plate volume fraction is

$$\text{PV}/(\text{RV}+\text{PV})^{\text{Rose}} = \frac{\sum_{\vec{x}} \text{Plate}(\vec{x})\text{Ridge}(\vec{x})}{\sum_{\vec{x}} (\text{Rod}(\vec{x}) + \text{Plate}(\vec{x}))\text{Ridge}(\vec{x})}. \quad (3.93)$$

3.4.3 Preliminary results and discussion

Figure 3.15 shows the application of the plate- and rod classifier $C(\lambda_1, \lambda_2, \lambda_3)$ taken from [138], which is based on the three principal components. Methods based on principal components fail in general at junctions since they are unable to distinguish

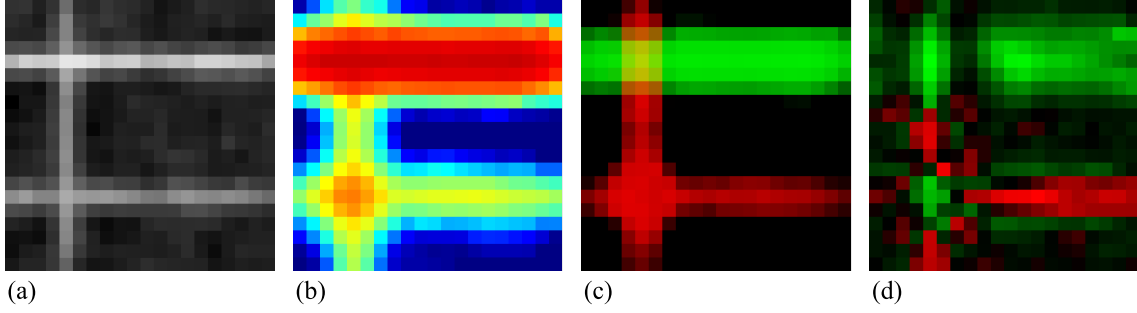


Figure 3.15: a) Noisy test volume: the slice cuts two rods (left and bottom) and one plate (top) in its center, b) anisotropy index $A(\vec{x})$ c) rod- and plate-likeness: red channel Rod(\vec{x}), green channel Plate(\vec{x}). d) C from [138] based on the three eigenvalues of a principal component analysis. This parameter performs inaccurate at junctions.

between perpendicular junctions of rods and plates and neither between intrinsic 3D (or 0D) regions and junctions of a plate with a perpendicular rod. Another problem is the impact of noise and the detection of rods and plates at locations that are not located on the ridge of the structure. On the contrary, the here presented method is robust at these spots. The operator is adaptable to different texture parameters, thus not only to the standard deviation but for instance as well to the inter-quartile range. Furthermore a combination with a signal that uses the average or median of the directed line segments could be beneficial, hence replacing the standard deviation in Eq. 3.77 with the average or median operator. This can be used to extend the definitions given in Eqs. 3.86 and 3.85. It is worth to note, that the minimum- and maximum- operator might be replaced in practice with a weighted minimum and maximum-operator, meaning a weighted 5% or 95% quantile and the orthogonality-operator $\theta \perp \vartheta$ must be replaced with a weighting according to the angle between θ and ϑ , similar to the procedure applied in Eq. 2.5. Finally the standard deviation can be computed with directional weighting masks and the formula of the weighted operators, Sec. 3.2.2, thus avoiding resampling issues. The proposed method can be adjusted to particular volume types by varying size of the integration length L , used for the definition of $\widehat{\text{VSD}}_{\theta}(\vec{x})$, the smoothing range r used for the definition of $\text{VSD}_{\theta}(\vec{x})$, or the shape parameter k , used for defining $g_{(k,M)}(x)$.

3.5 The rod volume fraction and the trabecular thickness with the local fractal dimension

Parts of this section have been published in *Medical Physics* [132] and a preliminary fractal method has been published in 2013 at the Argentine Symposium on Technology [130]. The method aims to demonstrate the application of the fractal dimension and it deals together with the method of Sec. 3.4 with the detection of the local anisotropy and the distinguishing between plate- and rod-like structures.

Existing microstructure parameters are able to predict vertebral in-vitro failure load, but for noisy in-vivo data more complex algorithms are needed for a robust assessment. A new algorithm is proposed for the microstructural analysis of trabecular bone under in-vivo quantitative computed tomography (QCT). Five fractal parameters are computed: (1) the average local fractal dimension FD, (2) its standard deviation FD.SD, (3) the fractal rod volume ratio fRV/BV, (4) the average fractal trabecular thickness fTb.Th, and (5) its coefficient of variation fTb.Th.CV. The algorithm requires neither an explicit skeletonization of the trabecular bone, nor a well-defined transition between bone and marrow phases. Two experiments were conducted to compare the fractal with established microstructural parameters. In the first, 20 volumes-of-interest of embedded vertebrae phantoms were scanned five times under QCT and high-resolution (HR-)QCT and once under peripheral HRQCT (HRpQCT), to derive accuracy and precision. In the second experiment, correlations between in vitro HRQCT structural parameters were obtained from 76 human T11, T12, or L1 vertebrae. In vitro fracture data were available for a subset of 17 human T12 vertebrae so that linear regression models between failure load and microstructural HRQCT parameters could be analyzed. The results showed correlations of fTb.Th and fRV/BV with their nonfractal pendants trabecular thickness (Tb.Th) and respective structure model index (SMI) while higher precision and accuracy was observed on the fractal measures. Linear models of bone mineral density with two and three fractal microstructural HRQCT parameters explained 86% and 90% (adjusted R^2) of the failure load and significantly improved the linear models based only on BMD and established standard microstructural parameters (68% – 77% adjusted R^2). The application of fractal methods may grant further insight into the study of bone quality in-vivo when image resolution and quality are less than optimal for current standard methods.

3.5.1 Introduction

Quantitative computed tomography (QCT) is a clinical in-vivo 3D image modality that allows visualization and quantitative assessment of the spongy microstructure of human vertebrae. In particular, QCT can be used for diagnosis and monitoring of osteoporosis. Bone quality encompasses bone mineral density (BMD), micro architecture, turnover rates, damage accumulation, and mineralization [28]. While the extraction of BMD from QCT or even dual energy absorptiometry (DXA) is straightforward, the estimation of microstructure parameters is more challenging. BMD is able to account for up to 70% of variability of the vertebral failure load, while existing microstructure parameters yield little additional information. Nevertheless, high computational power enables the application of more complex algorithms which are needed for a robust assessment of microstructure parameters under noisy in-vivo QCT.

Several refined algorithms have been proposed for dependent [49] and independent trabecular separation models [127, 26, 71]. Algorithms of the rod volume ratio (RV/BV) include scale space methods [114], fuzzy approaches [89], concurrent assignments of rod- and plate-likeness on the same voxel [91], and methods to obtain simultaneously RV/BV and trabecular thickness (Tb.Th) [138]. However, most of these attempts require a well-defined transition between bone and marrow phases or a structure preserving 3D skeletonization [112]. This makes them more likely suited for HRpQCT, rather than HRQCT or QCT resolution realms. In 3D imaging, fractal methods contain similar properties as scale space methods. Due to the limited computational power, early implementations of fractal concepts focused primarily on global parameters, for instance, box-counting dimensions [36]. Nowadays, different kinds of local fractal dimensions exist [121] and have been obtained from an initial slope in loglog scale between a local measure and the radii of the local neighborhood. In particular the trabecular bone score [105] a fractal dimension on the local variance of the trabecular bone, extracts structural information from 2D projections [120]. However, the trabecular bone score may not be suited to estimate bone strength [85].

The aim of this fractal method is to introduce new structural parameters from QCT that (1) are robust against noise, (2) contain a semantic link to existing microstructural parameters, and (3) contribute to assess key properties of bone health,

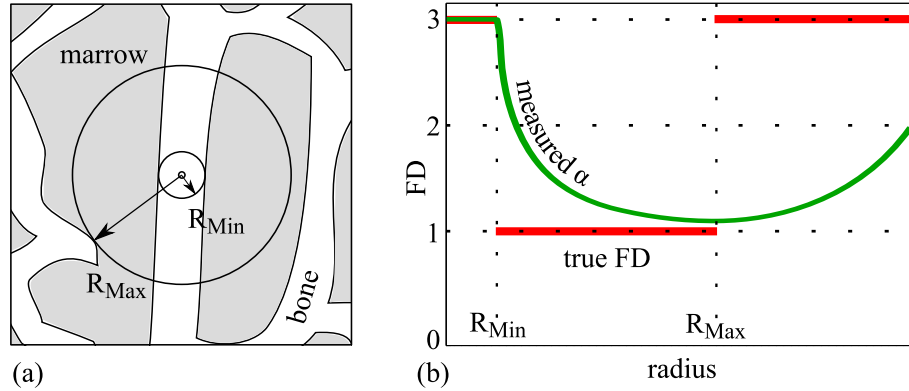


Figure 3.16: Evolution of α , the slope of $\log M_r$ vs $\log r$, on a rod. α is constant 3 at $r < R_{\text{Min}}$, descends smoothly towards 1 at $r \in [R_{\text{Min}}, R_{\text{Max}}]$ and ascends again towards 3 at $r > R_{\text{Max}}$. (a) Spatial illustration of M_r (b) α as a function of the radius r .

such as estimations of bone strength. New fractal methods of RV/BV and Tb.Th are proposed, based on local fractal methods of the Hölder exponent [93, 76].

3.5.2 Materials and Methods

The following subsections describe the fractal method, the image data and the applied statistical methods.

The Hölder exponent in digital images

The 3D Hölder exponent α_r relates the radius r of a sphere with the number of points (or mass) M_r inside that sphere, by computing the slope between $\log r$ and $\log M_r$,

$$\alpha_r = \lim_{a \rightarrow 1} \left(\frac{\log M_{ra} - \log M_{r/a}}{2 \log a} \right). \quad (3.94)$$

If the data consists of infinite thin points, α_r is independent of r : the Hölder exponent α is 1 on a line, 2 on a plane, and 3 on a sphere. This method has been extended for digital images, where voxels are not infinitely thin and to measure rods and plates instead of lines and planes. Rods and plates contain a positive trabecular thickness ($2R_{\text{Min}}$), causing the slope α_r to vary with r . Three different cases are met when measuring α_r on the center of a rod (Fig. 3.16). The slope starts at ($\alpha_r = 3$) for $r < R_{\text{Min}}$, descends smoothly towards one at $r \in [R_{\text{Min}}, R_{\text{Max}}]$ before ascending towards three at $r > R_{\text{Max}}$. The radius R_{Min} is the half of the local trabec-

ular thickness and R_{Max} defines the maximum local radius, which does not intersect with different bone structures. The information of the local rod- or plate-likeness is hidden in the interval $r \in [R_{\text{Min}}, R_{\text{Max}}]$.

Two different methods were defined to extract the fractal dimension, the first method uses only information from the slope α_r , while the second method uses additionally information of the curvature κ_r . First, when assuming that the local structure is sufficiently isolated from neighboring structures ($R_{\text{Max}} > 3R_{\text{Min}}$), the local fractal dimension $FD_1(\vec{x})$ at an arbitrary voxel \vec{x} can be estimated by the minimum of α_r at \vec{x} ,

$$FD_1(\vec{x}) = \min_r \{\alpha_r(\vec{x})\} \quad (3.95)$$

The estimate $FD_1(\vec{x})$ yields an overestimation of the real local fractal dimension, in particular in combination with image noise. The overestimation can be assessed by the curvature κ_r ,

$$\kappa_r = \lim_{a \rightarrow 1} \arctan \left(\frac{\log M_{ra} - 2 \log M_r + \log M_{r/a}}{(\log a)^2} \right). \quad (3.96)$$

An adjusted local slope is now estimated from a function $A(\alpha, \kappa) \in [0, 3]$ which expresses the local fractal dimension in terms of slope and curvature. The local fractal dimension $FD_2(\vec{x})$ is then computed as the minimum of $A(\alpha_r(\vec{x}), \kappa_r(\vec{x}))$,

$$FD_2(\vec{x}) = \min_r \{A(\alpha_r(\vec{x}), \kappa_r(\vec{x}))\}. \quad (3.97)$$

Since values of $\alpha_r(\vec{x})$ are generally larger than the true fractal dimension, which can be estimated with $FD_2(\vec{x})$, the ratio of $FD_2(\vec{x})/\alpha_r(\vec{x})$ grows towards one with increasing radii r . This allows to estimate the limiting radius R_{Min} from a function $\Omega(\alpha, FD_2/\alpha) \in [0, 1]$, which expresses the ratio of R_{Min} and r . The local trabecular thickness $fTb.Th(\vec{x})$ is now estimated the minimum of $2r\Omega(\alpha_r(\vec{x}), FD_2/\alpha_r(\vec{x}))$,

$$fTb.Th(\vec{x}) = \min_r \{2r\Omega(\alpha_r(\vec{x}), FD_2/\alpha_r(\vec{x}))\}. \quad (3.98)$$

Global parameters

To compute the fractal measures on digital volumes of spongy bone, the mass $M_r(\vec{x})$ at voxel \vec{x} was derived with a convolution of a bone map $\text{Bone}(\vec{x})$ and the structural

element $\mathcal{N}_r^{\text{Sphere}} \in [0, 1]$, as defined in Eq. 3.13,

$$M_r(\vec{x}) = (\text{Bone} * \mathcal{N}_r^{\text{Sphere}})(\vec{x}) \quad (3.99)$$

For every voxel, the masses of $N = 25$ different radii were computed, the factor of difference of the radii is given by $a = (R_{\text{Max}}/R_{\text{Min}})^{(1/N-1)}$, as used in Eqs. (3.94) and (3.96), and the radii read $r_i = R_{\text{Min}} a^{(i-1)}$ with $i \in \{1, \dots, N\}$. The maximum and minimum radius were set to $R_{\text{Max}} = 1.0\text{mm}$ and $R_{\text{Min}} = 0.3\text{mm}$. The bone map $\text{Bone}(\vec{x})$ was computed as defined in 2.18, combined with the global micro-structural calibration, Eq. 3.68, which allowed to fix the BV/TV to a constant value.

For the computation of the final VOI-based aggregates, the signals $FD_i(\vec{x})$ and $fTb.Th(\vec{x})$ are locally smoothed (Eq. 3.27) with the Gaussian structural element $\mathcal{N}_k^{\text{Gauss}}$ (Eq. 3.18) and the ridge map Ridge (Eq. 3.40),

$$\bar{S}(\vec{x}) = \text{AVG}_{\mathcal{N}_k^{\text{Gauss}}}(S, \text{Ridge}; \vec{x}) \quad (3.100)$$

with $S \in \{FD_1, FD_2, fTb.Th\}$. The ridge map is defined with $q = 3$, and both, the ridge map and the smoothing use $k = 1\text{mm}$ the a-priori approximation of the trabecular thickness. Now, the global estimates use the formulas for the global average and standard deviation, as defined in 2.12 and 2.13. The final structural parameters for method $i \in 1, 2$ are

- the average fractal dimension,

$$\text{FD}_i = \text{AVG}(\overline{FD}_i, \text{Ridge}) \quad (3.101)$$

- the standard deviation of the local fractal dimension,

$$\text{FD}_i.\text{SD} = \text{SD}(\overline{FD}_i, \text{Ridge}), \quad (3.102)$$

- the fractal trabecular thickness,

$$\text{fTb.Th} = \text{AVG}(\overline{fTb.Th}, \text{Ridge}), \quad (3.103)$$

- and the coefficient of variation of the local fractal trabecular thickness,

$$\text{fTb.Th.CV} = \frac{\text{SD}(\overline{\text{fTb.Th}}, \text{Ridge})}{\text{AVG}(\overline{\text{fTb.Th}}, \text{Ridge})}. \quad (3.104)$$

- Under the assumption that the volume contains only rods and plates, and with $\text{FD}_1^{\text{Noise}} = 2.0$ and $\text{FD}_2^{\text{Noise}} = 1.45$ at a threshold value generating $\text{BV}/\text{TV} = 25\%$ the fractal rod volume ratio fRV_i/BV is defined as

$$\text{fRV}_i/\text{BV} = \frac{\sum_{\vec{x}} \max\{0, \text{FD}_i^{\text{Noise}} - \overline{\text{FD}_i}(\vec{x})\} \cdot \text{Ridge}(\vec{x})}{\sum_{\vec{x}} |\text{FD}_i^{\text{Noise}} - \overline{\text{FD}_i}(\vec{x})| \cdot \text{Ridge}(\vec{x})}. \quad (3.105)$$

The range of $\overline{\text{FD}_i}(\vec{x})$ is decreased in noisy scenarios, inducing an overestimation of rods and an underestimation on plates or entirely filled regions and $\overline{\text{FD}_i}(\vec{x})$ collapses to a constant value $\text{FD}_i^{\text{Noise}}$ at a signal-to-noise ratio of 1. The fractal plate volume ratio is given by $\text{fPV}/\text{BV}_i = 1 - \text{fRV}/\text{BV}_i$. Figure 3.17 shows the application of a phantom of three rods and plates under noiseless and noisy conditions. The signal $\text{FD}_1(\vec{x})$ contains low variation inside rods or plates, and $\text{FD}_2(\vec{x})$ minimizes the error with the ground-truth.

Defining the look-up tables

The functions $A(\alpha, \kappa)$ and $\Omega(\alpha, \text{FD}/\alpha)$ were derived from the evolution of the intersection of a sphere of radius r with a sphere, rod, plate of radius R_{Min} , representing the integer fractal dimensions 0, 1, and 2. The fractal dimension 3 was directly obtained from the volume of a sphere with radius r . The masses of these structures are

$$M_r^{\text{FD}} = \begin{cases} 4/3\pi R_{\text{Min}}^3, & \text{if FD} = 0 \wedge r > R_{\text{Min}} \\ \pi R_{\text{Min}}^2 (3\hat{r} + r) + \frac{\pi}{3} (r - \hat{r})^3, & \text{if FD} = 1 \wedge r > R_{\text{Min}} \\ \pi R_{\text{Min}} (2r^2 - 2/3 R_{\text{Min}}^2), & \text{if FD} = 2 \wedge r > R_{\text{Min}} \\ 4/3\pi r^3, & \text{if FD} = 3 \vee r \leq R_{\text{Min}} \end{cases}, \quad (3.106)$$

with $\hat{r} = \sqrt{r^2 - R_{\text{Min}}^2}$. The logarithms of these volumes were then interpolated for non integer fractal dimensions and the slope α and the curvature κ , expressed in radians, were computed for $r \in [0, 10 R_{\text{Min}}]$. To obtain the map $A(\alpha, \kappa)$, the known fractal dimension FD was fitted as a surface of α and κ . Figure 3.18 shows the

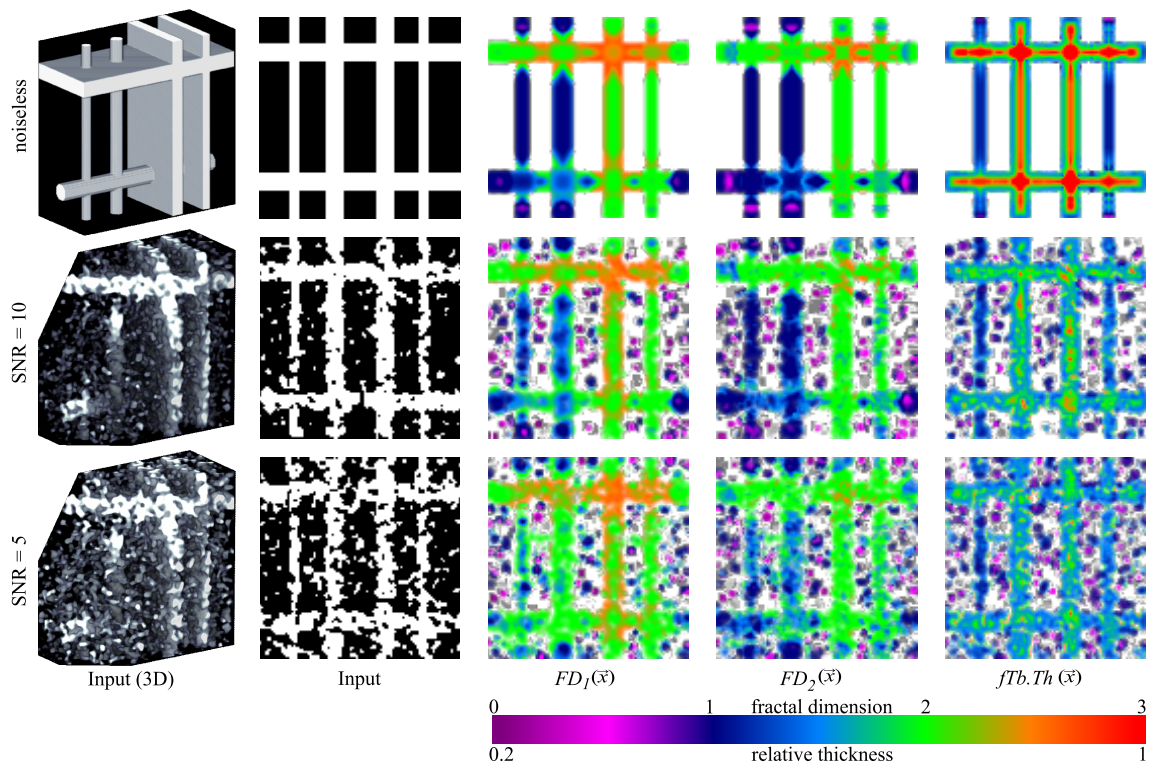


Figure 3.17: Application of the fractal method on a synthetic phantom consisting of two vertical rods and plates and one horizontal rod and plate of different thickness. Rows: (1) noiseless phantom, (2) signal-to-noise ratio = 10, (3) signal-to-noise ratio = 5. Columns: (1) volumetric rendering, (2) middle slice through the phantom, (3) $FD_1(\vec{x})$, (4) $FD_2(\vec{x})$, (5) $fTb.Th(\vec{x})$.

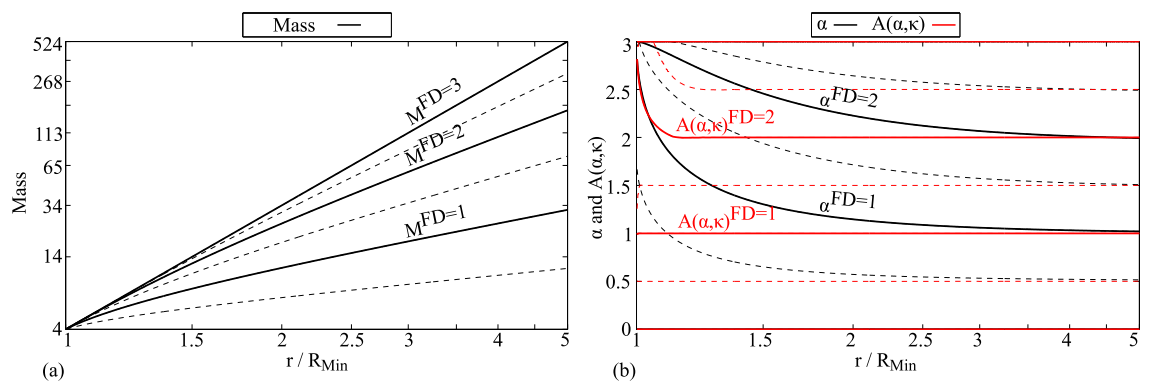


Figure 3.18: (a) Evolution of the prototype masses with r for $FD = 0, 0.5, 1, \dots, 3$, (b) Hölder exponents α and $A(\alpha, \kappa)$ of the prototype and interpolated volumes.

evolution of the volumes and the estimates of α and $A(\alpha, \kappa)$, α requires much larger radii ($r > 3 R_{\text{Min}}$) to obtain a close estimate to the true fractal dimension than $A(\alpha, \kappa)$ ($r > 1.2 R_{\text{Min}}$). In a similar way to the estimation of the fractal dimension, the map for the trabecular thickness $\Omega(\alpha, FD/\alpha)$ was obtained from the known values of r/R_{Min} as a surface interpolation of α and FD/α . The algorithm was developed in Matlab (v8.1, The MathWorks, Inc., Natick, MA, USA).

Experiments

Two data sets were analyzed: the experiment of the vertebra phantoms, Sec. 3.1.1, served to obtain robustness of the method with respect to precision and accuracy, the data of the Bioasset study, Sec. 3.1.3, served to predict the failure load F_{exp} and to obtain correlations between all parameters. The HRpQCT-data (Ground truth (1)) was used as ground-truth of the first experiment.

The following standard parameters were computed: bone mineral density (BMD), bone volume fraction (BV/TV), and tissue mineral density (TMD); with a model dependent method trabecular number (Tb.N), mean intercept length (MIL), and bone surface ratio (BS/BV); and model independently [54] trabecular separation (Tb.Sp), trabecular thickness (Tb.Th), and structure model index (SMI).

The threshold for computing the microstructural and fractal parameters was group-wise adjusted to compensate systematic differences between the QCT, HR-QCT and HRpQCT scans, using the global microstructural calibration, Sec. 3.3.3, according to [48, 56]. The threshold was selected in order to obtain $BV/TV \approx 10\%$ on HRpQCT[75] and $BV/TV \approx 25\%$ on QCT and HRQCT. Calibration of the HRpQCT scans was performed with the scanners software (Scanco Medical AG, Brüttisellen, Switzerland), and registration, calibration, and computation of the standard parameters were performed with Structural Insight (v3.1, Biomedical Imaging, University of Kiel, Germany).

Precision and accuracy were derived from the vertebra phantoms, using the metrics STP and LTP, Sec. 3.1.2. The sample size and the number of repeated scans were sufficient to claim statistical significance at a level considered appropriate for characterizing STP and LTP [40]. Average, standard deviation, quartiles, and Spearman's rank correlation coefficients (ρ) were computed from the BioAsset data (76 vertebrae), p-values were Bonferroni corrected for multiple comparisons.

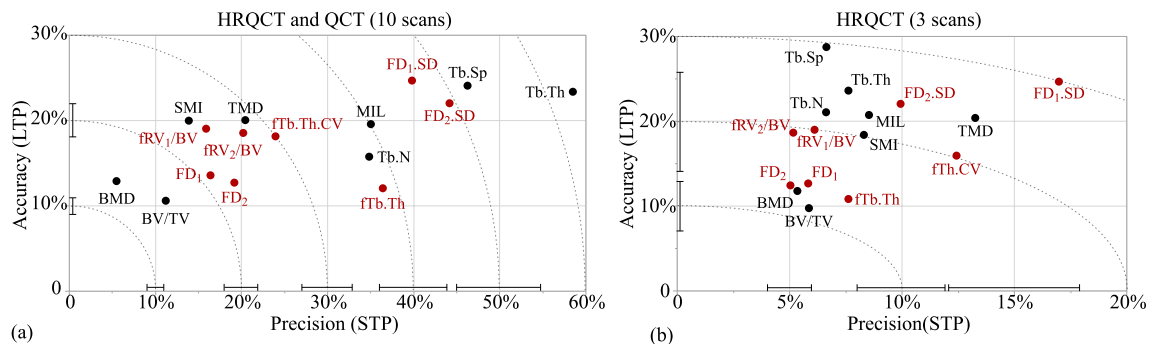


Figure 3.19: Precision (STP) vs accuracy (LTP) with confidence intervals. Lowest values represent highest trueness and reproducibility, isobars depict compound errors of both metrics, (a) ten scans (HRQCT and QCT with and without body ring, confidence intervals of $p < 0.025$), (b) three scans (HRQCT without additional body ring, confidence intervals of $p < 0.1$).

For 17 vertebrae, linear models for the prediction of F_{exp} were derived from BMD in combination with up to three microstructural parameters. R^2 , RMSE, and adjusted R^2 ($\text{adj}R^2$) were computed and a robust R^2 ($\text{rob}R^2$) and RMSE (robRMSE) were obtained from leave-one-out cross-validation of all combinations. The optimum regression models between F_{exp} and fractal or standard structural parameters were selected as those with the minimum corrected Akaike information criterion (AIC_c), see Sec. 3.1.4. The analysis was performed with JMP (v11, SAS Institute, Inc., Cary, NC, USA) and Matlab.

3.5.3 Results

Precision and accuracy

Figure 3.19 a) shows the precision (STP) and accuracy (LTP) of all structural parameters on ten repeated scans. Highest precision and accuracy (STP, LTP) were obtained by BMD (6%, 13%) and BV/TV (11%, 11%). From the microstructural parameters, FD (16% – 19%, 13%) was most robust, followed by fRV/BV (16% – 20%, 19%), SMI (14%, 20%), and TMD (20%, 20%). The parameter fTb.Th contained low precision but high accuracy (36%, 12%). However, its pendant Tb.Th (58%, 32%) still contained higher errors regarding both metrics. If considering only three repeated scans with a minimum noise level, Fig. 3.19 b), STP generally decreased while LTP remained unchanged. In particular, FD (5% – 6%, 12% – 13%), fRV/BV (5% – 6%, 19%), and fTb.Th (8%, 11%) obtained similar robustness as

BMD (5%, 12%) and BV/TV (6%, 10%). Improved precision was also observed on FD₂.SD, Tb.N, Tb.Th, and Tb.Sp.

Descriptive statistics and correlations between parameters

Parameter	Avg	SD	Q_1	Q_3
FD ₁	2.12	0.04	2.08	2.15
FD ₂	1.57	0.05	1.54	1.60
FD ₁ .SD	0.32	0.02	0.30	0.34
FD ₂ .SD	0.32	0.03	0.30	0.34
fRV ₁ /BV(%)	29.3	6.6	24.0	35.0
fRV ₂ /BV(%)	28.6	6.1	23.7	32.7
fTb.Th(mm)	1.10	0.02	1.09	1.12
fTb.Th.CV(%)	13.8	0.5	12.3	13.3
BMD(mg/cm ³)	54.0	19.5	43.8	69.2
TMD(mg/cm ³)	206.1	7.8	201.7	211.8
BV/TV(%)	25.0	1.5	24.0	26.1
Tb.N(mm ⁻¹)	0.67	0.07	0.62	0.72
Tb.Th(mm)	0.39	0.05	0.35	0.43
Tb.Sp(mm)	0.95	0.13	0.85	1.04
SMI	0.16	0.10	0.08	0.22
F _{exp} (kN)	2.10	0.50	1.75	2.47
Age(yr)	80.9	7.1	75.5	86.0
BMI(kg/m ²)	22.4	4.7	18.7	26.5

Table 3.2: Fractal, densitometric and microstructural parameters ($N = 76$), biomechanical data F_{exp} ($N = 17$) and donors' characteristics ($N = 33$).

The parameter FD₁ showed higher values than FD₂, while values of fRV₁/BV and FD₁.SD were similar to fRV₂/BV and FD₂.SD, respectively (Tab. 3.2). The parameter fTb.Th contained higher estimates than Tb.Th (and Tb.Sp) but reduced variation (SD/Avg). Spearman's rank correlation coefficients (ρ) between all parameters are shown in Tab. 3.3 with the exception of BS/BV, since it contained the same values as MIL. In general, the standard parameters correlated with each other, as did the fractal parameters, while the correlation between parameters of both groups was rather low. An exception was fTb.Th which contained significant correlations to all parameters with exception of BMD and FD.SD. The correlation between fTb.Th and Tb.Th ($\rho = 0.75^*$) was not noticeably stronger than between fTb.Th and other structural parameters (Tb.N: $\rho = -0.79^*$, SMI: $\rho = 0.84^*$).

	BMD	FD ₁	FD ₁ .SD	fRV ₁ /BV	FD ₂	FD ₂ .SD	fRV ₂ /BV	fTb.Th	fTb.Th.CV	BV/TV	TMD	Tb.N	Tb.Th	Tb.Sp	MIL	SMI
FD ₁	0.00															
FD ₁ .SD	0.29	0.28														
fRV ₁ /BV	0.05	-0.98*	-0.12													
FD ₂	0.06	0.96*	0.43*	-0.91*												
FD ₂ .SD	0.21	0.47*	0.94*	-0.32	0.63*											
fRV ₂ /BV	0.00	-0.98*	-0.25	0.97*	-0.98*	-0.46*										
fTb.Th	-0.11	-0.79*	-0.27	0.77*	-0.67*	-0.33	0.68*									
fTb.Th.CV	0.13	0.74*	0.55*	-0.67*	0.72*	0.60*	-0.66*	-0.87*								
BV/TV	0.38	0.15	-0.03	-0.18	0.03	-0.11	-0.06	-0.59*	0.35							
TMD	-0.01	-0.31	-0.05	0.30	-0.16	-0.01	0.17	0.65*	-0.40*	-0.61*						
Tb.N	-0.04	0.37	-0.12	-0.40*	0.16	-0.14	-0.22	-0.79*	0.50*	0.73*	-0.72*					
Tb.Th	0.15	-0.36	0.11	0.39	-0.15	0.13	0.20	0.75*	-0.49*	-0.55*	0.73*	-0.96*				
Tb.Sp	0.05	-0.34	0.10	0.37	-0.13	0.14	0.19	0.75*	-0.47*	-0.66*	0.66*	-0.98*	0.95*			
MIL	0.32	-0.39	0.16	0.41*	-0.17	0.14	0.24	0.66*	-0.43*	-0.27	0.58*	-0.84*	0.93*	0.86*		
SMI	-0.05	-0.48*	0.07	0.51*	-0.29	0.05	0.35	0.84*	-0.55*	-0.77*	0.75*	-0.94*	0.87*	0.87*	0.72*	
F _{exp}	0.84*	-0.14	0.71	0.30	0.04	0.45	0.05	-0.05	0.32	0.25	-0.05	-0.20	0.24	0.20	0.47	0.11

Table 3.3: Spearman's rank correlation coefficients (ρ) between density, fractal dimension, microarchitectural parameters ($N = 76$) and vertebral failure load ($N = 17$), $p < 0.05$, bold $p < 0.01$ (two-tailed correlation is significant with Bonferroni correction).

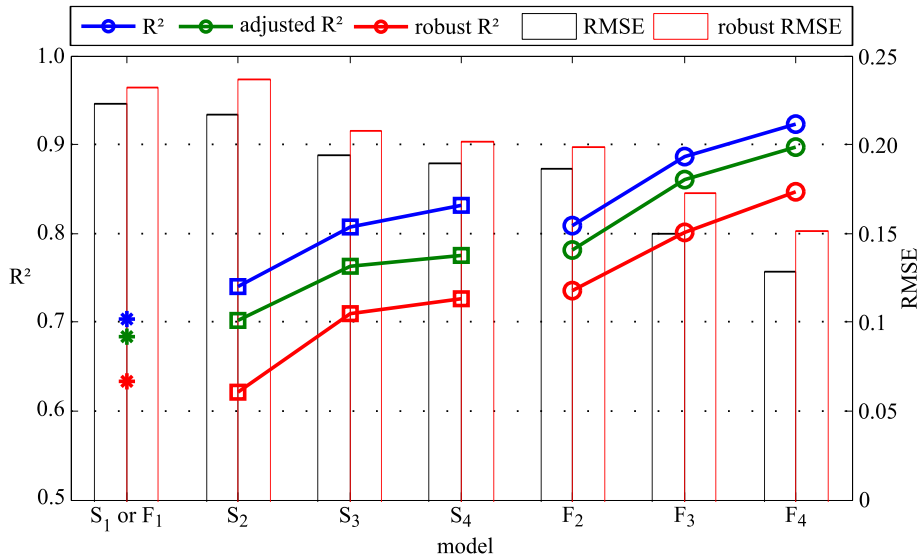


Figure 3.20: R^2 , $\text{adj}R^2$, $\text{rob}R^2$, RMSE, and $\text{rob}RMSE$ of linear models for prediction of F_{exp} .

Multiple regression analysis with failure load as dependent variable

	S_1 or F_1	S_2	S_3	S_4		F_2	F_3	F_4
BMD	< 0.0001*	0.0002*	0.0002*	0.0007*	BMD	< 0.0001*	< 0.0001*	< 0.0001*
MIL		0.188	0.043*	0.095	FD ₁ .SD	0.015*	0.0008*	0.0005*
BS/BV			0.053	0.151	FD ₂		0.011*	0.018*
TMD				0.213	fRV ₂ /BV			0.036*
AICc	2.813	4.123	3.172	5.830	AICc	-1.139	-5.900	-7.478

Table 3.4: P-Values of the predictors ($*p < 0.05$) and total AICc obtained from optimal models for prediction of F_{exp} with and without incorporating fractal methods.

Table 3.4 and Fig. 3.20 show multiple linear regression models to explain the variability of F_{exp} . The first set (S_1 to S_4) was based on BMD and (not fractal) standard parameters, the second set (F_1 to F_4) was based on BMD and fractal parameters. The indices of the model names indicate the number of used predictors. Although the actual predictors were chosen independently as the combination that minimizes the AICc, the best models contained always all predictors of the best preceding models (for instance $S_4 = S_3 + \text{TMD}$). The highest simple correlation with F_{exp} was obtained by BMD ($S_1 = F_1$: $\text{adj}R^2 = 0.684$, $\text{rob}R^2 = 0.634$, $\text{rob}RMSE = 0.231$, $\text{AICc} = 2.81$). The AICcs indicated a significant gain of information by F_{2-4} compared to S_{1-4} . Model F_2 with BMD and FD₁.SD ($\text{adj}R^2 = 0.782$, $\text{rob}R^2 = 0.736$,

robRMSE = 0.197, AICc = -1.14) obtained already higher correlations and lower errors than all S-models. Adding additionally FD₂ as a predictor (model F_3 : adjR² = 0.861, robR² = 0.801, robRMSE = 0.171, AICc = -5.90) significantly raised the gain of information towards standard models ($p(F_3 \text{ vs. } S_{1-4}) = 0.003^* - 0.013^*$). The optimum model was obtained by adding fRV₂/BV as a further predictor (model F_4 : adjR² = 0.897, robR² = 0.847, robRMSE = 0.150, AICc = -7.48), yielding a significant gain of information towards S_{1-4} ($p(F_4 \text{ vs. } S_{1-4}) = 0.001^* - 0.006^*$) and F_2 ($p(F_4 \text{ vs. } F_2) = 0.042^*$). P-values of the parameter estimates (Tab. 3.4) showed significant contributions of all fractal parameters to the F-models while standard parameters, with exception of MIL in model S_3 , did not contribute significantly to the S-models.

When allowing only parameters obtained with the first fractal method, the predictors FD₂ and fRV₂/BV of models F_3 and F_4 have been replaced by FD₁ and fRV₁/BV. These models with three (adjR² = 0.844, robR² = 0.771, robRMSE = 0.186, AICc = -3.97) and four predictors (adjR² = 0.891, robR² = 0.833, robRMSE = 0.157, AICc = -6.48) were not significantly different to the models F_3 and F_4 based on both fractal methods. Models, based on the Bayes information criterion were identical to these selected with the AICc.

3.5.4 Discussion

Compared to standard microstructural parameters, the fractal methodology improved the prediction of failure load and showed robustness against image noise. In particular FD.SD, FD, and fRV/BV demonstrated to be well adjusted for the analysis of HRQCT volumes. Prediction of the failure load with standard microstructure parameters can explain up to 86% of the variability in vertebral failure load, for instance, by using a linear model of BMD, SMI, and DA on HRpQCT (isotropic resolution 82 μ m)[140]. However, such a predictive power has not been observed before on HRQCT due to the high sensitivity of noise of standard microstructural parameters. Regression models with standard structural parameters (S_{2-4}) were not able to extract additional information of F_{exp} . Conversely, the fractal model F_3 , based on BMD, FD₁.SD, and FD₂, explained 86% (adjR²) of the vertebral failure load on in-vivo-like image conditions, thus bridging the gap between ex-vivo and in-vivo. Model F_4 , based on BMD, FD₁.SD, FD₂ and fRV₂/BV, explained up to 90% (adjR²) of the variability of F_{exp} . Models F_3 and F_4 signifi-

cantly improved the extraction of information beyond BMD without overfitting, as indicated by AICc's, robR^2 and robRMSE . This highlights the different aspects of bone quality captured by the set of fractal parameters. The results also showed that the same fractal parameters obtained with either of the both fractal methods were nearly redundant as they did not add independent information in any linear regression model and also showed high Spearman's rank correlations (FD: $\rho = 0.96^*$, FD.SD: $\rho = 0.94^*$, fRV/BV : $\rho = 0.97^*$). Thus, for the prediction of failure load, one could simply implement the first fractal method rather than both methods, explaining 84% (adjR^2) with the model of three and 89% with the model of four predictors. Robustness against image degradation is particularly important for in-vivo microstructural parameters. Precision or reproducibility (STP) is important to derive longitudinal skeletal changes. Accuracy or trueness (LTP), on the other hand, reflects robustness against inhomogeneous settings (different protocols, scanners) and defines, in particular, the ability to translate results from phantom- to patient-studies[40]. In this study, both the accuracy and precision of the structural information improved if computed with fractal methods. In particular, fTb.Th improved the accuracy of Tb.Th though still significantly correlated: $\rho(\text{fTb.Th}, \text{Tb.Th}) = 0.75^*$. The parameters fRV/BV and FD improved the accuracy of SMI. However, in contrast to fRV/BV and FD, SMI generally measures the convexity of the trabecular bone rather than its structural model [115]. This might explain the weak correlations between SMI and the related fractal parameters (FD_1 : $\rho = -0.48^*$, fRV_1/BV : $\rho = 0.51^*$, FD_2 : $\rho = -0.29$, fRV_2/BV : $\rho = 0.35$). Results of fRV/BV (mean: 29%, SD: 6.4%) showed agreement with an alternative parameter of RV/BV on HRpQCT resolution [75] (mean: 17.5%, SD: 6.9%). This indicates the inadequacy of the strict parallel plate model in the vertebral domain. High correlations with F_{exp} were only obtained with BMD ($\rho = 0.84^*$) and FD.SD ($\rho = 0.71$). The BMD was not correlated with the fractal parameters FD ($\rho = 0.0 - 0.06$), FD.SD ($\rho = 0.21 - 0.29$), and fRV/BV ($\rho = 0.0 - 0.05$), while BMD and all of these fractal parameters contributed significantly to the prediction of F_{exp} in model F_{2-4} . Hence the fractal parameters are able to characterize the failure load from the bone microstructure rather than from the bone density, as obtained with BMD. In general, unless one defines a mathematical mapping between hidden fine scale structural information and visible coarse scale information, high noise and low effective in-vivo resolution ($500 \times 500 \times 650 \mu\text{m}^3$)[71] impedes ability

to obtain failure load from the bone in in-vivo HRQCT volumes. Self-similarity, the property to extrapolate structural information from coarse to fine scale, makes fractal methods robust against low resolution and image degradation due to noise. Scale invariance and thus, accuracy, applies almost completely to fractal methods, but not to standard microstructural parameters. Most algorithms of microstructural parameters require a crisp threshold which discards a great portion of the contained information. In contrast, the fractal methods proposed here not only allow the application of a crisp threshold, but also the application of a sigmoidal fuzzy threshold. Nevertheless, the conducted experiments required the choice of a crisp threshold for the purpose of a fair comparison between fractal and standard parameters. The threshold was individually adapted from the histogram to remove most correlations of the microstructural parameters with BMD [48]. Alternative tests with global thresholds of 150, 200, and 250 mg/cm³ showed less performance on the standard microstructural parameters, which means higher correlation with BMD and lower ability to predict the failure load.

Finally, some alternative uses can be drawn from the method proposed here. Local qualitative indicators of bone health $FD_1(\vec{x})$, $FD_2(\vec{x})$ and $fTb.Th(\vec{x})$ (Fig. 3.17) could be beneficial for the segmentation of multiple myeloma [12, 13], or to extend the local information of finite element models [80, 20]. Furthermore, replacing the input volume with a skeletonized version of the bone [71] likely improves the estimation of $FD_1(\vec{x})$ and $FD_2(\vec{x})$ but however, impairs the estimation of $fTb.Th(\vec{x})$. Conversely, since skeletonization is a complex task in 3D, as noise and uncertainties need to be carefully treated without removing the relevant plates and rods, this adjustment might be only reasonable on HRpQCT.

3.5.5 Conclusion

The new fractal method proposed for the analysis of clinical 3D QCT and HRQCT volumes computes the RV/BV and Tb.Th. It does not require a well-defined skeleton, and is applicable with fuzzy threshold functions. Precision and accuracy tests demonstrated that the method can withstand image noise from in-vivo conditions. The fractal measurements outperformed most of the microstructural parameters in precision (STP) by as much as 20% – 45% (MIL, Tb.Sp, Tb.Th). The accuracy (LTP) of fractal parameters FD and fTb.Th was almost as high as that of BMD or BV/TV. On the ex-vivo human vertebrae, HRQCT-based linear prediction models of

the failure load improved significantly by using fractal rather than standard predictors, and can exceed the quality of reported predictive models of ex-vivo HRpQCT resolution [140]. Thus, application of fractal methods may grant further insight into the study of bone quality in-vivo when image resolution and quality are less than optimal for current standard methods.

3.6 Local Texture Descriptors on Diffusion Magnetic Resonance Imaging of the Brain

The material of this section has been published in the International Journal of Computer Assisted Radiology and Surgery [133] and aims to demonstrate the application of the local operators. Since the direct evaluation of local operators on CT images of the vertebra is difficult, this section handles instead brain DTI imaging where the voxel-wise evaluation is a standard approach. This allows a direct evaluation of the local texture operators without the need of performing any post-hoc aggregation with global parameters.

Descriptors extracted from magnetic resonance imaging (MRI) of the brain can be employed to locate and characterize a wide range of pathologies. Scalar measures are typically derived within a single voxel unit, but neighborhood-based texture measures can also be applied. In this chapter a new set of descriptors is proposed to compute local texture characteristics from scalar measures of diffusion tensor imaging (DTI), such as mean and radial diffusivity, and fractional anisotropy.

Weighted rotational invariant local operators are employed, namely standard deviation, inter-quartile range, coefficient of variation, quartile coefficient of variation, and skewness. Sensitivity and specificity of those texture descriptors were analyzed with tract-based spatial statistics of the white matter on a diffusion MRI group study of elderly healthy controls (HC), patients with mild cognitive impairment (MCI), and mild or moderate Alzheimer's disease (AD). In addition, robustness against noise has been assessed with a realistic diffusion weighted imaging phantom and the contamination of the local neighborhood with gray matter has been measured.

The new texture operators showed an increased ability for finding formerly undetected differences between groups compared to conventional DTI methods. In particular, the coefficient of variation, quartile coefficient of variation, standard deviation and inter-quartile range of the mean and radial diffusivity detected significant

differences even between previously not significantly discernible groups, such as MCI vs. moderate AD and mild vs. moderate AD. The analysis provided evidence of low contamination of the local neighborhood with gray matter and high robustness against noise.

The local operators applied here enhance the identification and localization of areas of the brain where cognitive impairment takes place, and thus indicate them as promising extensions in diffusion MRI group studies.

3.6.1 Introduction

Diffusion MRI is predominantly interpreted as a modality to estimate the spatial distribution of the diffusion of water molecules [8]. One common diffusion MRI model is diffusion tensor imaging (DTI), which describes the tensor of the diffusion directions. DTI found numerous applications in the study of neurosurgery [73], psychiatric [72] and neurological disorders [126], and is most commonly applied on the white matter (WM) of the brain [55] where water tends to diffuse preferentially parallel to fiber tracts because the myelin sheath and cell membranes impede the diffusion perpendicular to the direction of the axons. Given that the diffusion tensor is a mathematical entity whose comparison and interpretation is not straightforward, most DTI group studies rely on scalar measures which encode different rotationally invariant properties of the original diffusion tensor.

The most commonly employed measures are fractional anisotropy (FA) and mean diffusivity (MD) [119]. Also useful for describing the diffusion are radial and axial diffusivity [17], linear measure, tensor mode [27] and others [7, 31, 94]. The choice of suitable scalar measures is a critical step for DTI analyses, as their robustness to noise, or sensitivity and specificity to the pathological condition (i.e. ability to discriminate healthy from diseased patients, or between patients with different disease states) have a key role in the performance of the studies.

Most of the literature related to the derivation of new DTI scalar measures has focused on the behavior of different anisotropy measures with respect to noise. It is worth to note that most of the recently proposed anisotropy indices have similar contrast-to-noise ratio than FA [65, 139]. Only few DTI methods, which incorporate a local neighborhood, have been described. The lattice index [104] measures the similarity of the predominant diffusion directions on a local weighted neighborhood in 2D. The inter-voxel local diffusion homogeneity [44] uses an unweighted 3D

neighborhood. The local diffusion homogeneity might be sensitive to age-related changes in WM but less robust than MD or FA against motion artifacts in the MRI acquisition process [69]. Neither of these methods is rotational invariant.

The aim of this section is to present new DTI descriptors to improve the identification of subtle differences of the integrity of the white matter architecture between healthy and diseased brains (dementia, multiple sclerosis, stroke, aging etc.). Our hypothesis is that well defined texture operators, attached to existing scalar measures, can improve the identification of differences of the white matter architecture between patients with different levels of cognitive impairment. A new set of image filtering methods is proposed that operates directly on traditional scalar measures using rotationally invariant weighted local descriptors (average, standard deviation, coefficient of variation, skewness etc.) to improve the discriminative power and robustness against noise. These statistical descriptors are inter-voxel in nature and may extract additional texture information that was not revealed by the original scalar measures, allowing to localize formerly undetected areas and opening a door to new viewpoints for the analysis of neuronal pathologies.

For the evaluation of the texture operators, the performance with a real-world DTI group study is analyzed, instead of indirectly assessing the sensitivity and specificity to disease by means of the ability to distinguish between different types of brain tissue. An Alzheimer's disease (AD) study with four distinct cohorts has been chosen and the final analysis has been restricted to three input scalar measures MD, RD and FA, which were shown to differentiate well on AD [119]. Tract-based spatial statistics (TBSS) are employed as they have become widely accepted for such analyses [125]. In addition, the overlap of the neighborhood with gray matter has been analyzed and the performance of the local operators with respect to Rician noise has been examined.

3.6.2 Materials and methods

For the separate evaluation of each anatomical entity with TBSS, the following image processing steps are performed, Fig. 3.21: DTI is estimated from DWI volumes and thereafter the traditional single-voxel scalar measures (MD, RD or FA) are derived. Now, the inter-voxel descriptors are computed from the scalar measures using a local weighting mask. The final steps are the registration of the single- and inter-voxel measures to a standard atlas space and the projection to the registered WM skeleton,

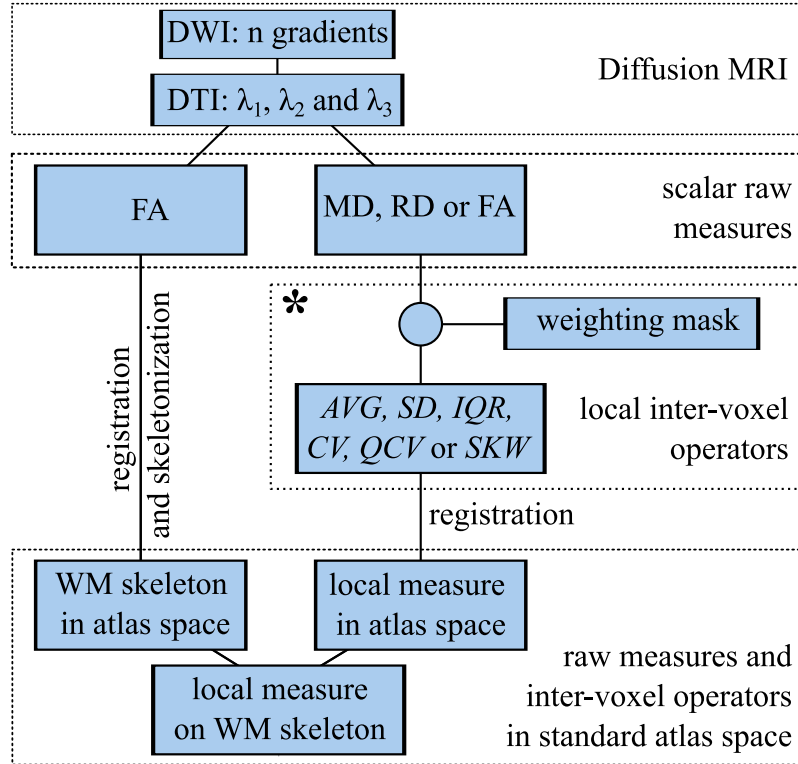


Figure 3.21: DTI scalar measures (MD, RD or FA) are filtered with weighted local inter-voxel operators (*). Then they are registered to atlas space and projected to the WM skeleton, allowing to derive statistical comparisons between patients.

which is derived from FA. The following subsections review the traditional scalar measures Sec. 3.6.2, the proposed inter-voxel operators Sec. 3.6.2 and the conducted experiments, Secs. 3.6.2 and 3.6.2.

Scalar measures

The definitions of the scalar measures that were employed in this section are briefly revised. Given a diffusion tensor and its three eigenvalues $\lambda_1 \geq \lambda_2 \geq \lambda_3$, the Mean Diffusivity is a measure of the total amount of diffusivity

$$MD = \bar{\lambda} = \frac{\lambda_1 + \lambda_2 + \lambda_3}{3}. \quad (3.107)$$

The Radial Diffusivity, on the other hand, measures how much diffusivity remains perpendicular to the main diffusion direction

$$\text{RD} = \frac{\lambda_2 + \lambda_3}{2}, \quad (3.108)$$

and the Fractional Anisotropy measures how much the diffusion deviates from isotropy

$$\text{FA} = \sqrt{\frac{3}{2}} \frac{\sqrt{(\lambda_1 - \bar{\lambda})^2 + (\lambda_2 - \bar{\lambda})^2 + (\lambda_3 - \bar{\lambda})^2}}{\sqrt{\lambda_1^2 + \lambda_2^2 + \lambda_3^2}}. \quad (3.109)$$

The following additional scalar measures were computed but finally discarded as they did not add much information with respect to the ones described in this work: linear, planar and spherical measure [141], anisotropy and elongation index [10] and an operator describing the DTI ellipsoid in terms of being oblate or prolate [138].

Local inter-voxel operators

Linear and non-linear local inter-voxel texture operators are computed. Both incorporate the Gaussian weighting mask $\mathcal{N}_k^{\text{Gauss}}$ (Sec. 3.2.1) and a binary volume of interest VOI, containing ones inside and zeros outside the brain. The weighting mask is rotationally invariant and monotonic decreasing from the center voxel, and thus minimizes remote influences of potential gray matter voxels within the neighborhood. To compute meaningful 3D information, the mask must contain at least three non-trivial voxels in each direction but must be small enough not to contaminate the texture information with gray matter voxels. Formulas for the linear and non-linear operators were introduced in Sec. 3.2.2. Since all of these parameters use the same mask $\mathcal{N}^{\text{Gauss}}$ and the same VOI, they are simply abbreviated as $\text{AVG}(\vec{x})$ of s or $\text{SD}(\vec{x})$ of s instead of $\text{AVG}_{\mathcal{N}^{\text{Gauss}}}(s, \text{VOI}; \vec{x})$ or $\text{SD}_{\mathcal{N}^{\text{Gauss}}}(s, \text{VOI}; \vec{x})$ etc. The following six scalar measures were computed,

- the weighted average $\text{AVG}(\vec{x})$,
- the weighted standard deviation $\text{SD}(\vec{x})$,
- the weighted coefficient of variation $\text{CV}(\vec{x})$,
- the weighted standardized skewness $\text{SKW}(\vec{x})$,
- the weighted inter-quartile range $\text{IQR}(\vec{x})$ and

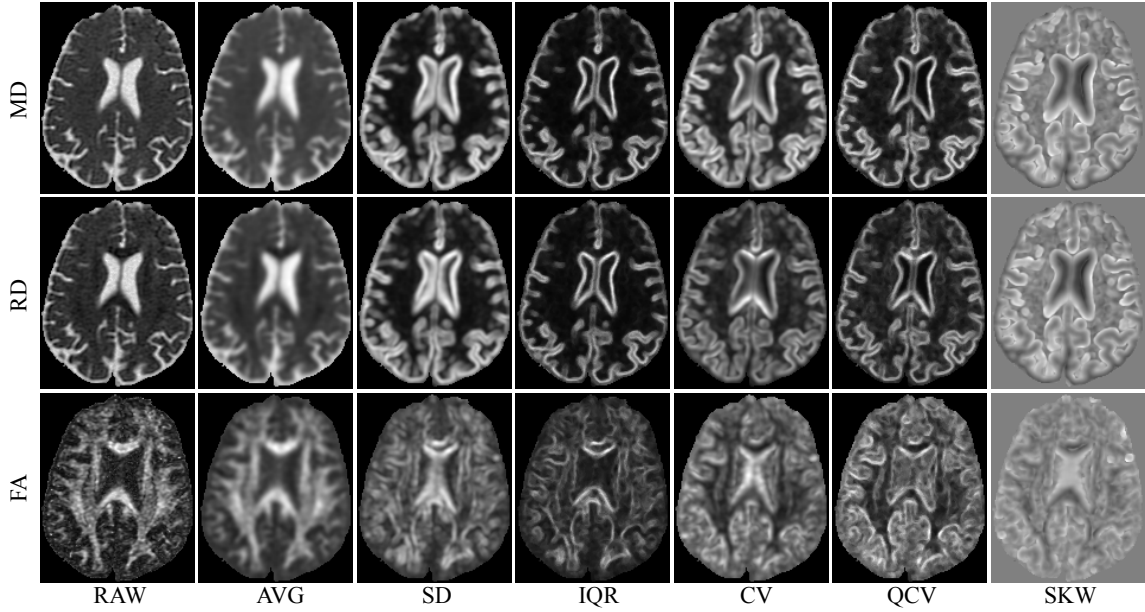


Figure 3.22: DTI measures obtained from a healthy patient (voxel size $1.015 \times 1.015 \times 3\text{mm}^3$, matrix is cropped to 131×162 voxels) obtained with $\mathcal{N}_{4\text{mm}}^{\text{Gauss}}$ (mask size $7 \times 7 \times 3$). Rows: MD, RD and FA. Columns: single-voxel measure (RAW) and inter-voxel operators average (AVG), standard deviation (SD), inter-quartile range (IQR), coefficient of variation (CV), quartile coefficient of variation (QCV) and skewness SKW).

- the weighted quartile coefficient of variation $\text{QCV}(\vec{x})$

Additionally, the empty identity operator of the signal s is denoted as RAW

$$\text{RAW}(\vec{x}) = s(\vec{x}). \quad (3.110)$$

Figure 3.22 shows axial views of all scalar measures (RAW) and inter-voxel operators for a certain sample case. AVG contains the smoothed information of RAW. The parameters IQR and QCV represent non-linear counterparts of SD and CV. SD and IQR emphasize areas with a high local gradient similar to their scale invariant counterparts CV and QCV. The third moment SKW reveals different information than the other operators, which becomes visually apparent in the case of MD and RD. However, SKW FA equals to a certain extent the CV and QCV of FA. The weighted standardized kurtosis was derived in a similar manner to the other linear operators, but later excluded due to its weak sensitivity and specificity against changes in the pathology.

Analysis of diagnostic performance

A DTI group study with four age adjusted cohorts was analyzed ($N = 58$ patients). The study contained healthy controls (HC: $N = 19$, age = 74.05, SD = 0.88y), patients with mild cognitive impairment (MCI: $N = 12$, age = 76.33, SD = 1.11y), patients with mild Alzheimer’s disease (Mild AD: $N = 20$, age = 76.30, SD = 0.86y) and patients with moderate Alzheimer’s disease (Mod AD: $N = 7$, age = 76.57, SD = 1.45y). Raw diffusion weighted images (DWIs) were acquired with a GE Signa 1.5 T MRI unit at QDiagnóstica radiological facilities in Valladolid, Spain. The parameters of the acquisition protocol were the following: 25 gradient directions, $b=1000\text{s/mm}^2$, one baseline volume, voxel size $1.015 \times 1.015 \times 3\text{mm}^3$, TR=13s, TE=85.5ms, 256×256 matrix, NEX=2 and 39 slices covering the entire brain.

The DWIs were linearly registered to the baseline volume to account for possible minor motion artifacts. Then, they were processed with an algorithm based on the Otsu threshold [96] to remove the image background as well as non-brain structures such as the skull. Diffusion tensors were estimated using a least squares method [116] and the image quality was individually checked on the tensor volumes using color by orientation maps. From the tensor volume, the scalar measures and local operators were computed ($\mathcal{N}_{4\text{mm}}^{\text{Gauss}}$, mask size $7 \times 7 \times 3$) and TBSS analysis [125] was performed using FSL 4.1 (FMRIB software library, <http://www.fmrib.ox.ac.uk/fsl> [60]). By using this methodology, FA volumes were non-linearly registered to the MNI 152 standard space (voxel size $1 \times 1 \times 1\text{mm}^3$ [45]). Then, a WM skeleton was created from the thresholded mean FA map ($\text{FA} \geq 0.2$). Finally, all original scalar measures and the ones derived from local operators were projected onto the WM skeleton for statistical comparisons.

Statistical analyses for TBSS were carried out using RANDOMISE, an FSL tool that performs permutations for inference on statistical maps when the null distribution is unknown [92]. This allows to measure the precision and specificity, similar to conventional tests of receiver-operator characteristics, but with increased sensitivity to differences in a specific direction [147]. Corrections for family-wise errors and multiple comparisons with threshold-free cluster enhancement [124] were performed. Pairwise comparisons were made for each combination of different cohorts and for all measures (original measures and the ones proposed in this paper), and the number of voxels for which significant differences ($p < 0.05$) were found among groups was counted separately for each operator and combination of cohorts.

Analysis of robustness

In order to evaluate the performance of the proposed new scalar measures with respect to noise, noise-controlled DTI volumes were employed based on a realistic phantom. Following the approach described in [135], a real dataset was denoised [136] to create a ground truth with 16 gradient directions, $b = 1200 \text{ s/mm}^2$, one baseline volume, reconstructed voxel size $0.9375 \times 0.9375 \times 1.7 \text{ mm}^3$, 128×128 acquisition matrix zero-padded to 256×256 prior to reconstruction, and 81 slices covering the entire brain. Then, the noiseless DWI (D_∞) was interfered with Rician noise of eleven different signal-to-noise ratios ranging in amplitude scale from $\text{SNR} = 3.16$ to $\text{SNR} = 56.23$. The SNR's have been chosen to be uni-distant in (logarithmic) decibel scale with a spacing of 2.5 dB and covering the interval [10 dB, 35 dB]. The noisy DWI signal D_{SNR} read:

$$D_{\text{SNR}} = \sqrt{(D_\infty + \eta(\text{E}/\text{SNR}))^2 + \eta'(\text{E}/\text{SNR})^2}, \quad (3.111)$$

where E and SNR were both expressed in amplitude scale and the expected value E was the mean value of the noiseless DWIs. The functions $\eta(\sigma)$ and $\eta'(\sigma)$ were two Gaussian random variables with zero mean and standard deviation σ . The traditional and novel scalar measures ($\mathcal{N}_{4\text{mm}}^{\text{Gauss}}$, $9 \times 9 \times 5$ voxels) were obtained from the resulting DTI volumes and TBSS was applied, thus obtaining a thresholded FA skeleton (noiseless $\text{FA} \geq 0.2$), over which the evolution in noisy scenarios was analyzed. Quantitative comparisons between operators and SNRs were derived from the normalized root-mean-square error

$$\text{NRMSE}(X_{\text{SNR}}, X_\infty) = \frac{\text{RMSE}(X_{\text{SNR}}, X_\infty)}{\text{SD}(X_\infty)}, \quad (3.112)$$

with $\text{RMSE}(X_{\text{SNR}}, X_\infty)$ the root-mean-square error between the noisy X_{SNR} and the noiseless signal X_∞ , and $\text{SD}(X_\infty)$ the standard deviation of the noiseless signal. The normalization with the standard deviation allows for the optimum comparison between the different tested operators: it does not require ratio variables (in contrast to a normalization with the mean) and is robust against outliers (in contrast to a normalization with the range). In particular the variables FA RAW and AVG on the white matter and SKW require this kind of normalization. Since the measures SNR

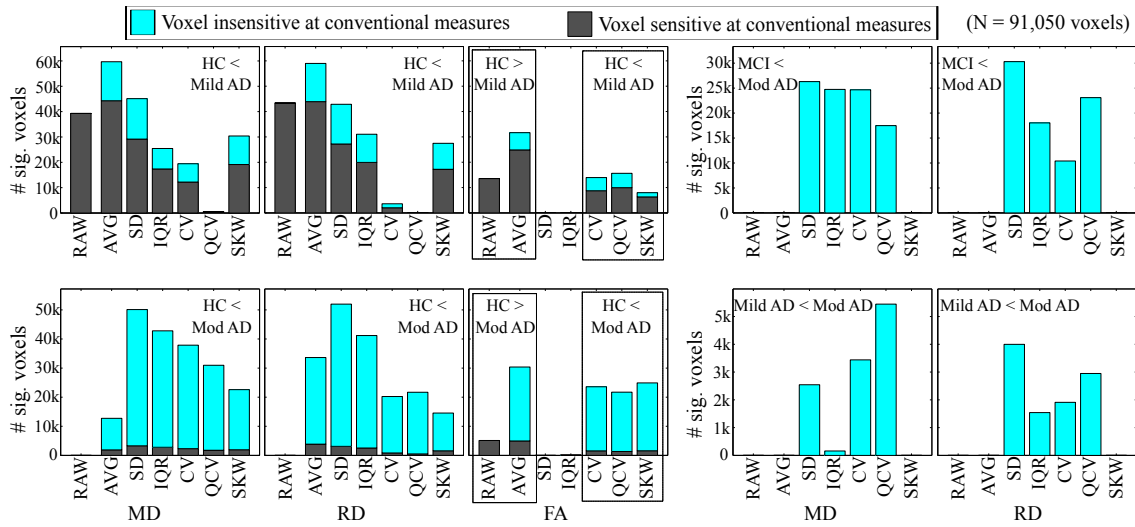


Figure 3.23: Number of significant different TBSS voxels ($N = 91,050, p < 0.05$, corrected for multiple comparisons) between HC *vs.* Mild AD (top left), HC *vs.* Mod AD (bottom left), MCI *vs.* Mod AD (top right) and Mild AD *vs.* Mod AD (bottom right). The subset of voxels which were also identified by conventional measures (RAW of MD, RD or FA) is shaded black.

and RMSE express amplitude ratios, the transformation to dB scale was performed with the formula for root-power quantities.

The analysis of the contamination with gray matter was obtained from all 58 patients of the AD study. A histogram was computed of the minimum amount of white matter in the neighborhoods of the TBSS. The proposed mask $\mathcal{N}_{4\text{mm}}^{\text{Gauss}}$ was compared with three different unweighted $3 \times 3 \times 3$ masks used for the computation of the inter-voxel local diffusion homogeneity [44]: the neighborhood $\mathcal{N}_{27}^{\text{Vox}}$ contained all 27 voxels, while the other contained only voxels sharing an edge ($\mathcal{N}_{19}^{\text{Vox}}$) or side ($\mathcal{N}_7^{\text{Vox}}$) with the center voxel.

3.6.3 Results

Analysis of diagnostic performance

No significant differences were found between HC *vs.* MCI or between MCI *vs.* Mild AD. Except for FA RAW and AVG, parameters between other cohorts increased with progressing dementia: HC $<$ Mild AD $<$ Mod AD and MCI $<$ Mod AD. None of the parameters contained significantly increased and decreased areas at the same moment. The traditional measures (RAW or AVG) found significant differences only

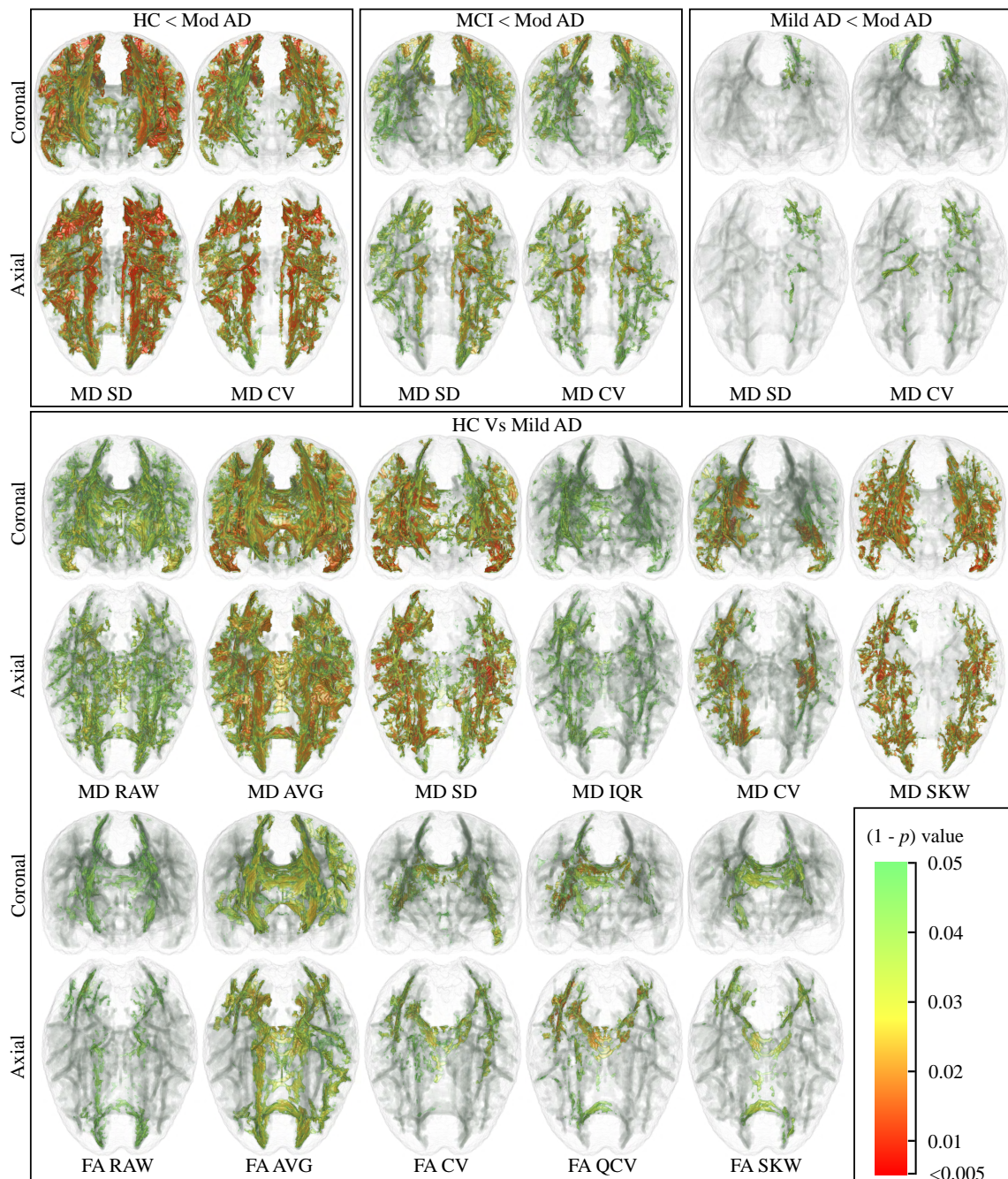


Figure 3.24: Up: spatial distribution of significant differences of MD SD and CV. Groups are HC < Mod-AD, MCI < Mod AD and Mild AD < Mod AD where RAW MD was not discriminative ($p < 0.05$). Down: Differences for HC vs. Mild AD on MD and FA.

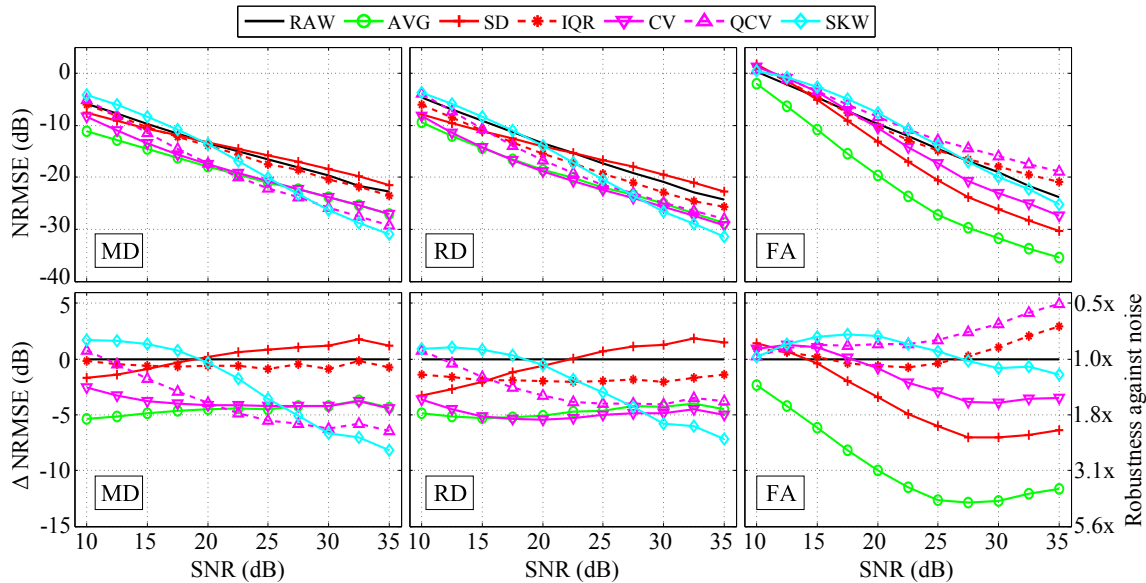


Figure 3.25: Noise analysis with NRMSE *vs.* eleven SNRs $\in [10 \text{ dB}, 35 \text{ dB}]$. 1. row: NRMSE(dB) of MD, RD and FA. 2. row: Δ NRMSE as the difference of NRMSE(dB) of the inter-voxel- to the NRMSE(dB) of the single-voxel operator RAW.

between healthy patients and those with AD, while the inter-voxel texture operators additionally located changes at $\text{MCI} < \text{Mod AD}$ and between the two AD cohorts (Mild AD $<$ Mod AD), Fig. 3.23.

The application of the operators to MD and RD followed a widely similar pattern, both, in regard to the number and in regard to their spatial distribution. With regard to MD, SD and CV discriminated on four pairs, while the other operators only at three (IQR and QCV) or two pairs of groups (AVG and SKW). MD SD and CV detected similar locations, however MD CV revealed stronger indications of impairments between Mild AD and Mod AD on the sensory cortex and parietal lobe, Fig. 3.24. The application of higher order moments (SD, CV, SKW) on FA did not improve the diagnostic performance of FA AVG.

Analysis of robustness

Most of the local operators had higher robustness against noise than the single-voxel RAW operator, Fig. 3.25. The noise characteristics obtained on MD and RD were very similar. Applied to MD or RD, AVG increased the robustness against noise constantly by a factor of 1.8, while FA AVG increased the robustness depending on

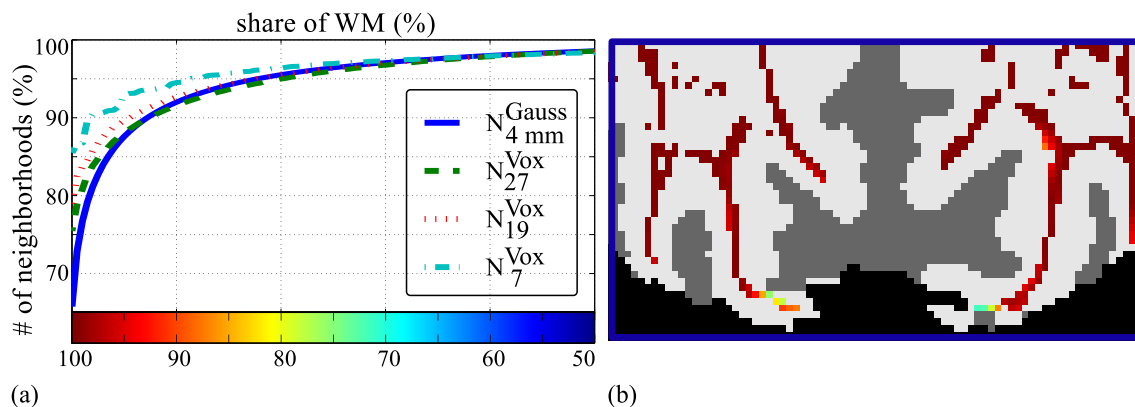


Figure 3.26: a) Histogram of neighborhoods on the WM-skeleton that contain a minimum amount of WM for masks $\mathcal{N}_{4\text{mm}}^{\text{Gauss}}$, $\mathcal{N}_{27}^{\text{Vox}}$, $\mathcal{N}_{19}^{\text{Vox}}$ and $\mathcal{N}_7^{\text{Vox}}$, b) spatial distribution of the WM share of $\mathcal{N}_{4\text{mm}}^{\text{Gauss}}$ (color coded from 50% – 100%).

the SNR by up to factor of 4, compared to RAW. Also the local texture operators of MD and RD were more robust than RAW, with the exception of SD for high SNRs and SKW for low SNRs. The robustness against noise of MD/RD CV, QCV and for high SNRs of SKW increased by a factor 1.8 to 2.2, exceeding also the robustness of MD/RD AVG. If applied to FA, SD and CV were only robust for high SNRs (2.2 and respectively 1.6 times of RAW), while IQR, QCV and SKW were rather sensitive to noise.

The comparison of $\mathcal{N}_{4\text{mm}}^{\text{Gauss}}$ with unweighted $3 \times 3 \times 3$ neighborhoods $\mathcal{N}_{27}^{\text{Vox}}$, $\mathcal{N}_{19}^{\text{Vox}}$ and $\mathcal{N}_7^{\text{Vox}}$ is shown in Fig. 3.26. Although the spatial dimension of $\mathcal{N}_{4\text{mm}}^{\text{Gauss}}$ exceeded the one of the unweighted neighborhoods, its contamination with gray matter was still low: approximately 92% of all neighborhoods were at least to 90% in WM. Furthermore, $\mathcal{N}_{4\text{mm}}^{\text{Gauss}}$ contained more neighborhoods with a minimum white matter share of 93% ($\mathcal{N}_{27}^{\text{Vox}}$), 80% ($\mathcal{N}_{19}^{\text{Vox}}$) and 65% ($\mathcal{N}_7^{\text{Vox}}$), respectively.

3.6.4 Discussion

The experimental work performed here focused on the analysis of two important aspects: the ability to discriminate between pathological conditions in a group study, and the evolution with varying SNR. With regard to the first one, results showed that some of the proposed local inter-voxel operators highly increased the ability to differentiate between groups. Concerning the second one, most parameters obtained

high robustness against noise, some texture operators even exceeded the robustness of AVG.

A DTI data set with multiple stages of Alzheimer’s disease was selected as an experimental benchmark because it allowed to quantify the potential gain of the new operators. Indeed, new differences between groups arose when employing the proposed approach, which is a strong advantage over traditional measures.

In particular, the texture parameters SD, CV, IQR and QCV, if applied on MD or RD, exceeded the performance of RAW and even AVG. For instance CV and QCV obtained both, higher robustness to noise and higher discriminative potential than AVG. When considering noise and discriminative analysis together, local texture parameters of MD and RD were more adequate for the conducted AD-group studies than those based on FA. AVG was the only non-texture and standard DTI-operator among the proposed ones, since weighted averaging is commonly employed in voxel-based morphometry [4] and TBSS [125]; it obtained high robustness to noise, but was, unlike other texture parameters, unable to reveal differences between MCI *vs.* Mod AD or Mild AD *vs.* Mod AD.

In general, also alternative statistical analyses could be performed, such as the general voxel based (VBA) or atlas based analysis (ABA), which do not require skeletonization of the WM [95]. However, TBSS analysis was used in this application because of two reasons. First, as TBSS is a widely employed DTI analysis tool [144], it facilitates the interpretation and comparison of the results among other approaches. Second, since TBSS centers the neighborhoods on the WM skeleton, it minimizes any contamination with gray matter.

Still, the mask size must be selected carefully according to the spatial resolution. If the mask exceeds noticeably the distance from the WM skeleton to gray matter voxels, local features become mainly dependent on changes in local morphometry, which decreases the discriminative power particularly at the boundaries of the WM. In terms of contamination with gray matter, $\mathcal{N}_{4\text{mm}}^{\text{Gauss}}$ contained similar characteristics than the unweighted reference masks, while being advantageous in terms of sample size and isotropy: in contrast to $\mathcal{N}_{4\text{mm}}^{\text{Gauss}}$, the reference masks $\mathcal{N}_{27}^{\text{Vox}}$, $\mathcal{N}_{19}^{\text{Vox}}$ and $\mathcal{N}_7^{\text{Vox}}$ are anisotropic ($3 \times 3 \times 9\text{mm}^3$) and thus favor longitudinal fiber tracts over transversal or sagittal ones.

The interpretation of the results may be difficult compared to traditional measures, which is a common issue of inter-voxel operators [44]. Differences in traditional

scalar measures, such as FA, have been often related to physiological changes in the WM tissue (demyelination, lower packing density or different membrane permeability, among others) [68]. However, changes in FA, MD or RD can be motivated by very different mechanisms within the tissue, which makes bold interpretations of changes in the WM integrity, although very common, possibly flawed [61]. The use of the proposed local operators, on the other hand, can open a door to new viewpoints for the analysis of pathologies. For instance MD CV uncovered a progressing impairment from mild to moderate AD of brain areas, which are commonly related to sensations (sensory cortex), perception, spelling and arithmetic (parietal lobe). These impairments remained hidden on standard parameters (RAW and AVG).

The application of inter-voxel operators is not committed to DTI, but could be applied to any scalar measure. In particular, the application to Q-Ball scalar measures from high angular resolution diffusion imaging might be investigated, for instance the generalized anisotropy [97], generalized fractional anisotropy [137] or fractional multi-fiber index [37]. Studies with with higher spatial resolution than the one employed here could achieve improvements regarding the robustness and localization of pathological areas. The Matlab code with a sample script, that computes the local operators, is available at members.imaglabs.org/felix.thomsen/LocalOperatorsMRI/Matlab.zip.

3.6.5 Conclusion

In this chapter new image processing methods were presented for the identification and characterization of pathological changes in the white matter of the brain based on DTI. Instead of deriving new scalar measures directly from DWI, existing DTI scalar measures such as FA, MD and RD have been further processed with rotational invariant inter-voxel texture operators. Each combination of existing scalar measures and inter-voxel operators provided a novel measure with distinct and new properties, which was in many cases more suitable than the original single-voxel measure for particular discrimination problems of DTI studies. Compound sensitivity and specificity of the inter-voxel operators was compared with the one of traditional measures on a group study of Alzheimer's disease. Additionally, noise characteristics were measured with a synthetic DWI phantom and the overlap of the local operators with gray matter was analyzed.

Texture parameters based on MD and RD yielded the highest discriminative power and robustness against noise and were able to identify formerly undetected pathologies even between previously insignificant pairs of groups (MCI or Mild AD *vs.* Mod AD). Thus, the results indicate that the methods are a promising extension in DTI studies. Future work might investigate the application of the proposed methods on group studies of different alterations of the brain (multiple sclerosis, schizophrenia, etc.) to improve the detection and localization of these pathologies.

Chapter 4

Structural Insight

For the computation of structural parameters from CT volumes, the software Structural Insight has been developed. Parts of this chapter have been presented in 2016 at the Argentine Congress of Informatics and Health in Buenos Aires [131]. Furthermore, the software has been used for a number of publications over the last years [12, 13, 20, 41, 102, 130, 132]. This third mayor version of the software resembles most features of its previous version [46, 71] but with important additional functionality, that will be described here in detail. Figure 4.1 shows the three mayor versions and their main developers. Since 2014 the software is maintained by Timo Damm, who continued with the recently developed version 3. Version 1 had mainly the purpose to provide the research environment for the scientific work of Wolfram Timm, version 2 was already a software that provided sufficient comfort to be used by external users. However some mayor design issues and not solvable bugs, including compiling errors, induced to develop the version 3. Mainly all functional concepts from version 2 entered in version 3, which follows internally a more categorical modular programming style, allowing for easier extension. The functional concept of Structural Insight is to provide all necessary methods and steps for the computa-

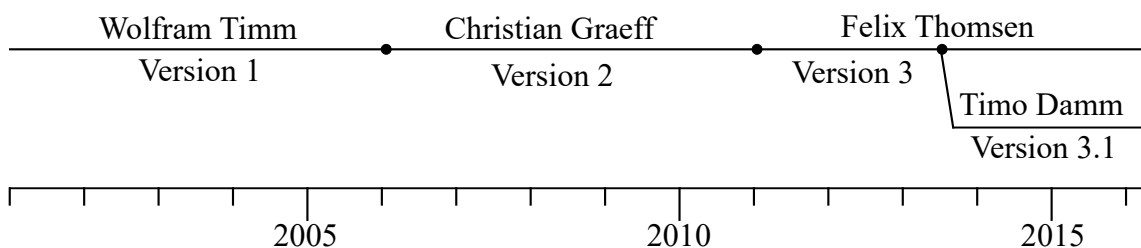


Figure 4.1: Timeline of Structural Insight containing versions and main developers.

tion of structural parameters from raw CT volumes of any resolution and modality. This includes the mayor steps quality assurance, calibration, segmentation, registration and analysis. The software is written in C++ using the libraries Insight Segmentation & Registration Toolkit ITK (www.itk.org) and Qt (www.qt.io).

4.1 Purpose and workflow

The software Structural Insight provides a all-in-one software to parse, visualize and analyze CT data as generated by commercial clinical or pre-clinical CT scanners. Other software packages exist, that contain similar functionality, some are listed below:

- **VolView** (<http://www.kitware.com/opensource/volview.html>) is a software, specialized to the visualization of 3D data rather than to the computation of structural parameters. It offers a wide range functionality, such as volume rendering or multiple projections on the same screen and is based on ITK
- **Slicer** (<https://www.slicer.org>) is a software with a similar idea than Structural Insight, thus provides functions for the visualization and analysis of 3D medical data. It is as well based on ITK and provides besides the processing of CT volumes also a large number of functions for the processing of MRI volumes. It is similar to ImageJ based on Add-ons, where the programming of own Add-ons is faster and better managed than in the case of ImageJ, however the data-base of the Add-ons contains unfortunately a large number of buggy add-ons, or of add-ons, which require a certain size of RAM or a specific GPU. In contrast to Structural Insight or BoneJ, the most standard structural CT parameters are not yet implemented.
- **ImageJ** (<http://imagej.net>) is a multi-purpose image- and volume-editing software, which is not only designed for medical imaging. It can read a large number of 2D and 3D images, such as e.g. DICOM volume and provides add-ons for distinct types of analysis and visualization. The visualization is however not as comfortable as in the case of VolView, Slicer or Structural Insight. ImageJ is not specific for the analysis of CT volumes and thus does not provide the entire required functionality and productivity.

- **BoneJ** (<http://bonej.org>) is an add-on of ImageJ and provides a number of routines for the computation of structural parameters. It is designed for either for researchers than for practical radiologists. It has some restrictions, such it requires a number of additional scripts for the batch computation of large scale studies and does not allow to define multiple VOIs.

Besides these open-source softwares, most CT manufacturer provide their own software, where generally only HRpQCT manufacturers (for instance Scanco or Bruker-SkyScan) provide the micro-structural parameters, but all provide a certain volume viewer. Furthermore, certain radiology institutes developed their own in-house software (for instance the institute of Medical Physics at the Friedrich-Alexander-University Erlangen-Nürnberg <http://www.imp.uni-erlangen.de/>). The difference of Structural Insight in relation to the mentioned software packages is its specificity for the application of HRQCT studies and the simplicity such that practical radiologists can use the program without long training sessions. Since the used version of Structural Insight was written by the author of the thesis, specific improvements of standard techniques were implemented and the functions were not treated as “black-boxed” like in many commercial software packages, where the source-code is not provided. Thus, comparisons and specific improvements of structural parameters could be optimally analyzed. The minimum workflow for processing DICOM volumes with Structural Insight is as follows:

- **Quality assurance:** The DICOM volumes generated with the commercial scanners (Siemens, Phillips, Scanco) are parsed into a common internal format. This is important, because the DICOM format is vaguely defined, many manufacturer-specific differences exist and the very same parameter can be expressed in different fields in the meta data. Then, the parsed meta data and the volume is displayed for the radiologist and stored in a normalized DICOM format, see also <https://www.youtube.com/watch?v=Bpsiyd1uZwA>.
- **Visualization:** Structural Insight provides functions to visualize the 3D data, that is important to extend the a-priori quality assurance but as well for a a-posteriori analysis of outliers and is essential for the calibration, segmentation and registration steps, see <https://www.youtube.com/watch?v=0rGGtb453iI>.

- **Calibration:** The DICOM volumes are calibrated from HU to density units which allows a quantitative analysis of the gray values, see <https://www.youtube.com/watch?v=uIhyBNQn7Dc>.
- **Segmentation or registration:** The VOI is defined, which allows to compute the structural parameters in the defined anatomical region. If a segmentation of the VOI exists from a previous scan, the old VOI can be automatically registered to the new scan. See the following videos show the handling of these functions: geometric segmentation <https://www.youtube.com/watch?v=4noMgi2ho2Y>, template segmentation <https://www.youtube.com/watch?v=9hp7ZLgEpRA> and registration <https://www.youtube.com/watch?v=JTz2JL7VmJ0>.
- **Computation of structural parameters:** Different standard structural parameters are computed and their result is stored in a XML- text- or Excel-file for the post-hoc analysis using statistical software like JMP, WEKA or Excel, see <https://www.youtube.com/watch?v=pwVAeEp5HfY>.

Besides these functions, Structural Insight provides different volume processing methods.

4.2 General classes and features

The program divides its functionality in specific classes, Fig. 4.2, the central class is the `InsightVolume`, which contains the image and the meta data. This meta data is visualized by the class `MetadataViewer`, while the image data is shown by the `ImageViewer` class, that contains three instances of `ImageFrame`. Changing of projection settings can be performed by mouse-operations on the screen (`ImageFrame`) or with the class `ViewerSettings`. The calibration is performed with the class `Calibration` and the user interface is provided by `CalibrationWidget`. The actual calibration is not only stored temporarily but also written to the hard disk, thus allowing to apply the same calibration to different scans, even when the calibration was performed in a older session. The characteristics of the calibration phantom are stored in a text file `PhantomSettings`, which allows to extend the applicable calibration phantoms ad-hoc. The class `SegmentationWidget` provides

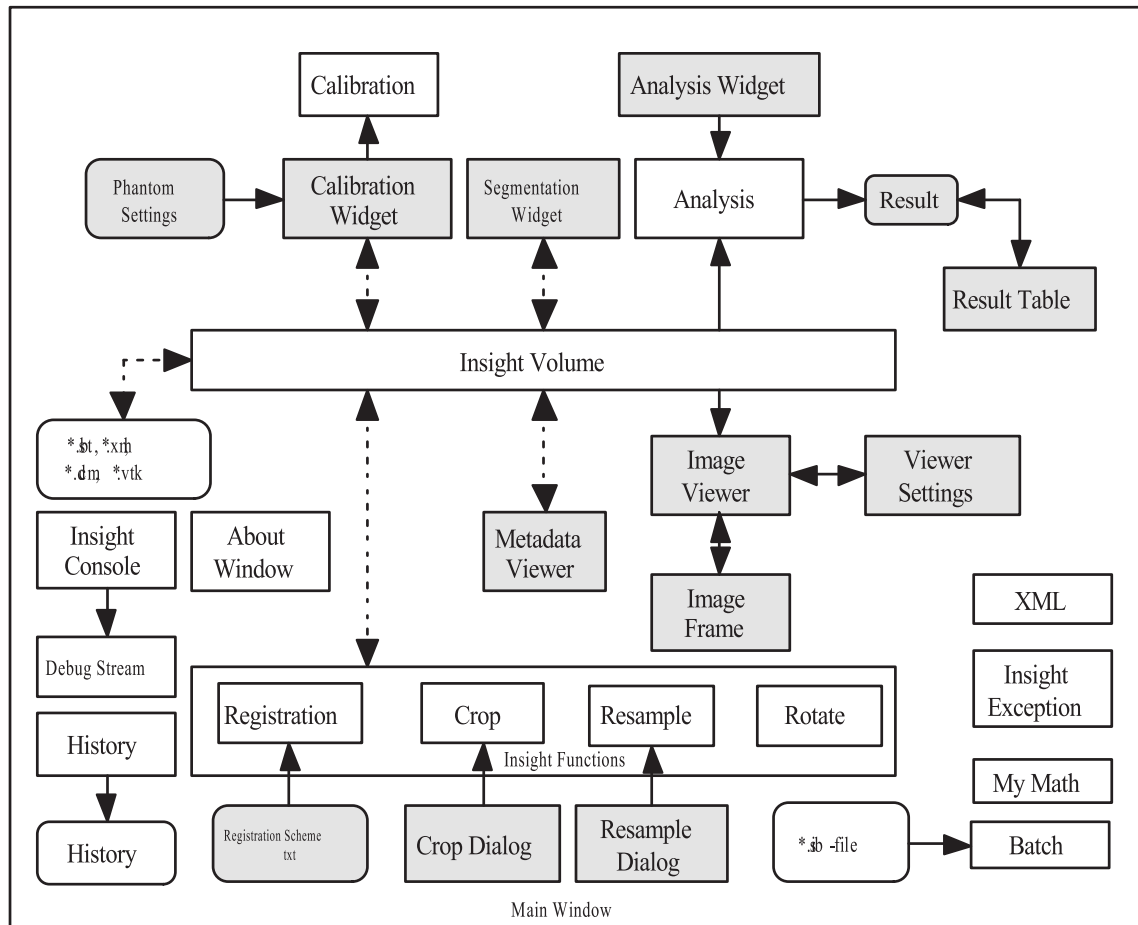


Figure 4.2: A simplified diagram of Structural Insight 3.0, showing the most important classes and their internal relation. User interfaces are shaded in gray and round boxes are data files.

functionality for the segmentation, following internal a similar principle as `CalibrationWidget`. The class `Analysis` performs the computation of the structural parameters, the user can select the parameters on `AnalysisWidget`. The results, an xml-table, can be visualized and stored with the class `ResultTable`. Additional classes, like the `InsightConsole`, `History` and `AboutWindow` are designed to track and organize the work. The `Batch` class allows to perform overnight-processing of large datasets. Volume processing methods, like resampling, crop, rotation and registration are provided by the class `InsightFunctions`, each with its own user interface class. Figure 4.2 shows only the most important classes, the program contains however further classes, such as a histogram, a thread-class, a number of classes

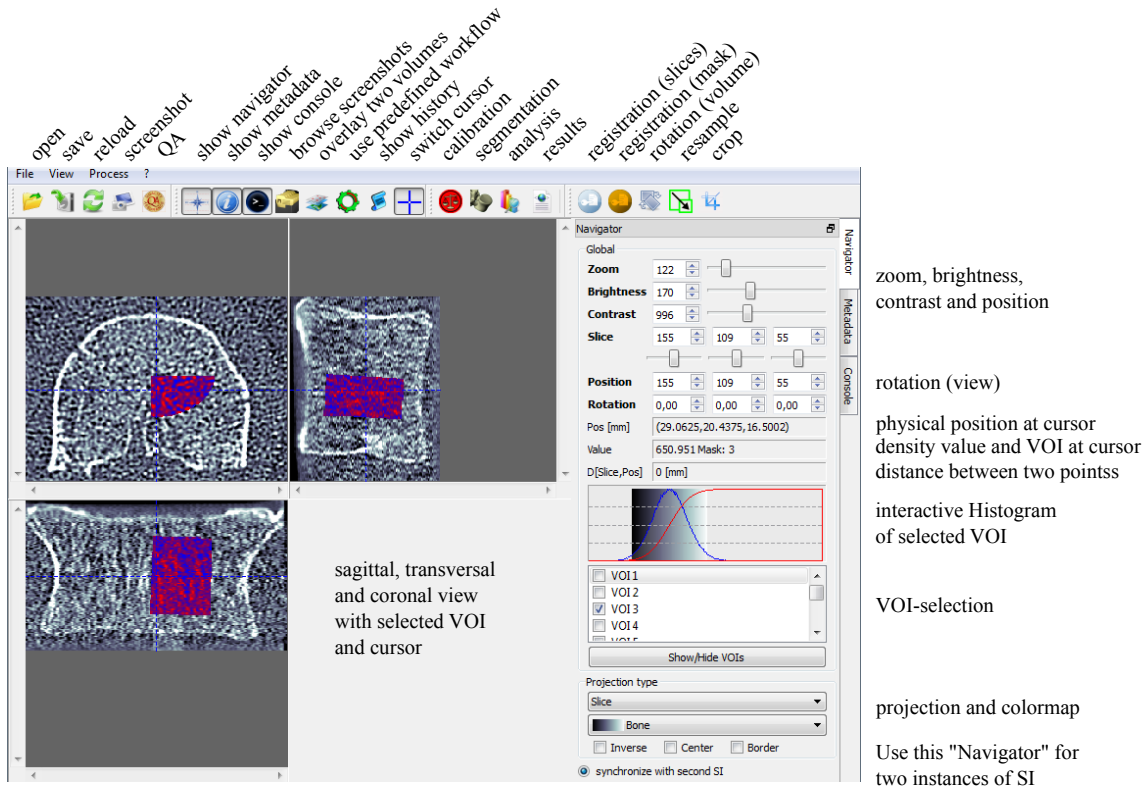


Figure 4.3: The main screen of Structural Insight after loading a pre-segmented volume. Functions can be accessed from the file menu or the icons.

for the template segmentation. It follows a brief summary of specific methods and features.

4.2.1 Start screen

The start screen contains the graphical user interface, Fig. 4.3, and allows to access all specific functions. The class `ImageViewer` is placed in the center and dockable widgets are placed on the left and right of it. On the right of the screen, the class `ViewerSettings` with the integrated histogram is located. By using tabs, the user can switch to view the meta data or the console, containing the user's last operations. Further widgets can be accessed with the file menu or by clicking on the icons. The icon-bar can be adjusted for user's preferences.

4.2.2 File formats

The class `InsightVolume` is the container of the CT data, while the corresponding meta data is stored in the class `Metadata`. Both contain functions to read and write the data. It reads and writes Digital Imaging and Communications in Medicine (DICOM), Guys Image Processing Lab (gipl) and gipl gun zip files (gipl.gz), Visualization Toolkit (vtk) files and the proprietary Byte stack (bst) and Extensible Markup Language (xml) files. The bst format was introduced in Structural Insight 1.0, and the xml format with Structural Insight 2.0 (xml) and the meta data was extended in version 3.0. Both, xml and bst store the voxel information as a float-bitmap without further compression. The header of the bst files contains only few information (dimension, resolution, birth date) while the xml files contain the most important information from the DICOM header and information regarding the calibration and segmentation. If a volume was segmented, a second file is generated, which allows to assign up to 255 distinct VOIs per volume (1 byte/voxel). Storage of the segmentation is only possible in .bst and .xml format. The slices can also be exported in portable network graphics format (png), lacking however the header information. Screenshots can be stored as bitmap (bmp), png, portable pixmap (ppm), X PixMap (xpm) or the binary format X BitMap (xbm), using a dithering approach. The program allows also to load only 2D projections, the maximum- and mean-projection is directly computed when the volume is opened, or to open the meta data without the corresponding volumes, which is particularly useful if the volume is very big and just details of the meta data need to be assessed.

4.2.3 Visualization

The class `ImageViewer` shows the volume data. Since Structural Insight shows concurrently 3 projections, the low-level image processing is located in the class `ImageFrame` containing these projections. The class manages mainly the interaction between the three instances of `ImageFrame` and between other classes. The `ImageFrame` class contains the low-level image processing routines to perform a set of different projections: The standard slice projection, a mean, a maximum, a minimum, a standard deviation and a standard deviation by range projection, furthermore a depth-map projection and a volume rendering with ray-casting, see Fig. 2.2. These projection exist as global (full) and local variants, starting either from the first

slice or from a particular point in the volume, and they are applicable in every direction, rather to be only aligned to the x-y- and z-axis. The class `ViewerSettings` contains all fields to adapt the projection settings, some of its functions are also accessible from `ImageFrame`. The colormap and the opacity settings for the volume rendering manipulated here. It also contains the list of VOIs and a histogram of the active VOIs. The `MetadataViewer` is similar to `ViewerSettings` and shows the entire meta data of the `InsightVolume`. It allows to change particular data, for instance the patient's or study name.

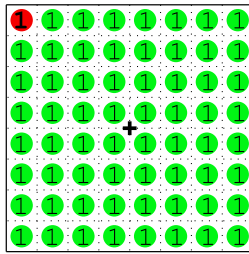
4.2.4 General volume processing functions

The class `InsightFunctions` contains some image processing functions: crop, re-sample, rotate, blur, invert, morphological filtering including a median filter and energy minimization with a Monte-Carlo model. Two other important functions are implemented in the class `Registration`, which applies a non-deformable registration between two scans of the same vertebra, the rotation and translation matrix can then either be applied to the volume data, meaning that the density voxels of are processed (rotated, translated and resampled) or to the mask data, meaning that the VOIs are redefined to match the VOIs of the destiny volume. This functions were introduced in Structural Insight 3.0 and provide an important tool if the study data contains more than one scan per specimen. In this case, the first segmentation is performed with the standard segmentation classes, while the further ones are automatically registered to the first one, allowing the most accurate definition of all scans. The registration of the voxels can be used to map the further scans to the atlas of the first which allows for instance to derive an average or median volume serving as a denoised or ground truth representation of repeated scans. The result of the registration can be controlled with a checkerboard image, which overlays the registered and the destination volume. Specific settings of the registration are loaded from a text file which can be adjusted by the user.

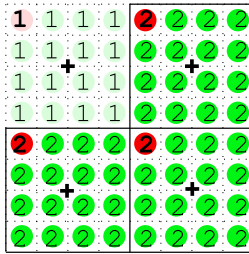
4.2.5 Threads

In particular computations related with the visualization are very costly, for instance the ray-casting operation. After each change of particular settings, the entire volume must be recalculated. This can take tens of seconds of time and thus disallowed

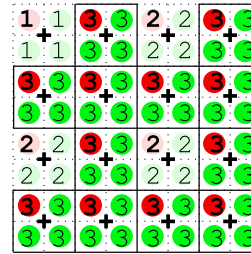
Method 1:



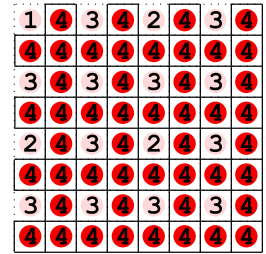
I: read: 1, write: 64



II: read: 3, write: 48

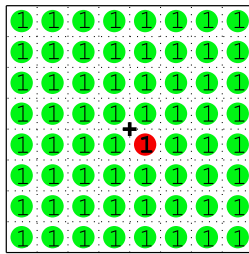


III: read: 12, write: 48

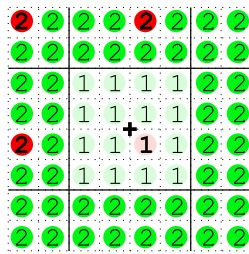


IV: read: 48, write: 48

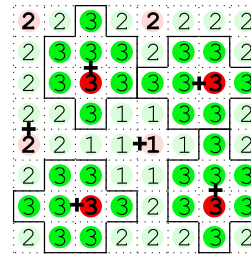
Method 2:



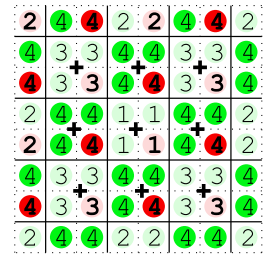
I: read: 1, write: 64



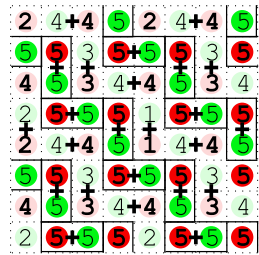
II: read: 3, write: 48



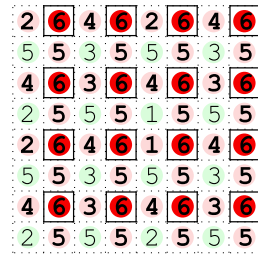
IIb: read: 4, write: 32



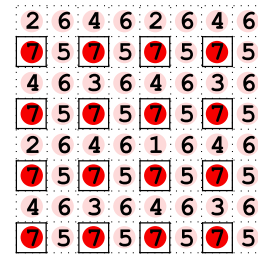
III: read: 8, write: 32



IIIb: read: 16, write: 32



IIIc: read: 16, write: 16



IV: read: 16, write: 16

Figure 4.4: Two different sample schemes of the threaded computation of projections when the read operation is very time consuming. Red circles indicate a read access and green circles a write access, labels indicate the iteration of the last read or write access. Both methods are scalable to every initial box-size, but the second method generates a better accordance to the centers (imprinted crosses) and reduces the number of read-accesses in the last iterations. Steps I, II, III and IV are identical on both methods except for rotation and translation.

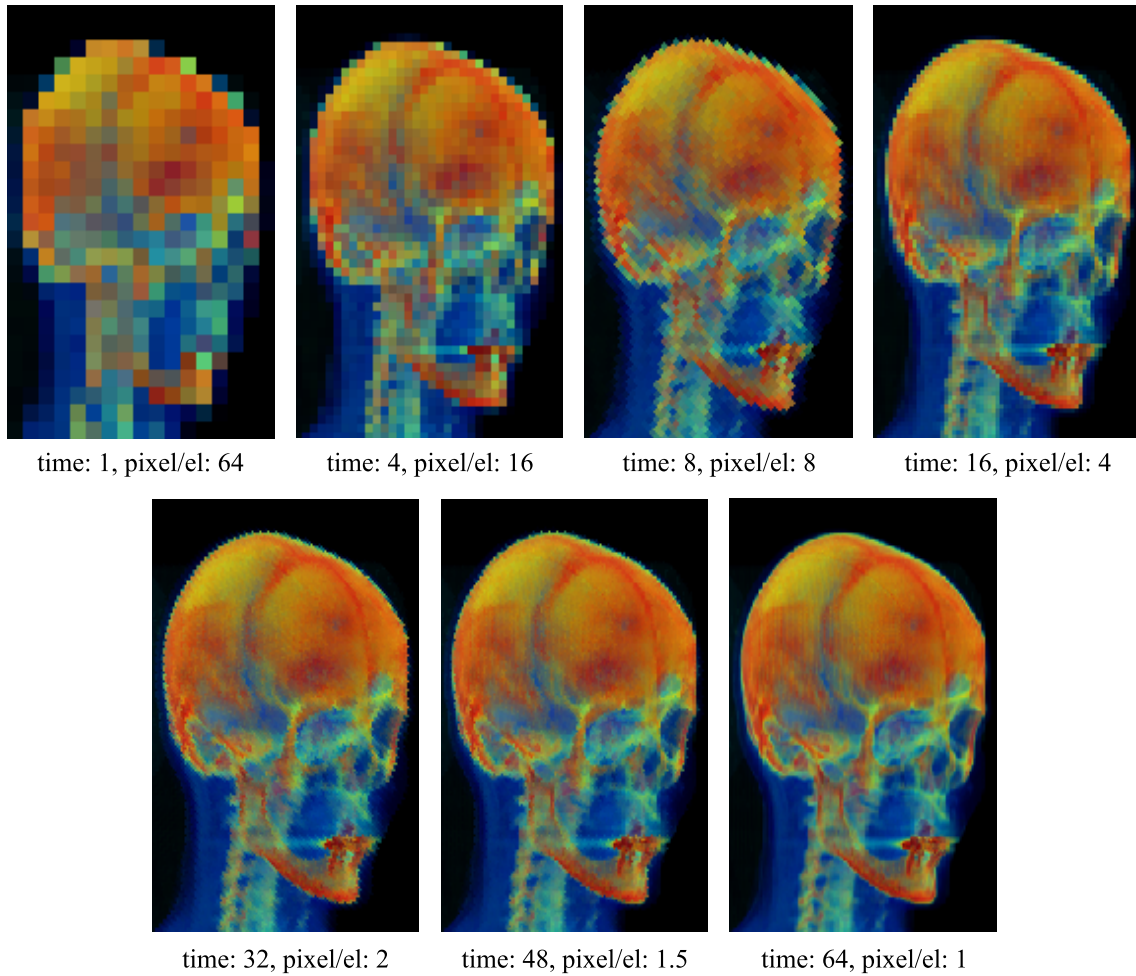


Figure 4.5: Example of threaded rendering with method 2. This allows the user to abort the rendering, before all pixels are processed.

the user to apply a try-and-error approach for seeking the optimum visualization parameters. To avoid this problem, a threaded mechanism was implemented, allowing to interrupt the current visualization and to show preliminary downsampled renderings before the final resolution is available. The rendering is independently threaded starting with rendering blocks of 32×32 pixels, then 16×16 pixels and so forth until reaching the final screen resolution, Fig. 4.4 shows the final steps for blocks smaller or equal 8×8 pixels. This does not restrict the total execution time and allows for an entirely smooth scrolling or change of projection settings since the threaded programming allows to interrupt the rendering as soon as the projection settings were updated, Fig. 4.5. Another application of this threaded mechanism was applied to the histogram. The histogram is mostly not critical for the user's

decisions and thus should neither freeze the program. Here, the same mechanism applies as shown in Fig. 4.4 with the difference that no write-operations are needed, hence method 1 and method 2 are practically equivalent for the application of the histogram. A further thread is implemented for a live-preview of threshold-free voxel-based structural parameters (BMD, TV and standard deviation of the gray values) in the class `SegmentationWidget`.

4.2.6 Further methods to increase the efficiency

The typical workflow consists of the steps quality assurance, calibration, segmentation and computation of structural parameters. While in version 2, the user had to comply this procedure for every scan, Structural Insight 3.0 allows (1) to store any time the intermediate results, (2) to perform certain steps blindly with a batch procedure and (3) to define different workflows.

Different workflows can be selected from a drop-down menu, such as those including a resampling, rotation or registration. This drop-down menu is loaded from an external text file and can be extended with a text editor. Each entry in the list of operations opens the required tabs and closes the not needed ones, two mechanisms are implemented, a force-mechanism automatically switches to the next step after the current operation was executed while the wait-mechanism requires the user input to do so. The workflow is designed like an audio player, containing a stop, a play or pause and a next item, allowing to repeat or to skip the actual step.

Different types of batches are implemented. First a file containing operations and file names can be processed, if the operations don't require user interaction which can be opened from the shell or after opening the program. Second, the computation of structural parameters can be processed as a batch, thereby selecting the list of segmented volume from the `AnalysisWidget`. Third, the described workflow mechanism is a batch processing, that always halts when user interaction is required.

Important classes use a text file to store typical combinations of settings, for instance a geometric VOI, consisting of a prototype shape, an extension in x-, y- and z-direction and a division into N sub-VOIs can be stored as one entity and in a later session again used, changed or deleted.

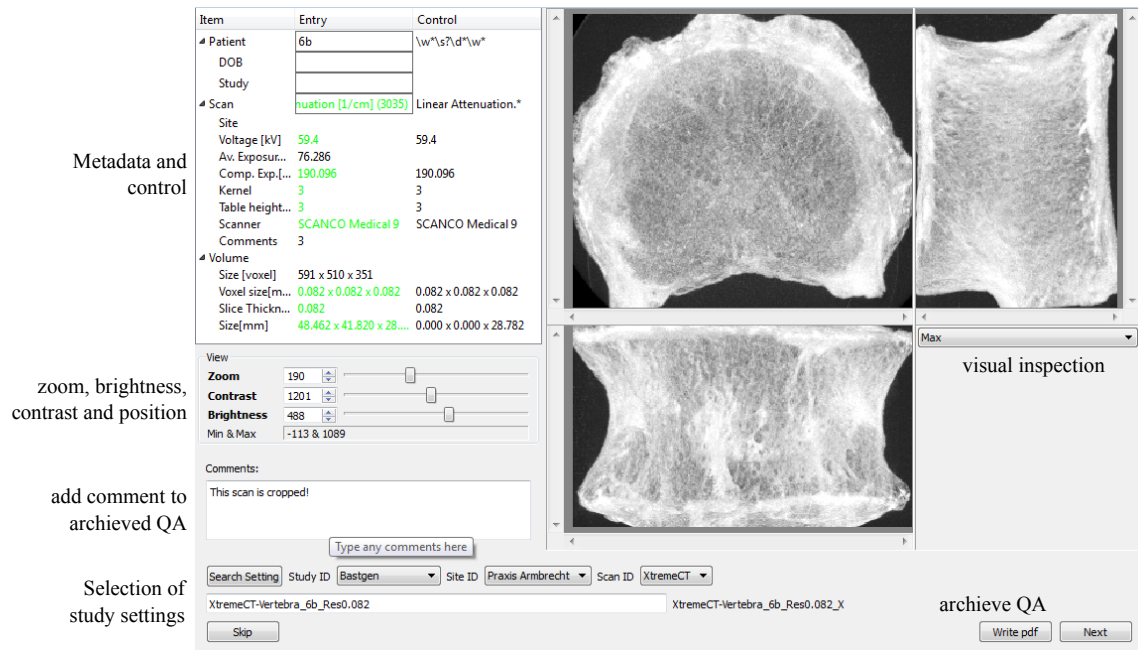


Figure 4.6: Quality assurance allows to check for failures in the field of view, to detect image artifacts and to check the meta data.

4.3 Core functions

The next subsections describe the minimum core steps that are required to compute structural parameters from an input DICOM file.

Quality assurance

Generally when starting to work with image data belonging to a new study, it is necessary to check if the meta- and image-data meet the desired requirements. This can be either done by opening every scan separately and checking all of its properties manually or with the quality assurance function (class `CTQA`). The class `CTQA`, Fig. 4.6, contains a simplified variant of `ImageViewer`, and `ViewerSettings`, designed to handle 2D images instead of 3D volumes, and an extended version of `MetadataViewer`, containing not only the meta data but also the control input and a color coding indicating a differences between the control and the real input. The volumes are not opened in 3D mode but in a 2D mode, thereby generating the transversal, sagittal and coronal maximum- and mean- projection. This allows to reach a higher flow-rate and is generally sufficient to visualize systematic image

defects. The quality of the image data is checked visually by the user while the meta data is tested against the standard settings of each study, using again regular expressions.

After selecting the input and output folder, all unsorted DICOM files, which are 2D slices, are opened and merged to entire 3D volumes. The eventually cryptic file name of the DICOM files is thereby replaced by using regular expressions based on the meta data of the files. The regular expressions are stored in an .xml file which can be adjusted after compilation with any text editor. The quality assurance class generates new folders for the output DICOM data of each scan. It contains also the option to create a .pdf file of each generated 3D volume containing (1) a scout view, (2) the most important meta data which is highlighted when violating the regular expressions, and (3) free space for comments and (4) a space for a signature of the person who included or excluded the current patient's scan from the study. This specialized class allows to seek all DICOM files in a complete file-system, to copy them to a specific folder structure, rename and filter them. In addition, the definition of the control input allows to perform the quality assurance by external personnel which helps to provide a quick feedback to the radiologists for eventual changes of their procedure.

4.3.1 Calibration

The class `Calibration`, Fig. 4.7, contains the functions to apply a calibration of the CT volume. After mapping the Hounsfield units (HU) of the scans to density values mg/cm^3 , the CT scans become quantitative CT scans (QCT). From these, it is possible to derive density based structural parameters (BMD, TMD). To apply a calibration, in general two reconstructions of the scan are needed. The large field of view (FOV) contains in particular the calibration phantom, which is placed under the patient or specimen, while the small FOV contains the specimen in the desired resolution. The calibration phantom contains at least 2 rods of different known densities of a reference material. The average HU inside these rods are taken and the linear mapping between HU and mg/cm^3 is derived from a linear fit. The derived mapping between HU and mg/cm^3 is then applied to the small FOV reconstruction. The calibration form contains all necessary functions to perform these operations manually, once the mapping is defined from the large FOV, the parameters are stored in a text file, the corresponding small FOV is opened and calibrated.

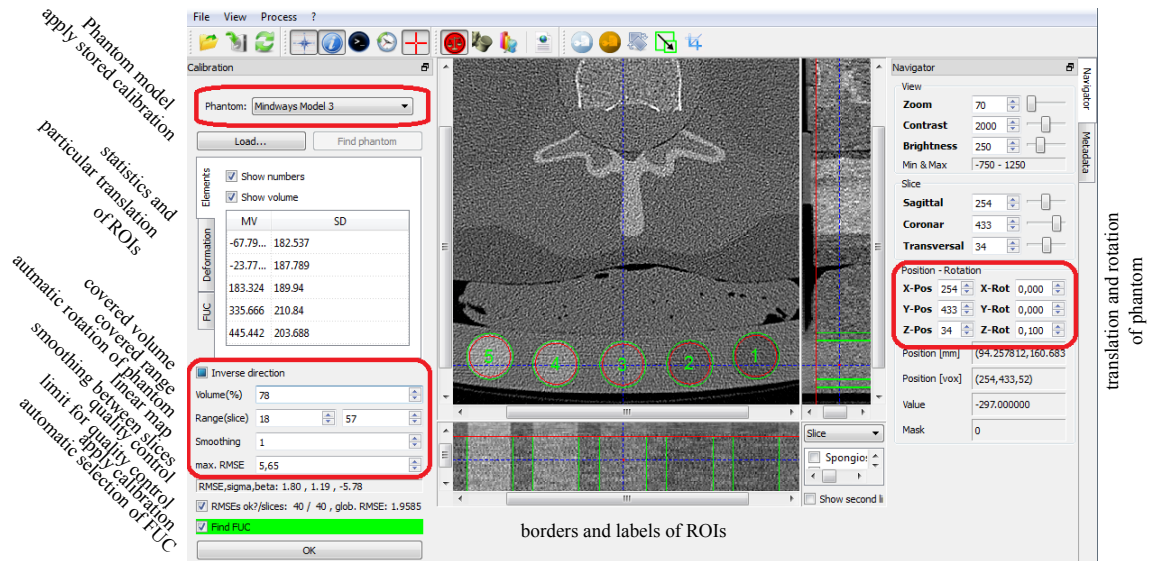


Figure 4.7: Calibration from Hounsfield to density values. The phantom type (left top), the position and rotation (right) and the processing of the HU-values (left bottom) can be adjusted.

The class contains functions to segment all calibration rods. Every scanner and every calibration phantom has individual settings, which change over time, for that purpose the individual calibration phantom and a field uniform correction (FUC) for the particular date and scanner can be derived from a quality assurance scan, containing a calibration phantom and a density phantom in the place of the patient. These settings can then be selected for the particular patient scan. Additionally the user can select between an individual calibration per slice or a global calibration and it is possible to extend the procedure for further calibration phantoms, whose characteristics are loaded from a text file.

The actual calibration is not only stored in the RAM but also in the file-system. A calibration will be applied to the file which is next opened after creating a calibration or an older calibration can be applied by opening the stored calibration file. Structural Insight allows only to apply one calibration of the volume to avoid the iterative application of the calibration.

4.3.2 Segmentation

The segmentation of the VOIs is performed with functions of the `SegmentationWidget` and `TemplateSegWidget`. The geometric segmentation, Fig. 4.8, allows to

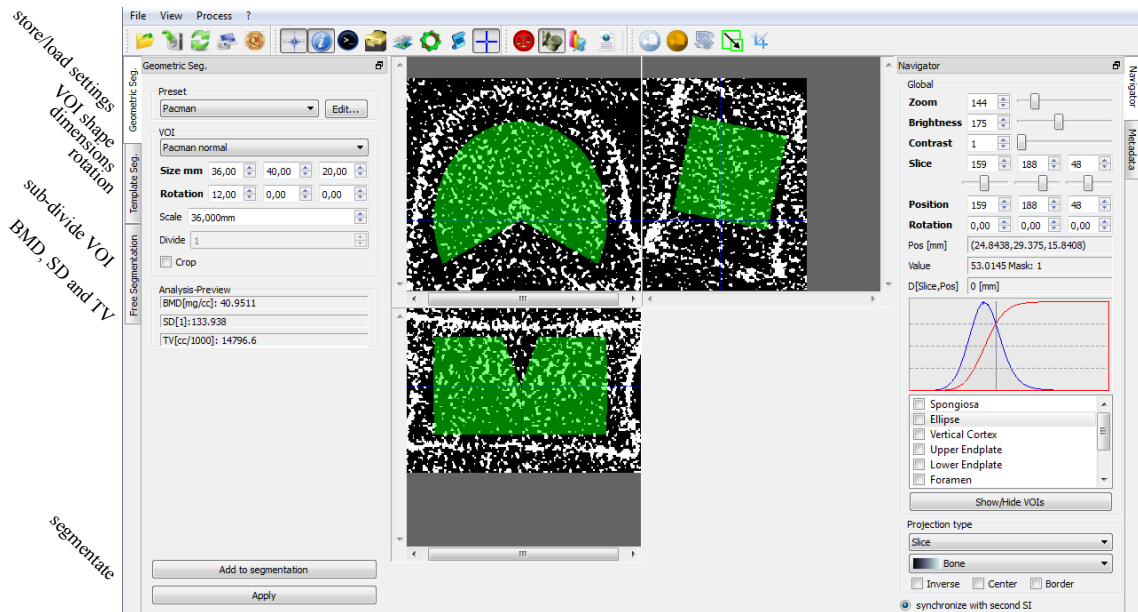


Figure 4.8: Geometric segmentation allows to define a VOI by applying and adjusting predefined geometric shapes. It also allows an ad-hoc computation of BMD and TV.

define boxes, spheres, cylinders and Pacman-shaped VOIs. The size and rotation can be adjusted and the VOIs can be subdivided, generating for instance $3 \times 3 \times 3$ sub-VOIs. Additionally a preview analysis containing the BMD, the standard deviation and the total volume are computed in a threaded manner not to freeze the principal functionality. The use of the geometric segmentation is in general sufficient for the analysis of microstructural parameters of the spongy bone.

The template segmentation, Fig. 4.9, already existed in Structural Insight 2.0 and is detailed explained in [46]. Only few internal changes between the two versions exist, while the principal functionality was maintained. This function defines a set of different anatomical regions, a central ellipse, the total spongiosa, the vertical cortex, the upper and lower endplates, foramen and pedicle. This kind of segmentation is required for analyzing the cortex or sub-cortex, as well as for a finite element analysis.

4.3.3 Computation of micro-structural parameters

The class `Analysis` contains the functions for the computation of the structural parameters, Fig 4.10. The user-interface `AnalysisWidget` allows to select the VOIs, the threshold and a shrinking. The shrinking is a morphological erosion to allow

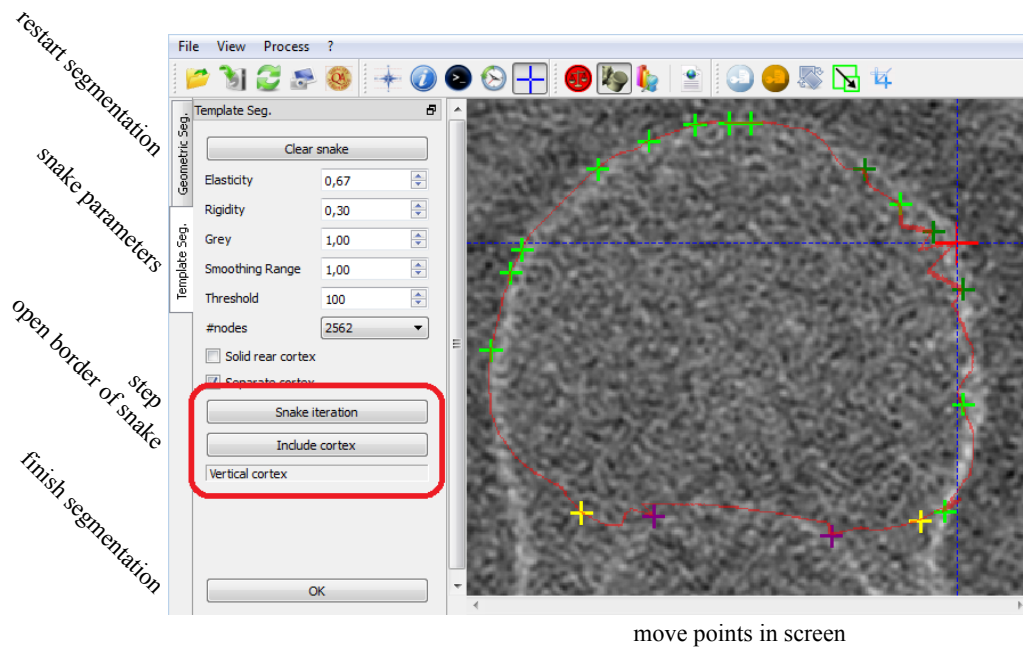


Figure 4.9: Template segmentation: The points of the cortex are colored according to the anatomical membership, green: vertical cortex, yellow: cut pedicle, purple: foramen, etc. additionally the currently selected node is enhanced in red.

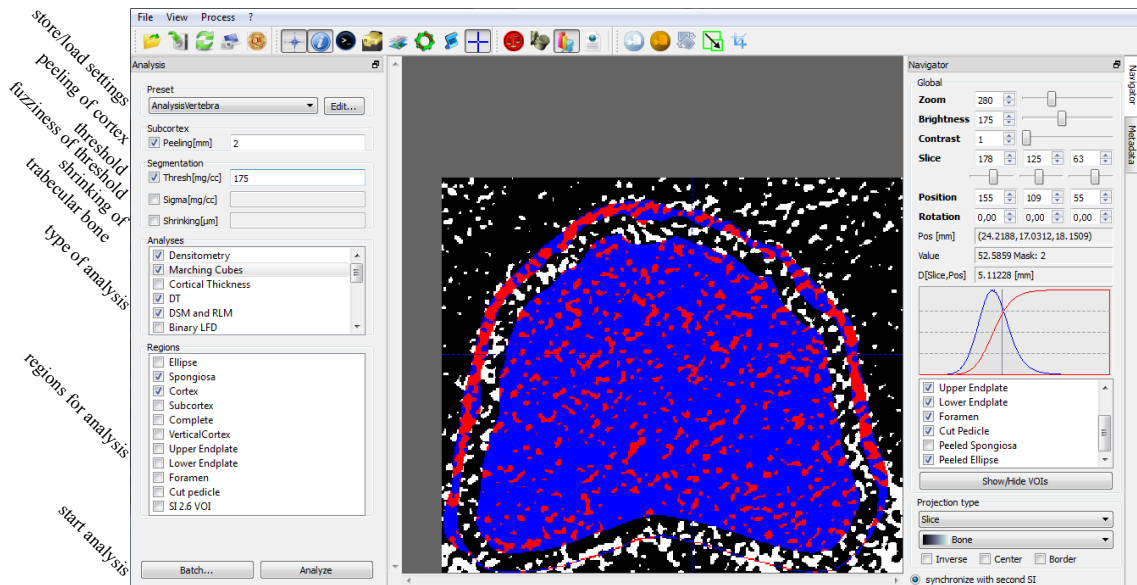
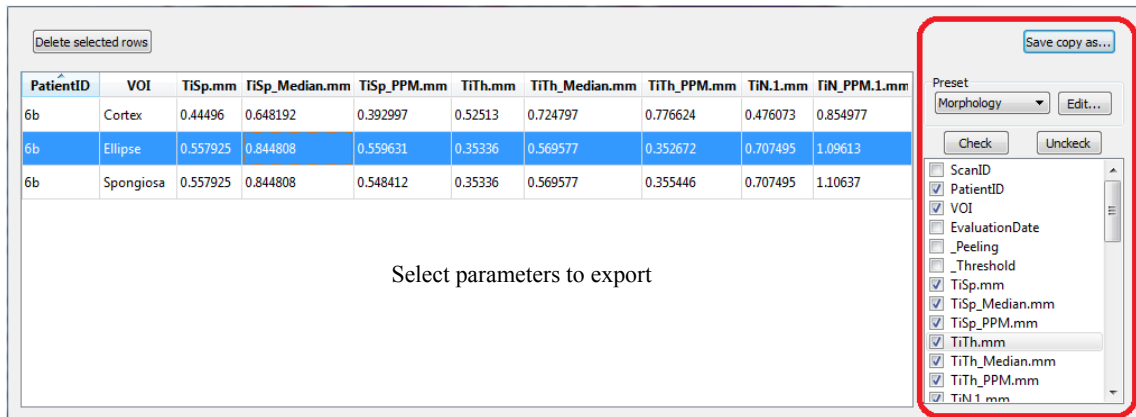


Figure 4.10: Computation of micro-structural parameters: Allows peeling to define the sub-cortex and shrinking as a morphological erosion of $Bone_{t,\sigma}$.



PatientID	VOI	TiSp.mm	TiSp_Median.mm	TiSp_PPM.mm	TiTh.mm	TiTh_Median.mm	TiTh_PPM.mm	TiN.1.mm	TiN_PPM.1.mm
6b	Cortex	0.44496	0.648192	0.392997	0.52513	0.724797	0.776624	0.476073	0.854977
6b	Ellipse	0.557925	0.844808	0.559631	0.35336	0.569577	0.352672	0.707495	1.09613
6b	Spongiosa	0.557925	0.844808	0.548412	0.35336	0.569577	0.355446	0.707495	1.10637

Select parameters to export

Save copy as...

Preset: Morphology Edit...

Check Uncheck

- ScanID
- PatientID
- VOI
- EvaluationDate
- _Peeling
- _Threshold
- TiSp.mm
- TiSp_Median.mm
- TiSp_PPM.mm
- TiTh.mm
- TiTh_Median.mm
- TiTh_PPM.mm
- TiN.1.mm

Figure 4.11: Export of the computed structural parameters: It allows to select and to sort specific parameters. A given set of parameters for exportation can be stored as preset.

a thinning of the bone segmentation. The sub-cortex is defined with the peeling-parameter. The sub-cortex is an extra VOI defining the outer shell of the spongiosa. Parameters are generally not computed on the sub-cortex, but it serves to shrink the VOI of the spongiosa to allow a more homogenous analysis of. The sub-cortex contains structural properties which in between the ones of the cortex and the ones of the spongiosa. Sigma is a parameter for the definition of a non-crisp binarization, see Sec. 2.4.2, though applicable only to some methods. The class provides the list of implemented structural parameters and contains a batch function, that applies the identical analysis to a set of previously segmented volumes.

For every VOI, one result entity is generated, containing the following meta data: patient ID, date of birth (DOB), name of the study, name of the site, scan ID, scan date, image resolution, volume of each voxel, voltage[kV], exposure[mAs], CT-kernel, table height[mm], date and time of the segmentation, kind of segmentation, current date and time, evaluation date, file name, current version of Structural Insight and the complete path of the file. The structural parameters are computed for all VOIs in the same moment loop, that means the complexity of the algorithms is independent of the number of VOIs. The results of the analysis are shown with the class `Results`, Fig. 4.11. It provides functions to select, sort and delete entries and to export all or selected parameters to comma separated or .xml formats, which can be then directly opened in Excel-like statistical programs.

4.4 Implementation of the structural parameters

The following structural parameters have been implemented in Structural Insight.

4.4.1 Voxel counting

Changes of the voxel counting method include the support of float-coded densities, instead of integer coded densities as in Structural Insight 2.0, and the support of fuzzy bone maps. The parameters are identical to the ones, computed with Structural Insight 2.0

- bone mineral density: BMD[mg/cc]
- segmented BMD: BMDseg[mg/cc]
- bone volume: BV[cc/1000]
- total volume: TV[cc/1000]
- bone mineral content: BMC[mg]
- segmented BMC: BMCseg[mg]
- bone volume fraction: BV/TV[1].

4.4.2 Marching cubes

The marching cubes method is for the first time included in Structural Insight. The implementation is based on [53] and follows the implementation suggested in [123]. While the standard implementation is used to derive a model independent bone surface, it was here extended to compute the bone volume as well. Therefore a two lists of coordinates are loaded, one containing the triangles defining the bone surface and another containing tetrahedrons. Each vertex of the triangle or tetrahedron is denoted by an index between 0 and 19. The first 8 indices denote the fixed corners of the cube and the following 12 indices denote the moving edges of the cube. The actual position of the moving edges is computed from the density of the 8 voxels, that create each cube. While the list of the faces `MCFaces.txt` is already comprehensive, the one of the tetrahedrons `MCVolumes.txt` is even more complex. The following parameters can be derived

- Structure model index: MC.SMI[1]
- Fragmentation index or trabecular bone pattern factor [47]: MC.Fr.I[1/mm]
- Bone surface in square mm: MC-BS[mm.mm]
- A bone volume based on the volume of the cubes: MC.BV[cc/1000]
- The bone surface fraction $(MC.BS[mm.mm]/MC.BV[cc/1000])$:
MC.BS/BV[1/mm]
- the segmented BMD: MC.BMDseg[mg/cc]
- the segmented BMC: MC.BMCseg[mg]

4.4.3 Thickness transform method

The thickness transform method was for the first time adapted to the analysis of the spongy bone in Structural Insight and implemented as described in [54]. Parameters are

- Trabecular separation: DT.Tb.Sp[mm]
- Standard deviation of Tb.Sp: DT.Tb.Sp.SD[mm]
- Trabecular thickness: DT.Tb.Th[mm]
- Standard deviation of Tb.Th: DT.Tb.Th.SD[mm]
- Weighted Tb.Sp, which is similar to wCt.Th[mm], but with different thresholds: DT.wTb.Sp[mm]
- weighted standard deviation of Tb.Sp: DT.wTb.Sp.SD[mm]
- weighted Tb.Th: DT.wTb.Th.SD[mm]
- weighted standard deviation of Tb.Th: DT.wTb.Th.SD[mm]

The computation of the cortical thickness based on the same principle, however by using the VOI instead of the bone map as the signal for the computation of the distance transform. The parameters are identical to these computed with version 2.0,

- cortical thickness based on the segmentation: Ct.Th[mm]
- weighted Ct.Th, as defined in [46]: wCt.Th[mm]
- Standard deviation of Ct.Th as defined in [54]: Ct.Th.SD[mm]
- Standard deviation of wCt.Th: wCt.Th.SD[mm]

4.4.4 Direct secant method and run-length method

The direct secant method (DSM) followed the definition of [122]. The implementation of the direct secant and run-length method are improved compared to the algorithms of Structural Insight 2.0. In Structural Insight 3.0, the directions of the test-rays are pre-defined, but not randomly generated as in version 2.0. The particular directions are loaded from a text file [50]. This has the advantage, that the test direction are covering optimally the surface of the unit-sphere and that the methods become deterministic. Furthermore, the line-segments which overlap the VOI but which are not entirely inside the VOI contribute only with the amount of their intersection to the histogram. Two types of histograms are internally computed, a global one containing all lengths of all line-segments, and local ones, only considering line-segments of a particular angle. From each histogram, the mean [49] and median [46] are computed. The following parameters can be obtained with the direct secant method,

- trabecular number as the median of the trabecular numbers of all direction: DSM-Tb.N[1/mm]
- trabecular separation $(1-BV/TV[1])/DSM.Tb.N[1/mm]$: DSM.Tb.Sp[mm]
- trabecular thickness $BV/TV[1] / DSM.Tb.N[1/mm]$: DSM.Tb.Th[mm]
- bone surface fraction: $2 DSM.Tb.N[1/mm]/(BV/TV[1])$: BS/TV[1/mm]
- from the distribution of mean intercept lengths of all angles ($MIL(\theta_i) = BV/TV*2/DSM.Tb.N(\theta_i)$ [1/mm]), the minimum mean intercept length is computed: MIL.Min[mm]
- the average mean intercept length: MIL.Avg[mm]
- the maximum mean intercept length: MIL.Max[mm]

- The distribution of $MIL(\theta_1, \dots, \theta_N)$ is also analyzed with a principal component analysis, giving the first eigenvalue of $MIL(\theta_1, \dots, \theta_N)$: MIL.Principal1[mm]
- the second eigenvalue of $MIL(\theta_1, \dots, \theta_N)$: MIL.Principal2[mm]
- the third eigenvalue of $MIL(\theta_1, \dots, \theta_N)$: MIL.Principal3[mm]
- the degree of anisotropy ($MIL.Principal1[mm]/MIL.Principal3[mm]$): MIL.DA[1]

The run-length method (RLM) as defined by [46, 49] is based on a histogram of the run-length of the bone phase $histoBone(\theta_i)$ and a histogram of the run-length of the marrow phase $histoMarrow(\theta_i)$, separately for each angle θ . The following parameters can be obtained,

- trabecular separation as the median of the medians of each directed marrow-histogram $MED_i(MED_{\theta_i}(histoMarrow))$: RLM.Tb.Sp[mm]
- trabecular thickness as the median of the medians of each directed bone-histogram $MED_i(MED_{\theta_i}(histoBone))$: RLM.Tb.Th[mm]
- the trabecular number from the run-length method $1/RLM.Tb.Th[mm]$: RLM.Tb.N[1/mm]
- trabecular separation as the median of the mean of each directed marrow-histogram $MED_i(AVG_{\theta_i}(histoMarrow))$: RLM.AVG.Tb.Sp[mm]
- trabecular separation as the median of the mean of each directed bone histogram $MED_i(AVG_{\theta_i}(histoBone))$: RLM.AVG.Tb.Th[mm]
- the trabecular number from the average-run-length method $1/RLM.AVG.Tb.Th[mm]$: RLM.AVG.Tb.N[1/mm]
- Statistics of the median run length, computed in accordance to the mean intercept length are the eigenvalues and the degree of anisotropy, hence the first eigenvalue: MRL-Eigenvalue1[mm]
- The second eigenvalue of the mean run length: MRL-Eigenvalue2[mm]
- The third eigenvalue of the mean run length: MRL-Eigenvalue3[mm]

- The degree of anisotropy of the mean run length: MRL-DA[1]

Most of these parameters are implemented in many standard software packages (for instance BoneJ, or Bruker Sykscan CT, etc.), but in particular the parameters of the run-length method, are only implemented in Structural Insight. The software contains further provisional methods, based on weighted densities or fractal methods, that were not shown in this work. The publication [130] describes some of these experimental parameters.

Conclusions

The computation of micro-structural parameters from in-vivo CT is a field of ongoing research. Variables of the pipeline of processing such 3D volumes are (1) the kind of CT scanner, such as single energy or dual energy CT, (2) the reconstruction method, such as filtered back projection or novel iterative reconstruction methods, (3) the calibration technique, (4) the definition of the VOI, (5) the preprocessing, such as binarization, noise reduction or upsampling methods and finally (6) the type of methods to compute the actual micro-structural parameters. This work concentrated on the development of novel robust methods for preprocessing and the computation of the micro-structural variables.

Chapter 2 discussed general themes of the processing of quantitative CT data. Different techniques for the visualization have been described in Sec. 2.1. These techniques play an important role for the quality assurance and are important for the manual definition of the VOI, Sec. 2.3. The calibration of the density values has been described in Sec. 2.2. A method for the automatic placement of calibration phantoms was developed and applied to a real study. This proposed method used a gradient based directional weighted circular Hough-transform. A generalization of the crisp binarization to access the bone phase has been discussed, Sec. 2.4.2. This technique uses a second parameter σ , which reflects the fuzziness of the binarization process. Furthermore, the influence of iterative reconstruction techniques has been qualitatively described in Sec. 2.5. Finally, the most important structural parameters were described in Sec. 2.4.

Novel approaches to improve the robustness of micro-structural parameters have been described in Ch. 3. First, the conducted experiments to obtain the CT data and the specific statistical methods to analyze the novel methods have been described in Sec. 3.1 and the common definitions of the neighborhood operators were introduced in Sec. 3.2. The general approach to obtain the ridge of the bone uses

skeletonization techniques. Section 3.3 describes two alternative methods to obtain the ridge map of the bone. In total four different applications of robust local operators were presented in the following sections, (1) to improve the preprocessing for the obtainment of micro-structural parameters in general (2) to obtain the rod-volume ratio in particular on junctions of rods or plates, (3) to obtain the rod-volume ratio and trabecular thickness with the local fractal dimension and (4) an application to diffusion tensor imaging. All of those methods contain separate discussion and conclusion sections. The last chapter 4 describes the program Structural Insight a software for the quantitative and qualitative analysis of CT volumes.

The independent methods and techniques of CT processing are all part of the same process, although they might appear to be disconnected. The standard CT processing does not need to be entirely replaced by a new processing pipeline, but certain processing steps can be replaced or aggregated. By improving the reconstruction method does not alter the forthcoming processing steps but increases the precision and accuracy of the obtained micro-structural parameters. Similar principles apply for the automatic placement of the calibration phantom, the improved binarization, the fuzzy skeletonization with the Monogenic signal and the microstructural calibration. While a combined application of all of these techniques would likely improve the outcome of the micro-structural parameters, in the same moment it would be impossible to evaluate each of these techniques in terms of their contribution to the quality of the outcome. Hence the conducted experiments did mostly not combine any two of the proposed methods and the novel parameters were not compared in between each other but instead towards the state-of-the art standard entities. The program Structural Insight serves as a framework program to fix and spread the implemented methods. A number of scientific works have been already conducted with the help of this software. Hence, the long-term goal of the ongoing research is the integration of all proposed techniques into Structural Insight, in particular to allow the combined robust preprocessing and computing of micro-structural parameters.

Future work

Possible future work regarding each method has been throughout mentioned in Secs. 3.4, 3.5 and 3.6. In particular further investigations of the local fractal dimension seem to be promising. The obtained results with the reported method significantly

improves the prediction of fracture risk under in-vivo conditions and is able to explain up to 90% of the failure load. Still, the complementary proposed techniques were not combined with this method, hence the iterative reconstruction, the fuzzy threshold, the micro-structural calibration and the improved definition of the bone-ridge map are likely to further boost the performance of the proposed approach. Additionally the fractal method itself contains still adjustable parameters and settings, for instance the decreasing uncertainty of the logarithm of the local bone volume with increasing radius has not yet been involved into the method. Also the exchange of the circular structural element with the Gaussian structural element likely yields improved capacities to explain failure load.

The local operators which have been applied on DTI can be interpreted as a local measure. By changing the radius of the local neighborhood, a local fractal dimension could be established. This could allow not only to access the direction and strength of the white matter fibers but also their structural organization, and might be in particular helpful for the detection of tumors which force the fibers to be organized in uncommon shapes. This extension is planned to be investigated in the closest future.

Acknowledgements

This doctoral thesis was realized since I got a lot of support by my advisers, colleagues, family and friends. I would like to thank my supervisors Dr. Claudio Delrieux, Dr. Claus-Christian Glüer and Dr. Rodrigo de Luis-García. Also I like to thank the Consejo Nacional de Investigaciones Científicas y Técnicas and the Universidad Nacional del Sur in Bahía Blanca for my doctorate fellowship. I would like to thank Jaime Peña, Dr. Yongtao Lu, Dr. Jan Borggreffe, Dr. Graeme Campbell, Dr. Gerd Huber and Andrea Silveti for supporting my research. Finally I like to thank Valeria, my parents, my brother and my sisters as well as Valeria's family for their constant support.

List of Figures

1.1	Bone measurement modalities	3
1.2	Scanners without X-ray technique	4
1.3	Scanners with X-ray technique	5
1.4	Human vertebra scanned with HRpQCT and HRQCT	6
1.5	Pipeline of CT processing	9
2.1	Sample colormaps	17
2.2	Sample 3D projections	18
2.3	Sample ray casting	19
2.4	Calibration phantom models	21
2.5	Calibration phantoms under CT	22
2.6	Automatic placing of the calibration phantom	23
2.7	Morphometric methods	29
2.8	Fuzzy threshold	32
2.9	Prototypes of marching cubes	35
2.10	Bone volume obtained with VC and MC	36
2.11	Distance transform method	37
2.12	Iterative reconstruction methods	41
3.1	CT setup vertebra phantom	45
3.2	Comparison HRQCT <i>vs.</i> HRpQCT	47
3.3	Ex-vivo <i>vs.</i> in-vivo quality	47
3.4	Setup for BioAsset scans	50
3.5	In silico data	51
3.6	Sample structural elements	56
3.7	Monogenic signal: reconstruction and phase	63
3.8	Monogenic signal: Ridge	66

3.9	Micro-structural calibration: histogram	67
3.10	Micro-structural calibration: high- and low-pass filter	69
3.11	Micro-structural calibration: sample micro-structural parameters . . .	71
3.12	Micro-structural calibration: Short-term and long-term precision . . .	71
3.13	Rose diagrams: prototype samples	75
3.14	Rose diagrams: distinction of plates and rods	78
3.15	Rose diagrams: Sample application	80
3.16	Fractal dimension: Evolution of the slope	83
3.17	Fractal dimension: Application on noisy sample	87
3.18	Fractal dimension: Mathematical derivation of the second method . .	87
3.19	Fractal dimension: Short term and long term precision	89
3.20	Fractal dimension: Prediction of failure load	92
3.21	MRI: Workflow	99
3.22	MRI: Sample of local operators	101
3.23	MRI: Number of significant different TBSS voxels	104
3.24	MRI: Spatial distribution of significant differences	105
3.25	MRI: Noise analysis	106
3.26	MRI: White matter share of local neighborhoods	107
4.1	Version timeline of Structural Insight	111
4.2	Program structure	115
4.3	Main screen	116
4.4	Two sample thread schemes	119
4.5	Example threaded rendering	120
4.6	Quality assurance	122
4.7	Calibration	124
4.8	Geometric segmentation	125
4.9	Template segmentation	126
4.10	Computation of micro-structural parameters	126
4.11	Export of the computed structural parameters	127

List of Tables

- 2.1 Linear att. coefficients, HU's and DV's of common substances. 20
- 3.1 Performed scans of each vertebra phantom. 48
- 3.2 Fractal dimension: Descriptive statistics 90
- 3.3 Fractal dimension: Spearman's rank correlation coefficients 91
- 3.4 Fractal dimension: Prediction of failure load 92

Bibliography

- [1] P. S. Addison. *Fractals and chaos: an illustrated course*. Bristol, Eng, Philadelphia: Institute of physics publishing, 1997.
- [2] K. Aho, D. Derryberry, and T. Peterson. Model selection for ecologists: the worldviews of AIC and BIC. *Ecology*, 95(3):631–636, 2014.
- [3] K. Anselme. Osteoblast adhesion on biomaterials. *Biomaterials*, 21(7):667–681, 2000.
- [4] J. Ashburner and K. J. Friston. Voxel-based morphometry - the methods. *Neuroimage*, 11(6):805 – 821, 2000.
- [5] B. Banneheka and G. Ekanayake. A new point estimator for the median of gamma distribution. *Viyodaya Journal of Science*, 14:95–103, 2009.
- [6] M. Barnsley, R. Devaney, B. Mandelbrot, D. Peitgen, and R. Voss. *The Science of Fractal Images*. Springer, 1988.
- [7] P. J. Basser and C. Pierpaoli. Microstructural and physiological features of tissues elucidated by quantitative-diffusion tensor MRI. *Journal of Magnetic Resonance, Series B*, 111:209–219, 1996.
- [8] P. J. Basser, J. Mattiello, and D. LeBihan. Estimation of the effective self-diffusion tensor from the NMR spin echo. *Journal of Magnetic Resonance, Series B*, 103(3):247–254, 1994.
- [9] C. Benhamou, E. Lespessailles, G. Jacquet, R. Harba, R. Jennane, T. Lousot, D. Tourliere, and W. Ohley. Fractal organization of trabecular bone images on calcaneus radiographs. *Journal of Bone and Mineral Research*, 9(12):1909–1918, 1994.
- [10] D. I. Benn. Fabric shape and the interpretation of sedimentary fabric data. *Journal of Sedimentary Research*, 64(4), 1994.
- [11] J. Borggreffe, N. Abdullayev, M. Hellmich, F. Thomsen, T. Damm, J. Peña, S. Waldhausen, C.-C. Glüer, D. Maintz, and B. Krug. Veränderungen der com-

- putertomografisch erfassten trabekulären Mikrostruktur unter Verwendung von iterativen Rekonstruktionsalgorithmen. In *Deutscher Röntgenkongress: Technik für Menschen*, 2015.
- [12] J. Borggrefe, S. Giravent, G. Campbell, F. Thomsen, D. Chang, M. Franke, A. Günther, M. Heller, and A. Wulff. Association of osteolytic lesions, bone mineral loss and trabecular sclerosis with prevalent vertebral fractures in patients with multiple myeloma. *European Journal of Radiology*, 84(11):2269–2274, 2015.
- [13] J. Borggrefe, S. Giravent, F. Thomsen, J. Peña, G. Campbell, A. Wulff, A. Günther, M. Heller, and C.-C. Glüer. Association of QCT bone mineral density and bone structure with vertebral fractures in patients with multiple myeloma. *Journal of Bone and Mineral Research*, 30(7):1329–1337, 2015.
- [14] J. Borggrefe, N. Abdullayev, F. Thomsen, J. Peña, S. Waldhausen, M. Hellmich, C.-C. Glüer, and B. Krug. Comparison of changes in quantitative computed tomography bone structure and bone density using two different reconstruction methods. *Drafted*, 2016.
- [15] S. Brown, D. Bailey, C. Baldock, et al. An investigation of the relationship between linear attenuation coefficients and CT Hounsfield units. *Australasian Physical & Engineering Sciences in Medicine*, 29(1):140, 2006.
- [16] S. Brown, D. L. Bailey, K. Willowson, and C. Baldock. Investigation of the relationship between linear attenuation coefficients and CT Hounsfield units using radionuclides for SPECT. *Applied Radiation and Isotopes*, 66(9):1206–1212, 2008.
- [17] M. D. Budde, M. Xie, A. H. Cross, and S.-K. Song. Axial diffusivity is the primary correlate of axonal injury in the experimental autoimmune encephalomyelitis spinal cord: a quantitative pixelwise analysis. *The Journal of Neuroscience*, 29(9):2805–2813, 2009.
- [18] K. P. Burnham and D. R. Anderson. Multimodel inference understanding aic and bic in model selection. *Sociological Methods & Research*, 33(2):261–304, 2004.
- [19] G. Campbell, C. Graeff, S. Giravent, F. Thomsen, J. Peña, A. Wulff, A. Günther, C.-C. Glüer, and J. Borggrefe. Prediction of vertebral body stiffness in patients with multiple myeloma using qCT-based finite element models. In *European Calcified Tissue Society Congress*, 2013.

- [20] G. Campbell, J. Peña, S. Giravent, F. Thomsen, T. Damm, C.-C. Glüer, and J. Borggrefe. Assessment of bone fragility in patients with multiple myeloma using qct-based finite element modeling. *Journal of Bone and Mineral Research*, 1(32):151–156, 2017.
- [21] E. V. Chernyaev. Marching cubes 33: construction of topologically correct iso-surfaces. *Institute for High Energy Physics, Moscow, Russia, Report CN/95-17*, 1995.
- [22] H. Chung, C. Chu, M. Underweiser, F. Wehrli, et al. On the fractal nature of trabecular structure. *Medical Physics*, 21(10):1535, 1994.
- [23] M. P. Cipolletti, C. A. Delrieux, G. M. Perillo, and M. Cintia Piccolo. Super-resolution border segmentation and measurement in remote sensing images. *Computers & Geosciences*, 40:87–96, 2011.
- [24] M. Crookshank, H.-L. Ploeg, R. Ellis, and N. J. MacIntyre. Repeatable calibration of hounsfield units to mineral density and effect of scanning medium. *Advances in Biomechanics and Applications*, 1(1):15–22, 2014.
- [25] S. Cummings and L. Melton. Epidemiology and outcomes of osteoporotic fractures. *The Lancet*, 359(9319):1761–1767, 2002.
- [26] A. Darabi, F. Chandelier, and G. Baroud. Thickness analysis and reconstruction of trabecular bone and bone substitute microstructure based on fuzzy distance map using both ridge and thinning skeletonization. *Canadian Journal of Electrical and Computer Engineering*, 34(1/2):57–62, 2009.
- [27] R. de Luis-García, G. Cabús-Piñol, C. Imaz-Roncero, D. Argibay Quiñones, G. Barrio-Arranz, S. Aja-Fernández, and C. Alberola López. Attention deficit/hyperactivity disorder and medication with stimulants in young children: A DTI study. *Progress in Neuro-Psychopharmacology and Biological Psychiatry*, 57:176–184, 2015.
- [28] D. W. Dempster. The impact of bone turnover and bone-active agents on bone quality: focus on the hip. *Osteoporosis International*, 13(5):349–352, 2002.
- [29] M. Doube. The ellipsoid factor for quantification of rods, plates, and intermediate forms in 3D geometries. *Frontiers in Endocrinology*, 6(15), 2015.
- [30] G. Dougherty. *Medical Image Processing - Techniques and Applications*. Springer, 2011.

- [31] D. B. Ennis and G. Kindlmann. Orthogonal tensor invariants and the analysis of diffusion tensor magnetic resonance images. *Magnetic Resonance in Medicine*, 55(1):136–146, 2006.
- [32] K. Falconer. *Fractal geometry: mathematical foundations and applications*. John Wiley & Sons, 2003.
- [33] P. Farahmand, F. Marin, F. Hawkins, R. Mörnicke, J. Ringe, C.-C. Glüer, N. Papaioannou, S. Minisola, G. Martínez, J. Nolla, et al. Early changes in biochemical markers of bone formation during teriparatide therapy correlate with improvements in vertebral strength in men with glucocorticoid-induced osteoporosis. *Osteoporosis International*, 24(12):2971–2981, 2013.
- [34] M. Felsberg and G. Sommer. The monogenic signal. *Transactions on Signal Processing, IEEE*, 49:3136–3144, 2001.
- [35] A. J. Fields, S. K. Eswaran, M. G. Jekir, and T. M. Keaveny. Role of trabecular microarchitecture in whole-vertebral body biomechanical behavior. *Journal of Bone and Mineral Research*, 24(9):1523–1530, 2009.
- [36] C. S. Fortin, R. Kumaresan, W. J. Ohley, and S. Hofer. Fractal dimension in the analysis of medical images. *Engineering in Medicine and Biology Magazine, IEEE*, 11(2):65–71, 1992.
- [37] L. Frank. Characterization of anisotropy in high angular resolution diffusion-weighted MRI. *Magnetic Resonance in Medicine*, 47(6):1083–1099, 2002.
- [38] H. M. Frost. Dynamics of bone remodeling. *Bone Biodynamics*, 315, 1964.
- [39] C.-C. Glüer. Quantitative ultrasound techniques for the assessment of osteoporosis: expert agreement on current status. *Journal of Bone and Mineral Research*, 12(8):1280–1288, 1997.
- [40] C.-C. Glüer, G. M. Blake, Y. Lu, B. A. Blunt, M. Jergas, and H. K. Genant. Accurate assessment of precision errors: How to measure the reproducibility of bone densitometry techniques. *Osteoporosis International*, 5(4):262–270, 1995.
- [41] C.-C. Glüer, M. Krause, O. Museyko, B. Wulff, G. Campbell, T. Damm, M. Dauschies, G. Huber, Y. Lu, J. Peña, S. Waldhausen, J. Bastgen, K. Rohde, S. Breer, I. Steinebach, F. Thomsen, M. Amling, R. Barkmann, K. Engelke, M. Morlock, J. Pfeilschifter, and K. Püschel. New horizons for the in vivo assessment of major aspects of bone quality. *Osteologie*, 22(3):223–233, 2013.

- [42] C.-C. Glüer, F. Marin, J. D. Ringe, F. Hawkins, R. Mricke, N. Papaioannu, P. Farahmand, S. Minisola, G. Martinez, and J. M. Nolla. Comparative effects of teriparatide and risedronate in glucocorticoid-induced osteoporosis in men: 18-month results of the EuroGIOPs trial. *Journal of Bone and Mineral Research*, 28:1355–1368, 2013.
- [43] S. Goldstein. The mechanical properties of trabecular bone: Dependence on anatomic location and function. *Journal of Biomechanics*, 20(11-12):1055 – 1061, 1987.
- [44] G. Gong. Local diffusion homogeneity (LDH): An inter-voxel diffusion MRI metric for assessing inter-subject white matter variability. *Plos One*, 8(6): 1–11, 2013.
- [45] G. Grabner, A. L. Janke, M. M. Budge, D. Smith, J. Pruessner, and D. L. Collins. Symmetric atlasing and model based segmentation: an application to the hippocampus in older adults. In *Medical Image Computing and Computer-Assisted Intervention*, pages 58–66. Springer, 2006.
- [46] C. Graeff. *Bone Strength Surrogate Markers*. PhD thesis, Technische Universität Hamburg-Harburg, 2010.
- [47] M. Hahn, M. Vogel, M. Pompesius-Kempa, and G. Delling. Trabecular bone pattern factor - a new parameter for simple quantification of bone microarchitecture. *Bone*, 13(4):327–330, 1992.
- [48] M. Haidekker, R. Andresen, C. Evertsz, D. Banzer, and H. Peitgen. Issues of threshold selection when determining the fractal dimension in HRCT slices of lumbar vertebrae. *British Journal of Radiology*, 73(865):69–72, 2000.
- [49] M. A. Haidekker and G. Dougherty. Medical imaging in the diagnosis of osteoporosis and estimation of the individual bone fracture risk. In *Medical Image Processing*, pages 193–225. Springer, 2011.
- [50] R. Hardin, N. Sloane, and W. Smith. Tables of spherical codes with icosahedral symmetry. Published electronically at <http://neilsloane.com/icosahedral.codes/>, July 2013.
- [51] N. Harvey, E. Dennison, and C. Cooper. Osteoporosis: impact on health and economics. *Nature Reviews Rheumatology*, 6(2):99–105, 2010.
- [52] Y. He, B. Fan, D. Hans, J. Li, C. Wu, C. Njeh, S. Zhao, Y. Lu, E. Tsuda-Futami, T. Fuerst, et al. Assessment of a new quantitative ultrasound calcaneus measurement: precision and discrimination of hip fractures in elderly

- women compared with dual X-ray absorptiometry. *Osteoporosis International*, 11(4):354–360, 2000.
- [53] T. Hildebrand and P. Rüegsegger. Quantification of bone microarchitecture with the structure model index. *Computer Methods in Biomechanics and Bio Medical Engineering*, 1(1):15–23, 1997.
- [54] T. Hildebrand and P. Rüegsegger. A new method for the model-independent assessment of thickness in three-dimensional images. *Journal of Microscopy*, 185(1):67–75, 1997.
- [55] M. A. Horsfield and D. K. Jones. Applications of diffusion-weighted and diffusion tensor MRI to white matter diseases - a review. *NMR in Biomedicine*, 15(7-8):570–577, 2002.
- [56] A. I. Hussein and E. F. Morgan. The effect of intravertebral heterogeneity in microstructure on vertebral strength and failure patterns. *Osteoporosis International*, 24(3):979–989, 2013.
- [57] S. Hwang and F. Wehrli. Subvoxel processing: a method for reducing partial volume blurring with application to in vivo MR images of trabecular bone. *Magnetic Resonance in Medicine*, 47(5):948–957, 2002.
- [58] K. Iftekharuddin, W. Jia, and R. Marsh. Fractal analysis of tumor in brain mr images. *Machine Vision and Applications*, 13:352–362, 2003.
- [59] K. Iftekharuddin, S. Ahmed, and J. Hossen. Multiresolution texture models for brain tumor segmentation in MRI. In *Annual International Conference of the Engineering in Medicine and Biology Society, IEEE*, pages 6985–6988, 2011.
- [60] M. Jenkinson, C. Beckmann, T. Behrens, M. Woolrich, and S. Smith. FSL. *Neuroimage*, 62(2):782–790, 2012.
- [61] D. K. Jones, T. R. Knösche, and R. Turner. White matter integrity, fiber count, and other fallacies: the do’s and don’ts of diffusion MRI. *Neuroimage*, 73:239–254, 2013.
- [62] M. K. Karlsson, A. Nordvist, and C. Karlsson. Physical activity increases bone mass during growth. *Food & Nutrition Research*, 52, 2008.
- [63] R. Ketcham and T. Ryan. Quantification and visualization of anisotropy in trabecular bone. *Journal of Microscopy*, 213(2):158–171, 2004.
- [64] R. Khawaja, S. Singh, M. Gilman, A. Sharma, S. Do, S. Pourjabbar, A. Padole, D. Lira, K. Brown, J.-A. Shepard, et al. Computed tomography (CT) of the

- chest at less than 1 mSv: an ongoing prospective clinical trial of chest CT at submillisievert radiation doses with iterative model image reconstruction and iDose4 technique. *Journal of Computer Assisted Tomography*, 38(4):613–619, 2014.
- [65] P. B. Kingsley and W. G. Monahan. Contrast-to-noise ratios of diffusion anisotropy indices. *Magnetic Resonance in Medicine*, 53(4):911–918, 2005.
- [66] A. Klibanski, L. Adams-Campbell, T. L. Bassford, S. N. Blair, S. D. Boden, K. Dickersin, D. R. Gifford, L. Glasse, S. R. Goldring, K. Hruska, et al. Osteoporosis prevention, diagnosis, and therapy. *Journal of the American Medical Association*, 285(6):785–795, 2001.
- [67] M. Knapp. The cost-effectiveness challenge: is it worth it? *Alzheimer’s Research & Therapy*, 7(1):1, 2015.
- [68] P. Kochunov, P. Thompson, J. Lancaster, G. Bartzokis, S. Smith, T. Coyle, D. Royall, A. Laird, and P. Fox. Relationship between white matter fractional anisotropy and other indices of cerebral health in normal aging: tract-based spatial statistics study of aging. *Neuroimage*, 35(2):478 – 487, 2007.
- [69] X.-Z. Kong. Association between in-scanner head motion with cerebral white matter microstructure: a multiband diffusion-weighted MRI study. *Peer J*, 2: e366, 2014.
- [70] K. Konrad and S. B. Eickhoff. Is the ADHD brain wired differently? A review on structural and functional connectivity in attention deficit hyperactivity disorder. *Human Brain Mapping*, 31(6):904–916, 2010.
- [71] A. Krebs, C. Graeff, I. Frieling, B. Kurz, W. Timm, K. Engelke, and C.-C. Glüer. High resolution computed tomography of the vertebrae yields accurate information on trabecular distances if processed by 3D fuzzy segmentation approaches. *Bone*, 44(1):145 – 152, 2009.
- [72] M. Kubicki, R. McCarley, C.-F. Westin, H.-J. Park, S. Maier, R. Kikinis, F. A. Jolesz, and M. E. Shenton. A review of diffusion tensor imaging studies in schizophrenia. *Journal of Psychiatric Research*, 41(1):15–30, 2007.
- [73] A. Lerner, M. A. Mogensen, P. E. Kim, M. S. Shiroishi, D. H. Hwang, and M. Law. Clinical applications of diffusion tensor imaging. *World Neurosurgery*, 82(1):96–109, 2014.
- [74] T. Lindeberg. Edge detection and ridge detection with automatic scale selection. *International Journal of Computer Vision*, 30(2):117–156, 1998.

- [75] X. S. Liu, P. Sajda, P. K. Saha, F. W. Wehrli, G. Bevill, T. M. Keaveny, and X. E. Guo. Complete volumetric decomposition of individual trabecular plates and rods and its morphological correlations with anisotropic elastic moduli in human trabecular bone. *Journal of Bone and Mineral Research*, 23(2):223–235, 2008.
- [76] R. Lopes and N. Betrouni. Fractal and multifractal analysis: a review. *Medical Image Analysis*, 13(4):634 – 649, 2009.
- [77] R. Lopes, P. Dubois, I. Bhourri, M. Bedoui, S. Maouche, and N. Betrouni. Local fractal and multifractal features for volumic texture characterization. *Pattern Recognition*, 44(8):1690 – 1697, 2011.
- [78] W. E. Lorensen and H. E. Cline. Marching cubes: a high resolution 3D surface construction algorithm. In *ACM Siggraph Computer Graphics*, volume 21, pages 163–169. ACM, 1987.
- [79] Y. Lu, M. Krause, A. Heinemann, F. Thomsen, and G. Huber. Influence of different CT scans on bone strength prediction using the finite element method. In *International Symposium on Computer Methods in Biomechanics and Biomedical Engineering*, 2012.
- [80] Y. Lu, G. Maquer, O. Museyko, K. Püschel, K. Engelke, P. Zysset, M. Morlock, and G. Huber. Finite element analyses of human vertebral bodies embedded in polymethylmethacrylate or loaded via the hyperelastic intervertebral disc models provide equivalent predictions of experimental strength. *Journal of Biomechanics*, 47(10):2512–2516, 2014.
- [81] Y. Lu, M. Krause, N. Bishop, K. Sellenschloh, C.-C. Glüer, K. Püschel, M. Ameling, M. Morlock, and G. Huber. The role of patient-mode high-resolution peripheral quantitative computed tomography indices in the prediction of failure strength of the elderly womens thoracic vertebral body. *Osteoporosis International*, 26(1):237–244, 2015.
- [82] W.-C. Ma, F.-C. Wu, and M. Ouhyoung. Skeleton extraction of 3D objects with radial basis functions. In *Shape Modeling International*, pages 207–215, 2003.
- [83] B. Mandelbrot. How long is the coast of Britain? Statistical self-similarity and fractional dimension. *Science*, 156(3775):636–638, 1967.
- [84] B. Mandelbrot. *The fractal geometry of nature*. Freeman, 1983.

- [85] G. Maquer, Y. Lu, E. Dall’Ara, Y. Chevalier, M. Krause, L. Yang, R. Eastell, K. Lippuner, and P. K. Zysset. The initial slope of the variogram, foundation of the trabecular bone score, is not or is poorly associated with vertebral strength. *Journal of Bone and Mineral Research*, 31(2):341–346, 2016.
- [86] J. A. Martínez, A. Y. Izquierdo, and B. G. Gardel. Estudio de costes en la enfermedad de Alzheimer. *Revista Clínica Española*, 204(2):64–69, 2004.
- [87] B. R. McCreadie and S. A. Goldstein. Biomechanics of fracture: is bone mineral density sufficient to assess risk? *Journal of Bone and Mineral Research*, 15(12):2305–2308, 2000.
- [88] MicroCT-World. The surface of an object. Published electronically at <http://microctworld.net/the-surface-of-an-object-bone-surface-bs-and-specific-bone-surface-bsbv>, December 2016.
- [89] R. Moreno, Ö. Smedby, and M. Borga. Soft classification of trabeculae in trabecular bone. In *International Symposium on Biomedical Imaging, IEEE*, pages 1641–1644. IEEE, 2011.
- [90] R. Moreno, M. Borga, and Ö. Smedby. Estimation of trabecular thickness in gray-scale images through granulometric analysis. In *Proceedings of SPIE*, volume 8314, pages 831451, 1–9, 2012.
- [91] R. Moreno, M. Borga, and Ö. Smedby. Evaluation of the plate-rod model assumption of trabecular bone. In *International Symposium on Biomedical Imaging, IEEE*, pages 470–473. IEEE, 2012.
- [92] T. E. Nichols and A. P. Holmes. Nonparametric permutation tests for functional neuroimaging: a primer with examples. *Human Brain Mapping*, 15(1): 1–25, 2002.
- [93] S. Novianto, Y. Suzuki, and J. Maeda. Near optimum estimation of local fractal dimension for image segmentation. *Pattern Recognition Letters*, 24:365 – 374, 2003.
- [94] L. J. O’Donnell and C.-F. Westin. An introduction to diffusion tensor image analysis. *Neurosurgery Clinics of North America*, 22(2):185–196, 2011.
- [95] K. Oishi, A. Faria, H. Jiang, X. Li, K. Akhter, J. Zhang, J. T. Hsu, M. I. Miller, P. C. van Zijl, M. Albert, C. G. Lyketsos, R. Woods, A. W. Toga, G. B. Pike, P. Rosa-Neto, A. Evans, J. Mazziotta, and S. Mori. Atlas-based whole brain white matter analysis using large deformation diffeomorphic metric mapping:

- application to normal elderly and Alzheimer's disease participants. *Neuroimage*, 46(2):486 – 499, 2009.
- [96] N. Otsu. A threshold selection method from gray-level histograms. *Transactions on Systems, Man, and Cybernetics, IEEE*, 9(1):62–66, 1979.
- [97] E. Özarlan, B. C. Vemuri, and T. H. Mareci. Generalized scalar measures for diffusion MRI using trace, variance, and entropy. *Magnetic Resonance in Medicine*, 53(4):866–876, 2005.
- [98] A. Parfitt, M. Drezner, F. Glorieux, J. Kanis, H. Malluche, P. Meunier, S. Ott, and R. Recker. Bone histomorphometry: standardization of nomenclature, symbols, and units: report of the ASBMR histomorphometry nomenclature committee. *Journal of Bone and Mineral Research*, 2(6):595–610, 1987.
- [99] H. Peitgen, H. Jürgens, and D. Saupe. *Chaos and Fractals: New Frontiers of Science*. Springer, 2004.
- [100] J. Peña, S. Waldhausen, G. Campbell, R. Barkmann, F. Thomsen, and C.-C. Glüer. Simulation of the influence of material properties and image quality on HRQCT-based bone densitometry. In *International Bone Densitometry Workshop*, 2012.
- [101] J. Peña, G. Campbell, T. Damm, R. Barkmann, S. Waldhausen, F. Thomsen, M. Krause, K. Püschel, and C.-C. Glüer. Bone marrow densitometry by clinical high resolution computed tomography of human vertebrae. In *European Calcified Tissue Society Congress*, 2014.
- [102] J. Peña, F. Thomsen, T. Damm, G. Campbell, J. Bastgen, R. Barkmann, and C.-C. Glüer. Bone-marrow densitometry: assessment of marrow space of human vertebrae by single energy high resolution quantitative computed tomography. *Medical Physics*, 43(7):4174–4183, 2016.
- [103] A. Pentland. Fractal-based description of natural scenes. *Transactions on Pattern Analysis and Machine Intelligence, IEEE*, 6:661–674, 1984.
- [104] C. Pierpaoli and P. J. Basser. Toward a quantitative assessment of diffusion anisotropy. *Magnetic Resonance in Medicine*, 36(6):893–906, 1996.
- [105] L. Pothuaud, P. Carceller, and D. Hans. Correlations between grey-level variations in 2D projection images (TBS) and 3D microarchitecture: applications in the study of human trabecular bone microarchitecture. *Bone*, 42(4):775–787, 2008.

- [106] C. Pudney. Distance-ordered homotopic thinning: a skeletonization algorithm for 3D digital images. *Computer Vision and Image Understanding*, 72(3): 404–413, 1998.
- [107] L. Rimoldini. Weighted skewness and kurtosis unbiased by sample size and gaussian uncertainties. *Astronomy and Computing*, 5:1–8, 2014.
- [108] S. D. Rockoff, E. Sweet, and J. Bleustein. The relative contribution of trabecular and cortical bone to the strength of human lumbar vertebrae. *Calcified Tissue Research*, 3(1):163–175, 1969.
- [109] J. Russ. *The image processing handbook*. CRC, 2006.
- [110] J. C. Russ. *Fractal surfaces*. Springer, 1994.
- [111] P. Saha, B. Chaudhuri, and D. Dutta Majumder. A new shape preserving parallel thinning algorithm for 3D digital images. *Pattern Recognition*, 30(12):1939–1955, 1997.
- [112] P. Saha, B. Gomberg, and F. Wehrli. Three-dimensional digital topological characterization of cancellous bone architecture. *International Journal of Imaging Systems and Technology*, 11(1):81–90, 2000.
- [113] P. Saha, F. Wehrli, and B. Gomberg. Fuzzy distance transform: theory, algorithms, and applications. *Computer Vision and Image Understanding*, 86(3): 171–190, 2002.
- [114] P. K. Saha, Y. Xu, H. Duan, A. Heiner, and G. Liang. Volumetric topological analysis: a novel approach for trabecular bone classification on the continuum between plates and rods. *IEEE Transactions on Medical Imaging*, 29(11): 1821–1838, 2010.
- [115] P. L. Salmon, C. Ohlsson, S. J. Shefelbine, and M. Doube. Structure model index does not measure rods and plates in trabecular bone. *Frontiers in Endocrinology*, 6, 2015.
- [116] R. Salvador, A. Peña, D. K. Menon, T. A. Carpenter, J. D. Pickard, and E. T. Bullmore. Formal characterization and extension of the linearized diffusion tensor model. *Human Brain Mapping*, 24(2):144–155, 2005.
- [117] E. Schileo, E. DallAra, F. Taddei, A. Malandrino, T. Schotkamp, M. Baleani, and M. Viceconti. An accurate estimation of bone density improves the accuracy of subject-specific finite element models. *Journal of Biomechanics*, 41(11):2483–2491, 2008.

- [118] M. Schwenkglenks, K. Lippuner, H. Huselmann, and T. Szucs. A model of osteoporosis impact in Switzerland 2000–2020. *Osteoporosis International*, 16(6):659–671, 2005.
- [119] C. E. Sexton, U. G. Kalu, N. Filippini, C. E. Mackay, and K. P. Ebmeier. A meta-analysis of diffusion tensor imaging in mild cognitive impairment and Alzheimer’s disease. *Neurobiology of Aging*, 32(12):2322.e5 – 2322.e18, 2011.
- [120] B. C. Silva, W. D. Leslie, H. Resch, O. Lamy, O. Lesnyak, N. Binkley, E. V. McCloskey, J. A. Kanis, and J. P. Bilezikian. Trabecular bone score: a non-invasive analytical method based upon the DXA image. *Journal of Bone and Mineral Research*, 29(3):518–530, 2014.
- [121] A. F. Silveti and C. A. Delrieux. Quadratic self-correlation: an improved method for computing local fractal dimension in remote sensing imagery. *Computers & Geosciences*, 60:142–155, 2013.
- [122] C. A. Simmons and J. A. Hipp. Method-based differences in the automated analysis of the three-dimensional morphology of trabecular bone. *Journal of Bone and Mineral Research*, 12(6):942–947, 1997.
- [123] Skyscan. Structural parameters measured by Skyscan CT-analyzer software. Published electronically at <http://bruker-microct.com/next/CTAn03.pdf>, December 2016.
- [124] S. M. Smith and T. E. Nichols. Threshold-free cluster enhancement: addressing problems of smoothing, threshold dependence and localisation in cluster inference. *Neuroimage*, 44(1):83–98, 2009.
- [125] S. M. Smith, M. Jenkinson, H. Johansen-Berg, D. Rueckert, T. E. Nichols, C. E. Mackay, K. E. Watkins, O. Ciccarelli, M. Z. Cader, P. M. Matthews, and T. E. J. Behrens. Tract-based spatial statistics: Voxelwise analysis of multi-subject diffusion data. *Neuroimage*, 31(4):1487–1505, 2006.
- [126] G. Stebbins and C. Murphy. Diffusion tensor imaging in Alzheimer’s disease and mild cognitive impairment. *Behavioural Neurology*, 21(1-2):39–49, 2009.
- [127] S. Svensson. Centres of maximal balls extracted from a fuzzy distance transform. In *Proceedings of the 8th International Symposium on Mathematical Morphology*, volume 2, pages 19–20, 2007.
- [128] F. Thomsen. Medical image processing with the 2-dimensional analytic signal. Diploma thesis, Christian-Albrechts-Universität zu Kiel, 2010.

- [129] F. Thomsen and C. Delrieux. Soft classification of the plate-rod model using three dimensional rose diagrams. In *Escuela y Workshop Argentino en Ciencias de las Imágenes*, 2014.
- [130] F. Thomsen, J. Peña, J. Bastgen, B. Hoffmann, I. Frieling, C.-C. Glüer, and C. Delrieux. Binary local fractal dimension: a precise structure parameter for 3D high resolution computed tomography images of the human spongiosa. In *Proceedings of the 14th Argentine Symposium of Technology*, pages 232–243, 2013.
- [131] F. Thomsen, J. Peña, C. Delrieux, and C.-C. Glüer. Structural Insight v3: a stand-alone program for micro structural analysis of computed tomography volumes. In *Anales del Congreso Argentino de Informática y Salud*, 2016.
- [132] F. Thomsen, J. Peña, Y. Lu, G. Huber, M. Morlock, C.-C. Glüer, and C. Delrieux. A new algorithm for estimating the rod volume fraction and the trabecular thickness from in vivo computed tomography. *Medical Physics*, 43(12):6598–6607, 2016.
- [133] F. Thomsen, C. Delrieux, and R. de Luis-García. Local texture descriptors for the assessment of differences in diffusion magnetic resonance imaging of the brain. *International Journal of Computer Assisted Radiology and Surgery*, 12(3):389–398, 2017.
- [134] W. Timm. *Markovianity of Trabecular Networks*. PhD thesis, Christian-Albrechts-Universität zu Kiel, 2006.
- [135] A. Tristán-Vega and S. Aja-Fernández. Design and construction of a realistic DWI phantom for filtering performance assessment. In *Medical Image Computing and Computer-Assisted Intervention*, pages 951–958. Springer, 2009.
- [136] A. Tristán-Vega and S. Aja-Fernández. DWI filtering using joint information for DTI and HARDI. *Medical Image Analysis*, 14(2):205–218, 2010.
- [137] D. S. Tuch. Q-ball imaging. *Magnetic Resonance in Medicine*, 52(6):1358–1372, 2004.
- [138] B. Vasilic, C. S. Rajapakse, and F. W. Wehrli. Classification of trabeculae into three-dimensional rodlike and platelike structures via local inertial anisotropy. *Medical Physics*, 36:3280, 2009.
- [139] J.-J. Wang, T.-C. Chao, Y.-Y. Wai, and Y. Hsu. Novel diffusion anisotropy indices: an evaluation. *Journal of Magnetic Resonance Imaging*, 24(1):211–217, 2006.

- [140] J. Wegrzyn, J.-P. Roux, M. E. Arlot, S. Boutroy, N. Vilayphiou, O. Guyen, P. D. Delmas, R. Chapurlat, and M. L. Bouxsein. Role of trabecular microarchitecture and its heterogeneity parameters in the mechanical behavior of ex vivo human L3 vertebrae. *Journal of Bone and Mineral Research*, 25(11): 2324–2331, 2010.
- [141] C.-F. Westin, S. E. Maier, H. Mamata, A. Nabavi, F. A. Jolesz, and R. Kikinis. Processing and visualization for diffusion tensor MRI. *Medical Image Analysis*, 6(2):93–108, 2002.
- [142] J. S. Weszka. A survey of threshold selection techniques. *Computer Graphics and Image Processing*, 7:259 – 265, 1978.
- [143] A. Wimo, L. Jönsson, J. Bond, M. Prince, B. Winblad, and Alzheimer Disease International. The worldwide economic impact of dementia 2010. *Alzheimer’s & Dementia*, 9(1):1–11, 2013.
- [144] T. Wise, J. Radua, G. Nortje, A. J. Cleare, A. H. Young, and D. Arnone. Voxel-based meta-analytical evidence of structural disconnectivity in major depression and bipolar disorder. *Biological Psychiatry*, 79(4):293–302, 2016.
- [145] I. Wolff, J. Van Croonenborg, H. Kemper, P. Kostense, and J. Twisk. The effect of exercise training programs on bone mass: a meta-analysis of published controlled trials in pre- and postmenopausal women. *Osteoporosis International*, 9(1):1–12, 1999.
- [146] Y. Zhou and A. Toga. Efficient skeletonization of volumetric objects. *Transactions on Visualization and Computer Graphics, IEEE*, 5(3):196–209, 1999.
- [147] K. H. Zou, A. Liu, A. I. Bandos, L. Ohno-Machado, and H. E. Rockette. *Statistical evaluation of diagnostic performance: topics in ROC analysis*. CRC Press, 2011.